ROLE OF ELECTRON-HOLE RECOLLISIONS IN HIGH HARMONIC GENERATION FROM BULK CRYSTALS

By
Giulio Vampa

A thesis submitted to the
Faculty of Graduate and Postdoctoral Studies
in partial fulfilment of the requirements for the
degree of Doctor of Philosophy in Physics

Department of Physics
Faculty of Science
University of Ottawa

Contents

List of Tables

List of Figures

List of Symbols

κ	Reciprocal lattice vector
λ	Fundamental laser wavelength
ω	High harmonic frequency
ω_0	Fundamental laser frequency
ω_c	High harmonic cut-off frequency
ε_g	Momentum-dependent band gap
a	Lattice constant
a_l	Effective lattice constant, such that $\kappa a_l = 2\pi$
E_c, E_v	Conduction and Valence band energies
E_g	Minimum energy gap of solids
F_0	Fundamental laser peak electric field strength inside the solid (or in vacuum if referred to gas)
F_{vac}	Fundamental laser peak electric field strength in vacuum
I_p	Atomic ionization potential
n_m	Population in band m
S	Semiclassical action
T_0	Fundamental laser period
T_2	Dephasing time for the interband polarization
t_r	Recollision time
U_p	Ponderomotive energy
$\mathbf{A}, A$	Laser vector potential (bold for vectorial)
$\mathbf{F}, F$	Electric field strength (bold for vectorial)

$\mathbf{j}_{\mathrm{er}}, \mathrm{j}_{\mathrm{er}}$ Interband current (bold for vectorial)

$\mathbf{j}_{\mathrm{ra}}, \mathrm{j}_{\mathrm{ra}}$ Intraband current (bold for vectorial)

$\mathrm{v_c}, \mathrm{v_c}$ Velocities of electron and holes in the conduction and valence bands respectively

$\mathbf{d_{mm'}}, \mathrm{d_{mm'}}$ Transition dipole moment between bands m and m'

$\mathbf{k}, \mathrm{k}$ Crystal momentum of electrons and holes in solids (bold for vectorial)

BZ Brillouin zone

Abstract

When intense laser pulses interact with an atomic or solid target, high order harmonics of the fundamental laser frequency are generated. In the case of atoms, this highly nonlinear optical process is initiated by ionization and terminated by the energetic recollision and recombination of the ionized electron with its correlated ion. In this thesis I demonstrate, both theoretically and experimentally, that high harmonics from bulk crystals can originate from the recollision of electrons with their associated holes, similarly to the atomic case, but where ionization is replaced by excitation of electron-hole pairs that accelerate within the material. This model is first derived from a quantum-mechanical theory of the solid-laser interaction, and then confirmed experimentally in ZnO and Si crystals. Despite the link I establish between high harmonic generation in solids and gases, there are notable dissimilarities. These include: a generalized motion of electrons and holes in their respective bands and its consequences, a more prominent role of dephasing and enhanced sensitivity to perturbing fields. These aspects are investigated throughout this thesis. Finally, I develop a method that exploits the recollision mechanism to reconstruct the momentum-dependent band structure of solids.

Résumé

Lorsque d'intenses impulsions lasers interagissent avec une cible atomique ou solide, des harmoniques d'ordre supérieur de la fréquence laser fondamentale sont générées. Dans le cas des atomes, ce processus optique nonlinéaire extrême est initié par l'ionisation et est terminé par la recollision énergétique et la recombination de l'électron ionisé avec son ion corrélé. Dans cette thèse, je démontre, de façon théorique et expérimentale, que les hautes harmoniques qui proviennent de l'intérieur d'un crystal peuvent avoir comme origine la recollision des électrons avec leur "hole" associé, ce qui est similaire au processus dans les atomes, mais où l'inonisation est remplacée par l'excitation des paires d'électron et "hole" qui accélèrent dans le matériel. Ce modèle est tout d'abord dérivé d'une théorie de la mécanique quantique de l'interaction d'un solide avec un laser, et est ensuite confirmé de façon expérimentale dans les cristaux de ZnO et de Si. En dépit du lien que j'établis entre la génération des hautes harmoniques dans les solides et dans les gaz, des dissemblances sont remarquables. Elles incluent: un mouvement généralisé des électrons et des "holes" dans leurs bandes respectives et les conséquences, un rôle plus proéminent de déphasage et une augmentation de sensibilité aux champs perturbants. Ces aspects sont analysés dans cette thèse. Finalement, je développe une méthode qui exploite le mécanisme de recollision pour reconstruire la structure à bandes des solides qui dépendent du momentum.

Acknowledgements

I wish to thank my supervisor, Prof. Paul Corkum, for the superb guidance and the endless faith and optimism.

Over time I convinced a formidable team of scientists to work on solids. I'm thankful to each one of them. First and foremost, to Prof. Thomas Brabec. Although the first theoretical evidence of interband recollisions was one of my achievements, the rigour and completeness of his analysis put those findings on solid grounds. His "touch" is present in all theoretical parts of this thesis. The methods I learnt working with him will be invaluable tools for my career.

I also learnt part of the vast experimental skills and pragmatic attitude of Dr. Thomas J Hammond. Besides the publications that resulted from collaborating with him, the transferred know-how – much more difficult to quantify – will equally impact my career. Many ideas presented in this thesis were spurred by discussing with TJ.

Further theoretical support was provided by Dr. Chris McDonald, who performed all 3D simulations of the high harmonic emission, and Dr. Dennis Klug, who performed all *ab initio* calculations of the band structures and with whom I had insightful discussions on solid state and group theory.

Furthermore, I wish to thank Dr. Nicolas Thiré for collaborating to the experiment and for bringing to my attention some important literature, and to Prof. François Légaré to allow us access to the lasers of the Advanced Laser Light Source.

Finally, I would like to thank my partner Laurence and my newborn son Fabio, for keeping quiet during the drafting of this thesis.

I acknowledge funding from the NSERC CREATE program through Prof. Corkum.

Introduction

Fifty years ago Keldysh [1] introduced an important idea. Treating both isolated atoms and solids on the same footing, he demonstrated that ionization in a strong laser field – valence-band to conduction-band transitions in solids – can be approximated by tunnelling.

Over the following decades, research over the interaction of intense laser pulses with solids and gases has diverged. Much of the solid-state research has been motivated by laser material processing, which uses dielectric breakdown initiated by tunnelling to induce permanent changes to materials. A great deal of the gas-phase research has been motivated by high harmonic generation, a process initiated by tunnelling and completed by the recollision of a highly energetic electron with its associated ion (or "hole") (for a review of the field see Ref. [2]). At the moment of recollision, the electron can recombine with the hole thereby converting the kinetic energy gained in the laser field to a high energy photon. Photon energies as high as 1 keV can be achieved [3]. The spectacular coherence properties of high harmonic generation have been used to image molecular wavefunctions [4, 5], to map the evolution of chemical reactions [6], to study multi-electron dynamics in molecules [7, 8] and to synthesize light flashes that last only some tens of attoseconds ($1\text{as} = 10^{-18}\text{s}$) [9]. These pulses are used to perform pump-probe studies with attosecond resolution in gases [10, 11], solids [12, 13, 14] and biomolecules [15].

However, the deep similarity of gases and solids to strong laser fields has been largely ignored. In recent years, high harmonics have been generated from the bulk of a solid [16]. This breakthrough experiment triggered further research, with high harmonics now being generated in different materials [17, 18]. In light of these experiments, it is important to reconsider the relation between gas-phase and solid-state high harmonic generation mechanisms.

In this thesis I demonstrate, theoretically and experimentally, that high harmonics from solids can be generated by a recollision mechanism analogous to the atomic (gaseous) one, in which electrons and holes are accelerated in the conduction and valence bands respectively. Therefore a link is established between harmonics generated in gases and in bulk solids. I exploit this link to demonstrate an all-optical method to reconstruct the band structure of the solid.

The thesis is organized as follows.

- In chapter 1, I introduce the semiclassical model of atomic recollisions to

explain gas-phase high harmonics, and use it to extend it to solids.

- In chapter 2, the semiclassical model is justified with a quantum-mechanical theory. Several other mechanisms of high harmonic emission are also analysed. The features exclusive to harmonics from solids are also discussed.

- In chapter 3, the role of recollisions is demonstrated experimentally in ZnO (a wide direct band gap semiconductor) and Si (a narrow indirect band gap semiconductor). The experiment in Si also provides insights into the tunnelling step. The sensitivity of the generation process to weak fields is discussed in terms of the solid's band structure, and compared to the atomic case. Finally, the possibility of creating attosecond high harmonic pulses from solids is investigated.

- In chapter 4, I present two consequences of recollisions. First, they can be used to reconstruct a material's band structure. Second, they allow an analytical scaling law of the cut-off harmonic to be developed. Lastly, a mechanism to reach higher harmonics is presented.

Chapter 1

Semiclassical model

To understand the basics of high harmonic generation in bulk solids it is most useful to describe a semiclassical model of the motion of electron-hole pairs that are created by the laser field. The model is derived from a quantum theory, introduced in chapter 2, where it's validated with simulations. In this chapter the model is introduced by a heuristic extension of the more familiar classical model of high harmonic generation from atoms. This chapter answers the question: "How would a classical model of high harmonics from solids work, had the generating mechanism been equivalent to the atomic case?"

The contents presented in this chapter are based on three publications of mine [19, 20, 21]. The contents of section 1.2 are entirely based on the results of my research.

1.1 The atomic case

The basic features of the high harmonic generation process in gases can be grasped with a semiclassical three-step model:

1. An electron, initially bound to an atomic core, tunnels through the potential barrier lowered by the strong laser field and is freed with zero initial kinetic energy, leaving a hole strongly localized on the atom.

2. The electron is accelerated away by the strong laser field and, if the time at which the electron is ionized relative to the peak of the laser electric field is right, it can return towards the ionic core.

3. The electron meets the hole and can recombine with it, emitting the kinetic energy that it picked up in the laser field plus the ionization potential of the atom as a high harmonic photon.

The ionization step. For the purpose of high harmonic generation, the major role played by the first step is to free the electron from the atom. Although the electron crossing the barrier has some influence over the high harmonics, in this

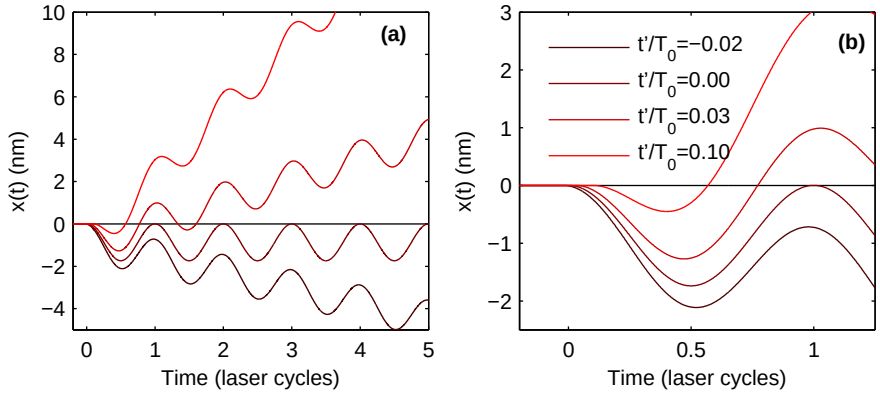

Figure 1.1: Trajectories of electrons ionized at different times relative to the peak of the electric field, set at an intensity of 10^{14} W/cm^2 with central wavelength of 800 nm. **(b)** is a close up within one laser cycle. T_0 is the laser cycle.

context the nature of the ionization step is disregarded. The quantum nature of ionization leaves uncertainty in the time at which the electron crosses the barrier and begins to accelerate away from the hole.

The propagation step. The analysis starts with a free electron subject to the laser electric field $\mathbf{F}(t) = F_0 \cos(\omega_0 t)\hat{\mathbf{x}}$. In atomic units ($e = m = \hbar = 4\pi\epsilon_0 = 1$), the momentum of the electron is:

$$\mathbf{k} \equiv \dot{\mathbf{x}}(t) = -\hat{\mathbf{x}} \int_{t'}^{t} F_0 \cos(\omega_0 \tau)\, d\tau + \mathbf{v_0} = -\frac{F_0}{\omega_0} \left[\sin(\omega_0 t) - \sin(\omega_0 t')\right] \hat{\mathbf{x}} + \mathbf{v_0} \quad (1.1)$$

In the following, the vector notation is dropped because the motion is confined along the (linear) laser polarization. The quantum model suggests that the electron tunnels with approximately zero initial velocity: $\mathbf{v_0} \simeq 0$. The time the electron begins to move, t', is measured relative to the peak of the laser field at $t' = 0$. The position of the electron is:

$$\mathrm{x}(t) = \int_{t'}^{t} \dot{\mathrm{x}}(\tau)\, d\tau = \frac{F_0}{\omega_0^2} \left[\cos(\omega_0 t) - \cos(\omega_0 t') + \sin(\omega_0 t')(t - t')\right] \quad (1.2)$$

When $t' \neq 0$ the electron oscillates with non-zero average momentum $\mathrm{k_{drift}} \propto \sin(\omega_0 t')$, which drifts its mean position relative to the hole (fixed at x = 0) linearly in time. The later the time of ionization, the stronger the electron drifts (see Fig. 1.1**a**). An electron born at the peak of the field re-encounters the hole after each laser cycle, while one born after the peak re-encounters it a limited number of times, and earlier in the cycle (see Fig. 1.1**b**). Another consequence of the classical motion is that, if the Coulomb attraction of the ion is neglected, an electron born before the peak of the field never re-encounters the hole, because the drift velocity changes sign and acts together with the electric field right after ionization to accelerate the electron farther.

The most common experiments focus femtosecond laser pulses with a bandwidth centred about 800 nm to intensities about 10^{14} W/cm^2. In these conditions the

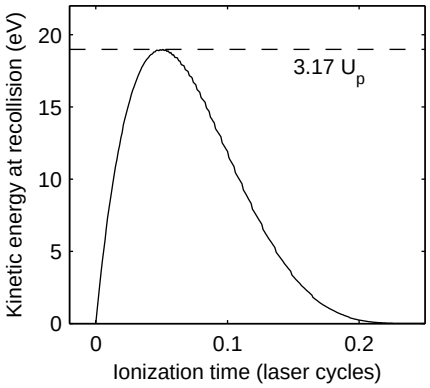

Figure 1.2: Kinetic energy of the electron at the time of recollision, as a function of the time of ionization. The maximum kinetic energy is determined by 3.17 U_p. The laser intensity is 10^{14} W/cm^2, central wavelength is 800 nm.

maximum excursion of the electron before recollision ($2F_0/\omega_0^2$, from Eq. 1.2) is on the order of 1 nm, therefore much larger than the atomic radius ($\sim$ 0.1 nm). The cycle-averaged kinetic energy of electrons born at the peak of the field, the *ponderomotive energy* U_p, is typically used as a good metric of the energetics of the process. From Eq. (1.1) it is easily derived that $U_p = F_0^2/(2\omega_0)^2 \simeq 10$ eV. Ponderomotive energies as high as 1000 eV can be reached in experiments with laser fields of longer wavelength and intensities in the 10^{15} W/cm^2 range [3].

Recollision and emission of high harmonics. Figure 1.1(b) shows the link between the times of creation and of recollision of the electron-hole pair: the later the electron is ionized, the sooner it recollides with the hole (fixed at $x = 0$). The kinetic energy T of the electron is transferred to a high harmonic photon upon recombination of the electron with its associated hole. Its energy is:

$$\hbar\omega = T + I_p \tag{1.3}$$

where I_p is the ionization potential of the atom. The electron's velocity at the time of recollision, the slope of the lines at the zero crossings, also depends on the time of ionization. This is shown in Fig. 1.2. It is found numerically that the harmonic photon energy peaks for an ionization phase of $\simeq 0.31$ rad at the energy given by [22, 23]:

$$\hbar\omega_c = 3.17\, U_p + I_p. \tag{1.4}$$

The existence of electron trajectories completely determined by any variable among time of ionization, time of recollision and emitted photon energy, is the most experimentally exploited characteristic of atomic high harmonic generation.

The bandwidth of the emitted radiation, shown in Fig. 1.2, is continuous. It does not explain the generation of only the odd-order harmonics, observed in experiments[1] [23]. Odd harmonics result from the interference between emissions at each

[1] A continuous bandwidth is experimentally observed under special circumstances.

laser half-cycle[2]. Harmonic radiation emitted at successive half-cycles has opposite phase, due to the change of sign of the driving laser field. The phase flip results in constructive interference of harmonic frequencies that are exactly odd multiples of the driving laser frequency. This is demonstrated below by summing only two harmonic waves of frequency $n\omega_0$ emitted with a delay of half of the fundamental laser cycle:

$$e^{in\omega_0 t} - e^{in(\omega_0 t+\pi)} = e^{in\omega_0 t}(1 - e^{in\pi}) = \begin{cases} 2e^{in\omega_0 t} & \text{if } n \text{ is odd,} \\ 0 & \text{if } n \text{ is even.} \end{cases}$$

This is, in a nutshell, atomic high harmonic generation. The classical concepts introduced in this section are sufficient to extend the recollision model to solids, a task that is performed in the next section.

1.2 From atoms to solids

To introduce a model of recollision in solids, it is convenient to translate the atomic model, presented as electrons moving in the real space, in the momentum/energy space. This is the natural framework in which solids are described. How to understand the interaction of the atom with the strong laser field in this framework?

Atomic high harmonic generation in momentum space. The energy diagram of atoms in strong laser fields is shown to the left of Fig. 1.3. In the following, only one electron-hole pair is considered, which emits high harmonics at the energy determined by its time of creation. The electron is initially in the ground state of the atom with energy $-I_p$. Upon tunnelling (blue arrow labelled "1"), the electron is freed in the vacuum with approximately zero initial velocity. Because the energy of a free electron is $T = \mathrm{k}^2/2$, it occupies the lowest-energy state in this continuum function of momentum (a parabolic band, black solid line in the middle of Fig. 1.3). As the electron accelerates, it gains the momentum described by Eq. (1.1), which can be rewritten in terms of the vector potential of the laser field $A(t)$ ($F(t) = -\partial A/\partial t$):

$$\mathrm{k}(t) = A(t) - A(t'). \tag{1.5}$$

In doing so, the electron gains the energy $\mathrm{k}^2(t)/2$: it climbs up the parabolic band (blue arrow labelled "2"). The hole, created in the ground state upon ionization, also gains the same momentum as the electron[3], but its energy is constant. At the

[2]Interference arises in the act of measuring the spectrum. Sufficient spectral resolution comes to the price of lengthening the harmonic pulses by more than their temporal separation, which allows them to interfere.

[3]Electrons and holes move together in momentum space. To describe the hole, in fact, the prescription of solid state physics says that both the charge and the mass of the electron must change sign. Since $\mathrm{k} \propto e/mA(t)$, the momentum is the same for electrons and holes.

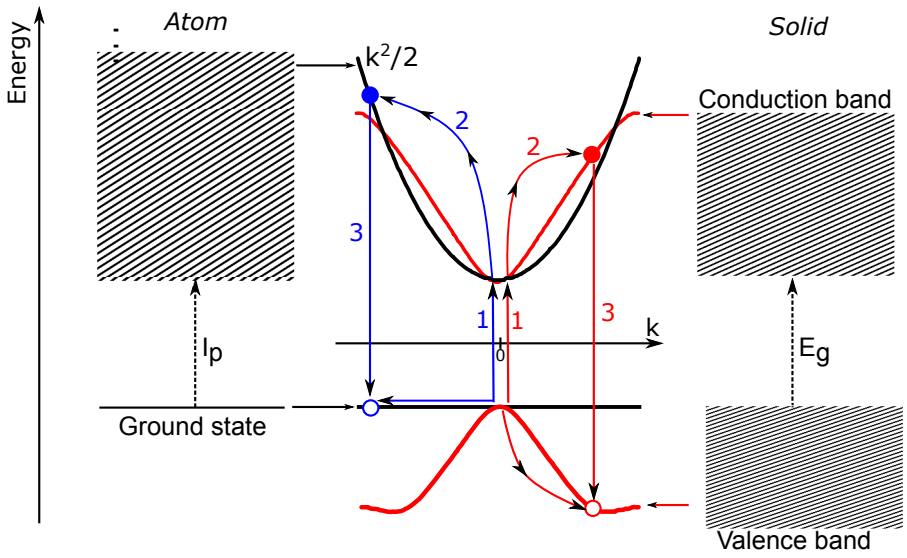

Figure 1.3: Energy diagrams of atoms and solids. In an atom (left), the ground state is a localized energy state, separated by the ionization potential I_p from the continuum states (band) of vacuum (the dashed square). In momentum space, the latter is a parabola (black line in the middle). In a solid (right), both ground and excited states form bands (valence and conduction, respectively), separated by the minimum energy gap E_g. They are more complicated functions of momentum (red lines in the middle). Here, the valence and first conduction band of a ZnO crystal are shown. They are calculated with Density Functional Theory (implemented by the ABINIT code [24]). High harmonic generation proceeds through creation of an electron-hole pair (labelled "1", blue colors for the atomic case, red for the solid), acceleration of the pair to high momentum (labelled "2"), and recombination of the electron with the hole (labelled "3"). Although in the atomic case the pair is created with zero initial momentum (k = 0), in a solid this is not always the case.

time of recollision t_r, the electron recombines with the hole (undergoing a vertical transition back to the ground state, marked by the blue arrow labelled "3") at the momentum $\mathrm{k}(t_r) = A(t_r) - A(t')$ and a photon of energy equal to $\mathrm{k}^2(t_r)/2 + I_p$ is emitted.

The model for solids. In crystalline solids, contrary to atoms, the electron is initially in a continuum of states, the *valence band*. The valence band is separated from higher energetic states by an energy gap, or *minimum band gap* (equivalent to the atom's ionization potential). In the following, only dielectric or semiconducting materials will be considered, so that the minimum band gap is non zero. The excited states, the *conduction bands*, also form several continua. The formation of bands reflects the quanto-mechanical electron's de-localization over the lattice of the crystal. The motion of electrons is therefore different than in free space, and results in the energy bands being non-parabolic functions of momentum. To the right of Fig. 1.3, one valence and one conduction band of a ZnO crystal are plotted.

The recollision model of high harmonic generation from solids is the following.

1. Around the peak of the laser field, an electron tunnels vertically from the valence to the conduction band (red arrow labelled "1" in Fig. 1.3) at the momentum of highest tunnelling probability. This is illustratively at $k = 0$ in Fig. 1.3 to make contact with the atomic case, but it can be at $k \neq 0$. An electron-hole pair is thus formed. The rate of tunnelling is obviously different than in atoms, and is currently a matter of intense debate in the scientific community [13, 12].

2. Regardless on how the electron tunnels, the laser field subsequently accelerates the pair. Like in atoms, its momentum is determined by Eq. (1.5). The energy also increases (red arrow labelled "2"), according to the structure of the band. The evolution of the momentum is plotted in Fig. 1.4(a) for some electron-hole pairs created at different times after the peak of the laser field. The same plot would be obtained for the case of an isolated atom. Like in atoms, the electron and the hole accelerate in opposite directions in real space (see Fig. 1.4**b**).

3. Some time later in the laser cycle, the electron can re-encounter the hole with non-zero momentum, they can recombine (red arrow labelled "3" in Fig. 1.3) and emit a harmonic photon of energy $\hbar\omega = \varepsilon_g[\mathrm{k}(t_r)]$, with $\varepsilon_g(k)$ being the difference in energy between the conduction and valence states at the momentum k. The time of re-encounter and the associated momentum of each electron-hole pair is marked by open circles in Fig. 1.4(a).

The time of re-encounter is dictated by the motion of electrons and holes in real space, which is markedly different between atoms and solids. This is because, in the solid state language, the velocity of electrons in band m is determined by (in atomic units):

$$\mathrm{v_m(k)} = \nabla_{\mathrm{k}} E_{\mathrm{m}}(\mathrm{k}) \tag{1.6}$$

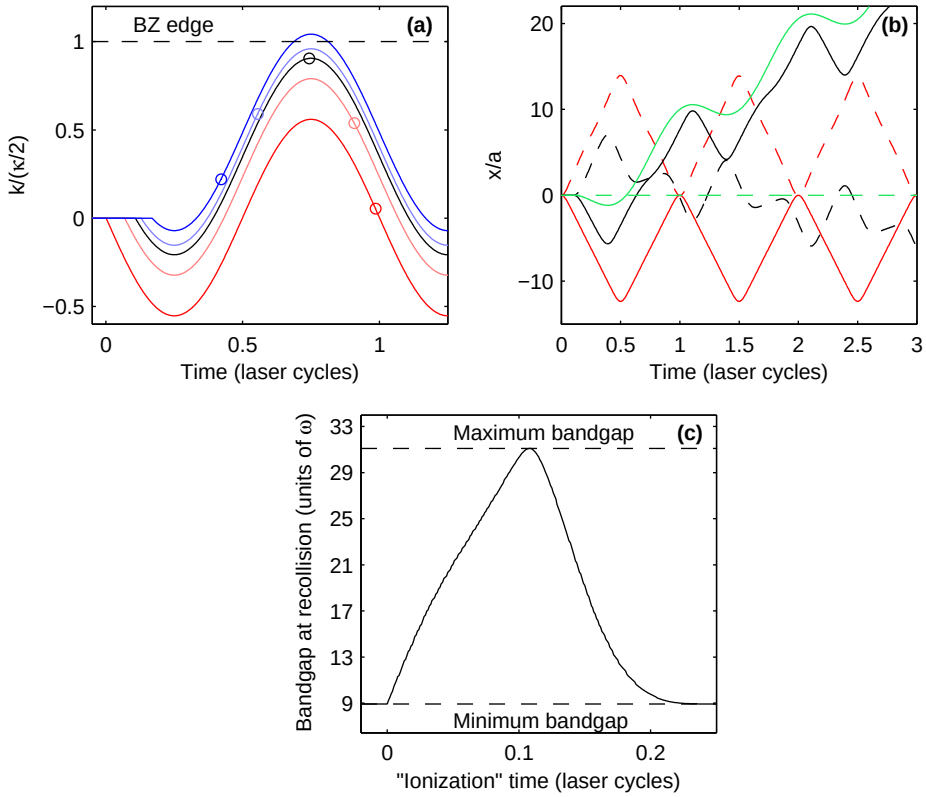

Figure 1.4: Semiclassical propagation in solids. **(a)** Time-dependent momentum $k(t)$ (calculated with Eq. (1.5) for a set of trajectories born at different times after the peak of the field. The dark red line is for $t' = 0$, while the black line marks the trajectory that emits the highest harmonic photon energy (cutoff). The time of recollision between electrons and hole is marked for each trajectory by the open circles. Momentum is given in units of half the reciprocal lattice vector $\kappa/2 = \pi/a_l$, with a_l the separation between the lattice planes identified by the particular relative orientation of the laser polarization with respect to the crystallographic axis. Here, $a_l = 5.32$ a.u. for ZnO. The dashed line marks the edge of the first Brillouin Zone at $k = \kappa/2$. In a periodic solid, owing to the discrete translational symmetry, higher momenta can be mapped back to the first BZ. The simulation is performed with laser frequency $\omega_0 = 0.014$ a.u. ($\lambda = 3.25\ \mu m$) , and $F_0 = 0.0046$ a.u. ($0.24\ V/\text{Å}$, corresponding to an intensity of $8 \times 10^{11}\ W/cm^2$). **(b)** Position of electrons (solid lines) and holes (dashed lines) following their creation, for pairs born at the peak of the field (red lines) and for the cutoff trajectory (black lines). The green lines are the cutoff atomic trajectories, for an 800 nm laser at $10^{14}\ W/cm^2$ (as in Fig. 1.2). **(c)** Energy of electron-hole pairs at the time of recollision, as a function of the time of their creation. This energy is transferred to high harmonic photons, upon recombination of the electrons with the holes. Classically allowed emission is limited within the minimum and maximum bandgap of the material (dashed lines), typically occurring at the center and edge of the BZ respectively.

where $E_{\mathrm{m}}(\mathrm{k})$ is the momentum-dependent energy of the band in which the electron (or hole) travels. For an electron in vacuum, for which $E(\mathrm{k}) = \mathrm{k}^2/2$, one obtains the classical definition of momentum: $\mathrm{v} = \mathrm{k}$. Therefore, no meaningful distinction is made between velocity and momentum. However, because bands in solids are more complex functions of momentum, this simple relation doesn't hold. Therefore, "k" is called *crystal momentum* to distinguish it from the real space momentum. To describe the motion of electrons and holes in real space, one has to solve Eq. (1.1) (or Eq. 1.5) together with:

$$x_e(t) = \int_{t'}^{t} \nabla E_c[\mathrm{k}(\tau)]\, d\tau \;\; ; \;\; x_h(t) = \int_{t'}^{t} \nabla E_v[\mathrm{k}(\tau)]\, d\tau \tag{1.7}$$

where E_c and E_v are the conduction and valence bands respectively. Figure 1.4(b) shows the real space trajectories of electrons (solid lines) and holes (dashed lines) for two different times of creation of the pairs (red for pairs created at the peak of the field, and black after the peak, corresponding to emission at the cut-off energy). They are compared to the atomic trajectory responsible for high harmonic emission at the cut-off (green lines). The motion in the solid is clearly different than in vacuum. The time of re-encounter, determined by the crossing of the dashed with the solid lines, is therefore also markedly different between the two cases, even though both trajectories are associated to cut-off emission. Similar deviations are found for all other trajectories (except for $t' = 0$).

As a result of the "generalized" time of recollision, and of the band structure, the energy of recolliding pairs maps differently than in atoms to their time of creation. This is shown in Fig. 1.4(c). Contrary to atoms, where the kinetic energy of the electron is potentially unlimited, in a solid composed of only two bands, the maximum harmonic emission is capped to the maximum bandgap energy (marked by the black dashed line).

Consequences of the model. In summary, the recollision model for solids generalizes atomic high harmonic generation to arbitrary band structures (not only parabolic). In atoms, the electrons' trajectories are universally defined, once all quantities are scaled with the laser peak field strength and frequency. In solids, the universality is lost: the trajectories also depend on the band structure, and to which portion the electron-hole pairs explore during their motion. The generalized relation between the times of creation, of recollision, and the harmonic photon energy, is the most apparent consequence of the model. It will be investigated further in a next chapter. Other paradigms of atomic high harmonic generation are lost as well. Below, I briefly discuss some of them.

- *The hole also moves.* This is a consequence of the dispersion of the band in momentum space. In atoms, the ground state is an almost flat band. Therefore, according to Eq. (1.6) the hole's velocity is almost zero.

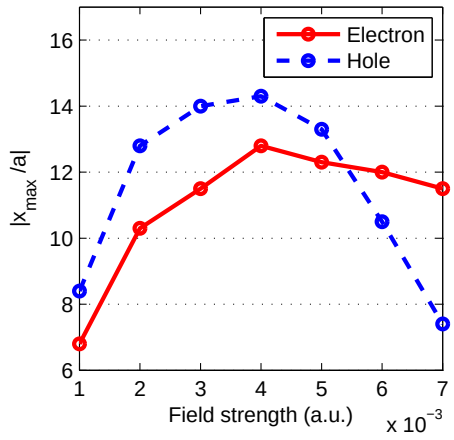

Figure 1.5: Maximum excursion of electrons (red line) and holes (blue line) in units of lattice cells, as a function of field strength.

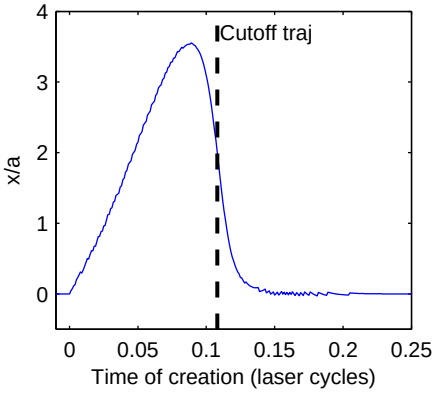

Figure 1.6: Position of recollision between electrons and holes of each trajectory born between the peak and the first zero of the field. The dashed vertical line marks the cut-off trajectory.

- *The hole's and electron's maximum excursion is limited.* Because typical bands change curvature at sufficiently high momenta, the velocity reaches a maximum at the inflection point. Therefore, an increase in momentum slows down the particle propagating in the band, and limits its maximum excursion in the laser field. Figure 1.5 shows the maximum excursion (in units of lattice cells) for electrons and holes born at the peak of the field as a function of the peak field strength (in atomic units).

- *Recollision can happen away from the origin.* Figure 1.6 shows the position of electron-hole pairs at recollision (in units of lattice cells) with respect to their place of origin (at $x = 0$) for all trajectories born around the peak of the laser field. Pairs can recollide some lattice cells away!

- *Trajectories born before the peak of the laser electric field can recollide.* When the field strength is increased, the trajectories significantly distort: some pairs that would typically recollide, won't, and pairs born before the peak of the field, which would typically avoid recollision, recollide. An in-depth analysis of the distortions is deferred to section 2.2.

In the next chapter, the semiclassical model of high harmonic generation in solids is derived from a quantum-mechanical theory.

Chapter 2

Quantum model

In this chapter I introduce the quanto-mechanical theory underlying high harmonic generation, and the interaction of strong laser fields with solids in general. The model is, again, a generalization of the one used to describe atomic high harmonic generation. Just like in the atomic case, high harmonics are emitted by the oscillating dipole. There are two major results: (i) the semiclassical recollision model already introduced can be derived from one part of the oscillating dipole, and (ii) there are other parts that also emit high harmonics. The relative importance and the temporal properties of harmonics emitted by each mechanism are analysed in the last part of the chapter.

The material presented is based on two publications of mine [19, 20]. Although the density matrix formulation (Eqs. 2.6 and 2.8) was already known to the community, their derivation from the Schrödinger equation and the link between the two formalisms is one of my achievements. Before my work, the density matrix equations were solved numerically, and only for laser wavelengths resonant with the minimum bandgap, a regime unsuited for high harmonic generation. Moreover, the analytical solution to the density matrix equations was missing. I find analytical solutions in the Keldysh limit (Eqs. 2.12a and 2.12b) and, from them, derive the semiclassical model of recolliding electron-hole pairs. I validate the model by comparing the temporal properties of high harmonics with those obtained from numerical integration for laser wavelengths much smaller than the minimum band gap, the regime used in the first experimental report on high harmonic generation from solids. The contents of sections 2.2, 2.3 and 2.4 result solely from my research.

2.1 Derivation of the dipole moment

The time dependent Hamiltonian is given by $H(t) = H_0 - \mathbf{x} \cdot \mathbf{F}(t)$, where $H_0 = T + U$ is the unperturbed Hamiltonian with $T = -\mathbf{p}^2/2$ the kinetic energy operator, $\hat{\mathbf{p}} = -i\nabla$ the momentum operator, and $U(\mathbf{x})$ the periodic potential of the lattice[1].

[1]Either the length (as done here) or the velocity gauge can be used without any effect on expectation values. They are independent on the gauge because the only difference is a phase

The field free Hamiltonian H_0 has Bloch eigenstates $\Phi_{\mathrm{m},\mathbf{k}}(\mathbf{x}) = u_{m,\mathbf{k}}(\mathbf{x})\exp(i\mathbf{k}\cdot\mathbf{x})$ with energies $E_{\mathrm{m},\mathbf{k}} = E_{\mathrm{m}}(\mathbf{k})$ in band m with crystal momentum $\mathbf{k}$; $u_{\mathrm{m},\mathbf{k}}$ is the periodic part of the Bloch function. The analysis is restricted to a two-band model with valence (m = v) and conduction (m = c) bands.

In the presence of the laser field the wavefunction becomes time dependent. In the length gauge it is represented as

$$\Psi(\mathbf{x},t) = \sum_{\mathrm{m=c,v}} \int_{\mathrm{BZ}} a_{\mathrm{m}}(\mathbf{k},t)\Phi_{\mathrm{m},\mathbf{k}}(\mathbf{x})\, d^3\mathbf{k} \tag{2.1}$$

with probability amplitudes $a_{\mathrm{m}}(\mathbf{k},t)$. The integration is performed over the primitive cell of the momentum space, the Brillouin Zone (BZ).

To obtain the equations of motion for the probability amplitudes $a_{\mathrm{m}}(\mathbf{k},t)$, ansatz (2.1) is substituted into the time-dependent Schrödinger equation for the Hamiltonian $H(t)$:

$$i\frac{\partial\Psi(\mathbf{x},t)}{\partial t} = H(t)\Psi(\mathbf{x},t) \tag{2.2}$$

and the Bloch eigenstates are integrated out, yielding

$$\dot{a}_{\mathrm{m}} = (-iE_{\mathrm{m}}(\mathbf{k}) + \mathbf{F}(t)\nabla_{\mathbf{k}})a_{\mathrm{m}} + i\mathbf{F}(t)\sum_{m'\neq m}\mathbf{d}_{\mathrm{mm'}}(\mathbf{k})a_{\mathrm{m'}} \tag{2.3}$$

with $\mathrm{m} = \{\mathrm{v},\mathrm{c}\}$, $\mathrm{m'} = \{\mathrm{v},\mathrm{c}\}$, and with

$$\mathbf{d}_{\mathrm{mm'}}(\mathbf{k}) = i\int d^3\mathbf{x}u^*{}_{\mathrm{m},\mathbf{k}}(\mathbf{x})\nabla_{\mathbf{k}}u_{\mathrm{m'},\mathbf{k}}(\mathbf{x}) \tag{2.4}$$

the transition dipole moment between valence and conduction bands. In the derivation the relation $\langle\Phi_{\mathrm{m},\mathbf{k}}|\mathbf{x}|\Phi_{\mathrm{m'},\mathbf{k'}}\rangle = -i\partial_{\mathbf{k}}\delta_{\mathrm{mm'}} + \mathbf{d}_{\mathrm{mm'}}(\mathbf{k})$ [26] is used, which splits the transition dipole into an intraband and interband contribution, respectively[2].

According to Eq. (2.3) there are two ways the electron population is transferred to band m and momentum $\mathbf{k}$:

1. from the other band within the states of same momentum. The term proportional to $\mathbf{d}_{\mathrm{mm'}}$ is responsible for this transition. The same term causes transitions in two-level systems.

2. from adjacent momentum states within the same band. The term proportional to $\nabla_{\mathbf{k}}$ causes this transition. It describes the acceleration of electrons by the laser field. This term differentiates a solid from an independent collection of two-level systems, each system represented by the valence and conduction states at any given $\mathbf{k}$, in which population would not be transferred between systems.

factor in the wavefunctions. This has been demonstrated in [25]

[2]The fact that the intraband term in $\langle\Phi_{\mathrm{m},\mathbf{k}}|\mathbf{x}|\Phi_{\mathrm{m'},\mathbf{k'}}\rangle$ return the operator $\nabla_{\mathbf{k}}$ rather than a number is somewhat bothering. The correct understanding of this expression can be found in Ref. [26].

High harmonics are emitted by the oscillating dipole (or rather its time derivative, the current):

$$< \Psi|\mathbf{x}|\Psi >= \sum_{\mathbf{k}\in BZ} \left[-i \sum_{\mathrm{m=c,v}} \nabla_{\mathbf{k}} |a_{\mathrm{m}}(\mathbf{k},t)|^2 + \sum_{\substack{\mathrm{m=c,v} \\ \mathrm{m}\neq\mathrm{m}'}} a^*_{\mathrm{m}'}(\mathbf{k},t) a_{\mathrm{m}}(\mathbf{k},t) \mathbf{d}_{\mathrm{mm}'}(\mathbf{k}) \right] . \quad (2.5)$$

The first term on the RHS deals with electrons in each separate band. It is commonly called *intraband*, although it necessarily takes into account both bands, at least during the tunnelling step. The second term arises from the interference between electrons in the conduction and valence bands. It is referred to as *interband*.

Relation to atomic high harmonic generation. The model introduced is a generalization of atomic high harmonic generation. In fact, a set of differential equations equivalent to Eq. (2.3) can be obtained by replacing $\Phi_{\mathrm{v},\mathbf{k}}$ with the ground state wavefunction Φ_g (and drop the summation over $\mathbf{k}$ for the ground state), and by considering the dispersion of electrons in vacuum $E_{\mathrm{c}} = \mathbf{k}^2/2$ and the ground state energy $E_{\mathrm{v}} = -I_p$. In atoms, the *intraband* dipole contributes only to low order harmonics, whereas higher order harmonics – arising from the recolliding electron-hole pairs – are generated by the *interband* term.

The density matrix formulation. Rather than working with the Schrödinger equation, one could work with the density matrix formalism [27, 28]. This has the advantage that dephasing of the interband polarization, that has a strong effect on the high harmonic spectrum (as shall be seen later), can be included more easily. In this formalism, the intraband $\mathbf{j}_{\mathrm{ra}}$ and interband $\mathbf{j}_{\mathrm{er}}$ contribution to the current are [19]:

$$\mathbf{j}_{\mathrm{ra}}(t) = \sum_{\mathrm{m=c,v}} \int_{\overline{\mathrm{BZ}}} \mathbf{v}_{\mathrm{m}}[\mathbf{K}+\mathbf{A}(t)]\, n_{\mathrm{m}}(\mathbf{K},t)\, d^3\mathbf{K} \quad (2.6a)$$

$$\mathbf{j}_{\mathrm{er}}(t) = \frac{d}{dt} \int_{\overline{\mathrm{BZ}}} \mathbf{p}(\mathbf{K},t)\, d^3\mathbf{K}, \quad (2.6b)$$

where $\mathbf{v}_{\mathrm{m}}(\mathbf{k}) = \nabla_{\mathbf{k}} E_{\mathrm{m}}(\mathbf{k})$ is the velocity of electrons in band m, $n_{\mathrm{m}} = |a_{\mathrm{m}}|^2$ is the population of band m, and $\mathbf{p}(\mathbf{K},t) = \mathbf{d}[\mathbf{K}+\mathbf{A}(t)] a_c(\mathbf{K},t) a_v^*(\mathbf{K},t) + \mathrm{c.c.}$ is the interband polarization. The crystal momentum $\mathbf{k}$ has been transformed into a frame moving with the vector potential $-d\mathbf{A}/dt = \mathbf{F}$, $\mathbf{K} = \mathbf{k} - \mathbf{A}(t)$. As a result, the first Brillouin zone is also shifted to $\overline{\mathrm{BZ}} = \mathrm{BZ} - \mathbf{A}(t)$. The high-harmonic spectrum is obtained from the Fourier transform (FT) of $\mathbf{j}_{\mathrm{t}} = \mathbf{j}_{\mathrm{ra}} + \mathbf{j}_{\mathrm{er}}$, as $|\mathrm{FT}\{\mathbf{j}_{\mathrm{t}}\}|^2$.

A set of differential equations for the populations and the polarization can be derived from Eq. (2.3) by introducing the following definitions:

$$b_{\mathrm{m}} = a_{\mathrm{m}} e^{i \int_{-\infty}^{t} E_{\mathrm{m}} dt'}, \quad (2.7a)$$

$$n_{\mathrm{v}} = |b_{\mathrm{v}}|^2, \qquad n_{\mathrm{c}} = |b_{\mathrm{c}}|^2, \qquad \pi = b_{\mathrm{c}} b_{\mathrm{v}}^*. \quad (2.7b)$$

to obtain:

$$\dot{\pi}(\mathbf{K},t) = -\frac{\pi(\mathbf{K},t)}{T_2} + i\Omega^*(\mathbf{K},t)\, w(\mathbf{K},t)\, e^{iS(\mathbf{K},t)} \tag{2.8a}$$

$$\dot{n}_{\mathrm{m}}(\mathbf{K},t) = i s_m\, \Omega(\mathbf{K},t)\, \pi(\mathbf{K},t)\, e^{-iS(\mathbf{K},t)} + \mathrm{c.c.} \tag{2.8b}$$

where $w = n_{\mathrm{v}} - n_{\mathrm{c}}$ is the population difference between valence and conduction band; $s_{\mathrm{m}} = -1, 1$ for valence and conduction band, respectively and $\Omega(\mathbf{K},t) = \mathbf{F}(t)\cdot\mathbf{d}[\mathbf{K}+\mathbf{A}(t)]$ is the Rabi frequency. S is the classical action:

$$S(\mathbf{K},t) = \int_{-\infty}^{t} \varepsilon_g(\mathbf{K}+\mathbf{A}(t'))dt' \tag{2.9}$$

and $\varepsilon_g = E_{\mathrm{c}} - E_{\mathrm{v}}$ is the bandgap. The dephasing (T_2) term has been added phenomenologically; in principle, it could also be derived more formally by extending the theory to account for coupling to phonon bath and impurities and for electron-electron scattering [27].

Relation to the Optical Bloch Equations With the definitions $n_m = |a_m|^2$ and $\Pi = a_{\mathrm{c}}a_{\mathrm{v}}^*$, Eqs. (2.3) become the *Semiconductor Bloch Equations* [28]:

$$\dot{\Pi}(\mathbf{k},t) = F(t)\nabla_{\mathbf{k}}\Pi(\mathbf{k},t) - i\varepsilon_g(\mathbf{k})\Pi(\mathbf{k},t) - i\Omega(\mathbf{k},t)\, w(\mathbf{k},t) \tag{2.10}$$

$$\dot{n}_{\mathrm{m}}(\mathbf{k},t) = F(t)\nabla_{\mathbf{k}} n_{\mathrm{m}}(\mathbf{k},t) - 2\mathrm{Im}\{\Omega(\mathbf{k},t)\,\Pi^*(\mathbf{k},t)\} \tag{2.11}$$

They differ from the *Optical Bloch Equations* that describe two level systems by the terms $\propto \nabla_{\mathbf{k}}$, which are responsible for the acceleration of the electrons and holes in their respective bands. As a result, a two-bands periodic solid can be understood as a collection of coupled two-level systems, each system labelled by a different momentum, where the laser field transfers population between the systems.

The analytical solution. In order to better understand the physical processes driving intraband and interband high harmonic generation in solids, it is useful to explore Eqs. (2.8) by using the Keldysh approximation [1], $w(t) \approx 1$ in Eq. (2.8a). This decouples Eqs. (2.8) so that they can be formally integrated. Inserting the result into Eqs. (2.6), the spectra of the currents are obtained:

$$\begin{aligned}\mathbf{j}_{\mathrm{ra}}(\omega) = &\sum_{\mathrm{m=c,v}} s_{\mathrm{m}} \int_{-\infty}^{\infty} dt e^{-i\omega t} \left[\int_{\mathrm{BZ}} d^3\mathbf{k}\, \mathbf{v}_{\mathrm{m}}(\mathbf{k}) \int_{-\infty}^{t} dt' F(t') d^*(\boldsymbol{\kappa}_{t'})\times\right.\\ &\left.\times \int_{-\infty}^{t'} dt'' F(t'') d(\boldsymbol{\kappa}_{t''}) e^{iS(\mathbf{k},t'',t') - (t'-t'')/T_2} + \mathrm{c.c.}\right]\end{aligned} \tag{2.12a}$$

$$\mathbf{j}_{\mathrm{er}}(\omega) = \omega \int_{-\infty}^{\infty} dt e^{-i\omega t}\left[\int_{\mathrm{BZ}} d^3\mathbf{k}\, \mathbf{d}^*(\mathbf{k}) \int_{-\infty}^{t} dt' F(t') d(\boldsymbol{\kappa}_{t'}) e^{iS(\mathbf{k},t',t) - (t-t')/T_2} + \mathrm{c.c.}\right], \tag{2.12b}$$

where $\boldsymbol{\kappa}_{t'} = \mathbf{k} + \mathbf{A}(t') - \mathbf{A}(t)$. Further, the crystal momentum has been transformed back to the initial frame $\mathbf{k} = \mathbf{K} + \mathbf{A}(t)$, and $S(\mathbf{k},t',t) = \int_{t'}^{t} \varepsilon_{\mathrm{g}}(\boldsymbol{\kappa}_\tau)d\tau$. Note that

deriving Eqs. (2.12) directly from Eq. (2.3) would yield the same result except for the dephasing term. For the range of fields $F_0 \leq 0.008$ a.u., explored in experiments [16], the harmonic spectra obtained from Eqs. (2.12) and by using the full two-band equations (2.8) are practically identical. The Keldysh approximation might even be more robust in solids than in atoms because, contrary to atoms, it is difficult to achieve more than few percent in ionization without damaging the solid.

2.2 Interband harmonics and recollisions

The connection between the semiclassical model of recollisions in solids and the interband current is demonstrated in this section.

Theoretical derivation. Equation (2.12b) includes integrals of two oscillating functions: $F(t')$ and the complex exponential, with phase:

$$i\phi = iS(\mathbf{k}, t', t) - i\omega t - (t - t')/T_2. \tag{2.13}$$

ϕ oscillates faster than the electric field, because in typical experiments $\omega_0 \ll E_g$ (E_g is the minimum bandgap). Therefore, the integral would not build up, unless ϕ remains constant for some time. One can approximate the integrals with the saddle point method, which calculates the integrand around the points where the phase is stationary. These points are determined by:

$$\nabla_{\mathbf{k}}\phi = \int_{t'}^{t} \Delta\mathbf{v}(\mathbf{k} - \mathbf{A}(t) + \mathbf{A}(t''))dt'' = 0 \tag{2.14a}$$

$$\frac{d\phi}{dt'} = \varepsilon_{\mathrm{g}}[\mathbf{k} - \mathbf{A}(t) + \mathbf{A}(t')] - \frac{i}{T_2} = 0 \tag{2.14b}$$

$$\frac{d\phi}{dt} = \varepsilon_{\mathrm{g}}(\mathbf{k}) - \omega + \frac{i}{T_2} = 0. \tag{2.14c}$$

where $\Delta\mathbf{v}(\mathbf{k}) = \nabla_{\mathbf{k}}\varepsilon_{\mathrm{g}}(\mathbf{k}) = \mathbf{v}_{\mathrm{c}} - \mathbf{v}_{\mathrm{v}}$ is the difference of the velocities of the electron and the hole in their respective bands. To simplify the discussion it is useful to consider the limit $T_2 = \infty$. As shall be seen later, neglect of dephasing does not alter the physical picture down to $T_2 \approx 1$ fs. The above equations yield an intuitive semiclassical description of interband harmonics. This description is detailed below.

1. $\Delta\mathbf{x}_{\mathrm{m}} = \int_{t'}^{t} \mathbf{v}_{\mathrm{m}} dt'' = \mathbf{x}_{\mathrm{m}}(t) - \mathbf{x}_{\mathrm{m}}(t')$ is the distance propagated by electrons/holes in the conduction/valence band ($\mathrm{m} = \mathrm{c}, \mathrm{v}$) between time of birth t' and time of observation t. Therefore, Eq. (2.14a), reads $\nabla_{\mathbf{k}}\phi = \Delta x_c - \Delta x_v = 0$. Since electrons and holes are born at the same position, the condition implies that *high harmonics are emitted only upon re-encounter of each electron with its associated hole.*

2. Because $\varepsilon_g(\mathbf{k}) \geq E_g \geq 0$, Eq. (2.14b) can only be solved for complex t'. The imaginary part of t' describes the tunnelling of electrons from the valence to

the conduction band, a necessary parameter to calculate the tunnelling rate. An exact solution of this equation for an arbitrary band structure is not known yet. However, one can neglect the influence of the tunnelling step by setting $E_g = 0$. In this case, by writing $\varepsilon_g(\mathbf{k}) = E_g + h(\mathbf{k})$, with $h \geq 0$, Eq. (2.14b) reads $h[\mathbf{k} - \mathbf{A}(t) + \mathbf{A}(t')] = 0$. The latter is solved for:

$$\mathbf{k} = \mathbf{k_0} + \mathbf{A}(t) - \mathbf{A}(t'), \tag{2.15}$$

where $\mathbf{k_0}$ is the *minimum* direct band gap. The equation reduces to Eq. (1.5) in the case that the minimum direct band gap is at zero crystal momentum ($\mathbf{k_0} = 0$). The solution of Eq. (2.14b), in summary, implies that *electron-hole pairs, after their birth through tunnelling across a direct band gap at* $\mathbf{k} = \mathbf{k_0}$*, accelerate in the reciprocal space according to Eq. (2.15).*

3. Finally, Eq. (2.14c) is conservation of energy. Upon recollision at time t, *each electron recombines with its associated hole and emits a high harmonic photon with energy equal to the bandgap at the time of recollision:* $\omega = \varepsilon_g[\mathbf{A}(t) - \mathbf{A}(t')]$. Therefore, the recombination step, which is not apparent in the quantum picture of interband emission arising from the interference of the electron and hole wavepackets, is necessary to explain the energy transfer between electrons and high harmonic photon modes in a second quantization formalism.

In general, solution of the saddle point equations yields complex-valued saddle points t'_{st}, t_{st}, $\mathbf{k}_{st}$. A beautiful summary of the complete (complex) physical picture of high harmonic generation can be found in Ref. [29] for the atomic case. Among other effects, the complex solutions are able to explain the generation of harmonics below the minimum energy gap. Complex values arise from the requirement that the electron and hole need to meet at exactly the same position. This requirement is an *artifact* of neglecting the size of the electron and hole in the saddle point analysis. It is also discussed in Ref. [29] for the atomic case.

Results of the simulations. The semiclassical analysis of the interband polarization is confirmed by numerical integration of Eqs. (2.8). The time-dependent inter- ($\mathbf{j}_{\mathrm{er}}$) and intraband ($\mathbf{j}_{\mathrm{ra}}$) currents are then calculated with Eqs. (2.6). Their spectrum is reported in Fig. 2.1 for two different values of the dephasing time T_2. Details about the simulation are reported in appendix A. The spectrum of both currents exhibit an extended plateau from the minimum bandgap of the material (corresponding to the 9^{th} harmonic order, marked by the black dashed vertical line) up to the 25^{th} order. The plateau in the interband current arises from the recollision and recombination of electron-hole pairs. In section 2.3 it will be shown that the plateau in the intraband current also bears the signature of recollisions.

To demonstrate the role of recollisions in the plateau of the interband current, one can look at the variation of the harmonic frequency with time in this spectral region, the hallmark of the recollision process as introduced in Ch. 1.2. For the purpose, a windowed Fourier transform is performed in the following way:

$$\mathbf{j}(\omega, \tau) = \int_{-\infty}^{\infty} W(t - \tau)\mathbf{j}(t)e^{-i\omega t}\, dt \tag{2.16}$$

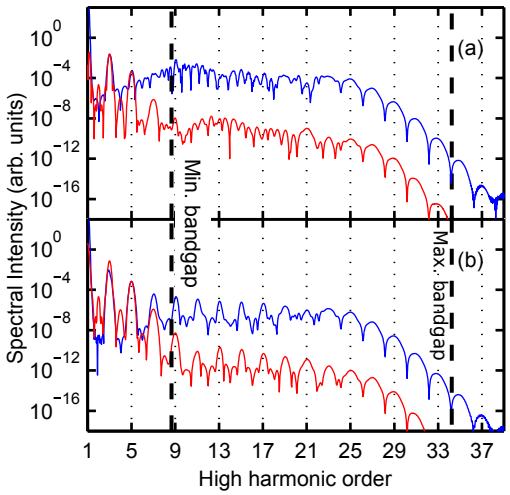

Figure 2.1: Harmonic spectrum for interband ($|FT\{\mathbf{j}_{\mathrm{er}}\}|^2$, blue line) and intraband ($|FT\{\mathbf{j}_{\mathrm{ra}}\}|^2$, red line) currents for a field strength $F_0 = 0.003$ a.u.; the cosine laser field with $\omega_0 = 0.014$ a.u. ($\lambda = 3.25\ \mu$m), corresponding to a laser period $T_0 = 2\pi/\omega_0 = 10.9$ fs, is multiplied by a temporal Gaussian envelope with a FWHM of ten cycles. The dephasing time is **(a)** $T_2 = \infty$ and **(b)** $T_2 = T_0/4$. The laser polarization is along the $\Gamma - M$ direction of the reciprocal space of a wurtzite ZnO crystal. Details about the crystal and its band structure are given in appendix A. The dashed vertical black lines mark the minimum band gap at the center of the Brillouin zone (at 3.4 eV) and the maximum band gap at the edge of the Brillouin Zone (at 13 eV).

Here, the interband time-dependent dipole is multiplied by a Blackman window function W which is narrow compared to the fundamental laser cycle (the window is only 0.34 cycles wide). The spectrum of the resulting dipole is recorded as a function of the delay between the window and the laser cycle, thereby returning a 2D map of the emission in time and frequency – a spectrogram.

The spectrograms are shown in Fig. 2.2(e-h) for increasing field strengths (from **e** to **h**). The spectral intensity of the interband dipole is color coded. At each laser half-cycle, the high harmonic frequency increases, reaches a maximum, and decreases. The solid white line, instead, is the prediction of the semiclassical model. Panel (f) shows the same data as in Fig. 1.4(c), plotted as a function of time rather than birth time. The near perfect agreement between the simulated spectrum and the prediction of the semiclassical model confirms that *recolliding electron-hole pairs are responsible for the generation of interband high harmonics, at the given laser frequency.*

There is a slight discrepancy however: the simulated cut-off is slightly higher than in the semiclassical calculation. This deviation arises from neglecting the ionization process in the semiclassical calculation (a full calculation requires finding the complex solutions to the saddle point Eqs. 2.14).

A thorough validation of the semiclassical model can be performed with the aid of simulations. Panels (a)-(d) show the classically calculated harmonic order as a function of time for the same field strengths of the right panels. Electrons born at a specific time can recollide with the hole multiple times. These higher returns are

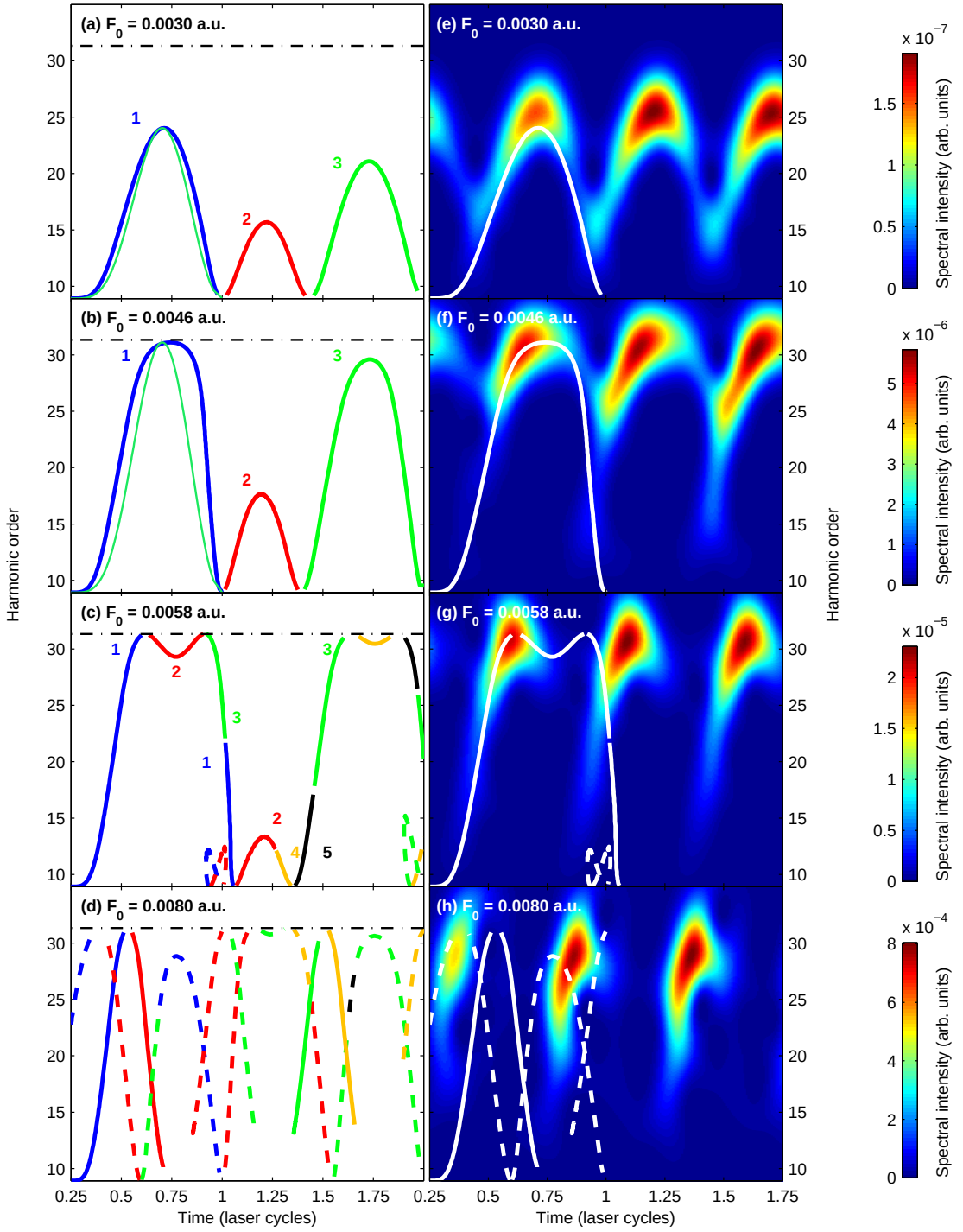

Figure 2.2: **(a-d, left panels)** High harmonic photon energy as a function of time for generation in a ZnO crystal at various field strengths. Subsequent recollision events are numbered sequentially and color coded as follows: **first**, **second**, **third**, **fourth**, **fifth**. Solid (dashed) lines are for pairs created after (before) the peak of the field. The thin green line in panels (a-b) is the recollision energy of atomic high harmonics normalized to the cut-off of the crystal case. The dashed-dotted black line is the maximum bandgap at the edge of the Brillouin Zone. **(e-h, right panels)** Simulated high harmonic spectral intensity (color code) as a function of harmonic order (vertical axis) and time (horizontal axis). The classical trajectories recolliding within the cycle, found in (a-d), are the solid and dashed white lines. Replicas of this emission at following laser half-cycles arise from the intrinsic periodicity of the generation process.

color coded from the first (blue) to the fifth (black). The thin green line in panels (a)-(b) represents the energy of the first recollision in an atomic system, for a field strength that yields the same cut-off; for the atomic system it is assumed that the ionization potential $I_p = E_g$. In panels (e)-(h) only recollisions within the first laser cycle are plotted (solid white line). Several points can be made.

- *Existence of generalized trajectories.* Whereas the atomic trajectories are independent of the field strength (as illustrated in Chap. 1), in a crystal they are not. For example the blue line in Fig. 2.2(b), calculated with $F_0 = 0.0046$ a.u., is distorted with respect to that of Fig. 2.2(a), where $F_0 = 0.003$ a.u. For the higher field, the cut-off originates from trajectories that are born and recollide almost 10° later in the cycle as compared to the lower field case. The differences between solids and atoms become even more pronounced as the field is further increased, see Figs. 2.2(c-d). This striking difference is a consequence of the non-parabolic band dispersion. For higher field strengths, electrons and holes start to explore the non-quadratic part of the band. When this happens, the quadratic energy-momentum relation and therewith the velocity is strongly modified and the trajectories are no longer invariant with respect to the field strength.

Similar to atomic high harmonic generation, the cut-off energy separates two sets of trajectories that recollide within one optical cycle and contribute to the same harmonic order. Those that travel a longer time, the *long* trajectories, are born after the peak of the field but before the birth time of the cut-off trajectory t'_c; the *short* trajectories instead are born at times later than t'_c.

- *The cut-off can saturate.* For field strengths $F_0 \leq 0.0046$ a.u., the cut-off is below or equals the maximum possible photon energy (black dashed-dotted line), which is determined by the maximum energy difference between valence and conduction bands. The *long* and *short* branches are clearly identifiable. When the intensity is increased further, see Figs. 2.2(c-d), the cut-off saturates. As a result, the simple long/short trajectory picture is lost. For $F_0 = 0.0058$ a.u., Fig. 2.2(c), the same electron-hole pairs undergo up to three recollisions near the cutoff energy before the long trajectories recollide the first time.

  For $F_0 = 0.008$ a.u., Fig. 2.2(d), long trajectories do not recollide at all, but short trajectories can recollide a second and a third time within the optical cycle. This field strength corresponds to ~ 0.43 $V/\text{Å}$ in the crystal. With the refractive index $n = 1.8992$ of ZnO at $\lambda = 3.62$ μm, it corresponds to $F_{\text{vac}} = 0.62$ $V/\text{Å}$, which has been reached in experiments [16].

- *Trajectories born before the peak can recollide.* For $F_0 = 0.008$ a.u., harmonic emission is shifted at earlier times starting from the field zero (at 0.25 cycles, marked by the dashed blue line in panel **d**). This emission is associated to recolliding trajectories born before the peak of the field. In the atomic case, this can only happen if the Coulomb attraction between electrons and holes is

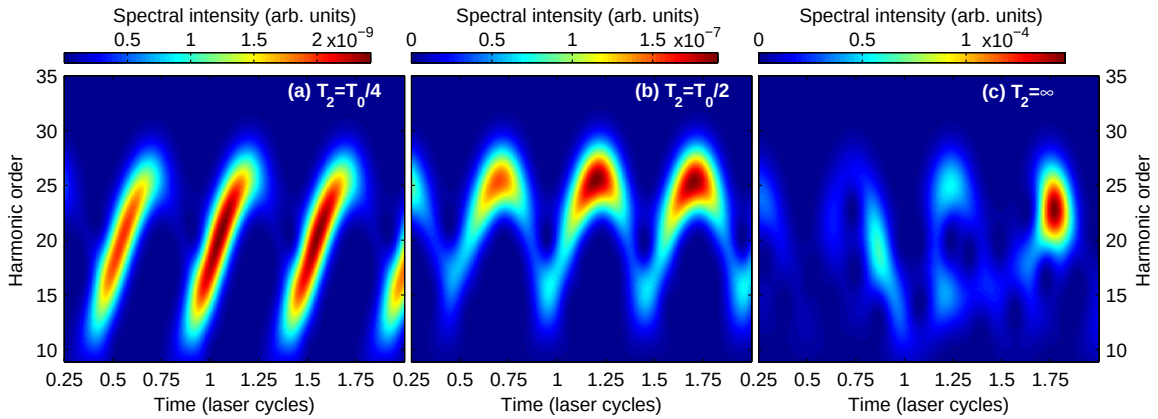

Figure 2.3: Harmonic order versus time for three different dephasing times: **(a)** $T_2 = T_0/4$, **(b)** $T_2 = T_0/2$, **(c)** $T_2 = \infty$. The laser frequency is $\omega_0 = 0.014$ a.u. and the field strength is $F_0 = 0.003$ a.u. The shorter the dephasing time the weaker the long trajectories are. In (c) multiple returns significantly modify the recollision.

considered. Excitonic interaction is not included in the simulations presented here, so this effect arises solely from the generalized motion of electron-hole pairs in solids.

Another discrepancy is the absence in the simulations of multiple recollisions, labelled "2" and "3" in Fig. 2.2(a,b). In atomic high harmonic generation, long returns are (i) suppressed by quantum diffusion of the wavepacket, which results in a small recombination cross section between free electrons and the atomic ground state and (ii) difficult to detect because their large dipole phase results in extremely curved phase fronts, ultimately leading to highly divergent beams.

In solids, in addition to the atomic effects, short dephasing times (≈ 5 fs) could contribute to the suppression of higher-order returns. Dephasing also weakens the long trajectory contribution. The weakening is confirmed by the trajectory analysis of Fig. 2.3, for $T_2 = T_0/4$ (a), $T_0/2$ (b) and $T_2 = \infty$ (c). For increasing dephasing times the spectral intensity of the long trajectories becomes stronger. When the dephasing time is long enough to allow returns longer than a laser cycle (c), multiple recollisions interfere and, together with the varying intensity of the pulse envelope, lead to aperiodic photon emission[3]. This results in the loss of the clear harmonic structure in the spectrum, as shown in Fig. 2.1(a). The simulation suggests that dephasing could play an important role in high harmonic generation.

[3]If a CW laser is used instead, the emission is still periodic and only the odd harmonics constructively interfere. However, multiple returns modulate their intensity.

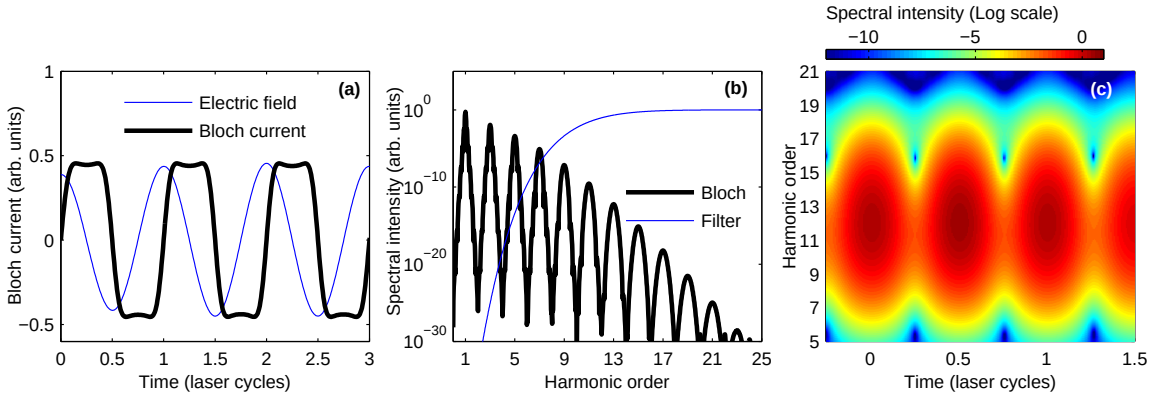

Figure 2.4: Properties of Velocity harmonics. **(a)** Electrons (black line) move asynchronously with the laser field (blue line) because their velocity is determined by the band dispersion. **(b)** The spectrum (black line) decreases monotonically with harmonic order. **(c)** The spectrogram (spectral intensity is in logarithmic scale) reveals emission in phase at each field crest. The blue line in panel (b) filters out the dominant low-order harmonics in the windowed Fourier transform. The laser frequency is $\omega_0 = 0.014$ a.u. and the field strength is $F_0 = 0.003$ a.u.

2.3 Mechanisms of intraband emission

There are several mechanisms responsible for intraband emission. The intraband current is defined by Eq. (2.6a):

$$\mathbf{j}_{\mathrm{ra}}(t) = \sum_{\mathrm{m=c,v}} \int_{\overline{\mathrm{BZ}}} \mathbf{v}_{\mathrm{m}}[\mathbf{K}+\mathbf{A}(t)]\, n_{\mathrm{m}}(\mathbf{K},t)\, d^3\mathbf{K}$$

First, harmonics are emitted by the nonlinearity of the band velocities $\mathbf{v}_{\mathrm{m}}[\mathbf{K}+\mathbf{A}(t)]$, which results in the nonlinear oscillations of electrons and holes represented by the black line in Fig. 2.4(a). When the electron is accelerated across the entire Brillouin Zone, it undergoes a Bloch oscillation. Consequently, the emitted harmonics are dubbed *Bloch harmonics*. However, the electron need not to be accelerated so strongly to generate harmonics. Therefore, to avoid confusion, these harmonics will be named *velocity harmonics*. They have been extensively studied in the literature in the context of high harmonic generation [28, 16, 18]. Their spectrum can be analytically solved, and the motion characterized by the dimensionless parameter ω_B/ω, where $\omega_B = Fd$ (in a.u.) is the *Bloch frequency*.

Typically, velocity harmonics decrease in intensity rapidly with harmonic order (black line in Fig. 2.4**b**). The windowed Fourier transform (Fig. 2.4**c**) reveals that these harmonics are emitted in phase as discrete bursts at each peak of the laser field, when the acceleration of the electron is maximum (see panel **a**). The absence of spectral phase results from the time-reversal symmetry of the oscillations. The properties of the Fourier transform, in fact, demand that if $\mathbf{v}_{\mathrm{m}}(t) = \mathbf{v}_{\mathrm{m}}(-t)$, then $\mathbf{v}_{\mathrm{m}}(\omega) = \mathbf{v}^*{}_{\mathrm{m}}(\omega)$, where * indicates complex conjugation. Therefore, $\mathbf{v}_{\mathrm{m}}(\omega) \in \mathbb{R}$.

Second, harmonics arise from the nonlinearity of tunnel ionization, embedded in $n_{\mathrm{m}}(\mathbf{K},t)$, that results in almost step-like increase (decrease) in the conduction (va-

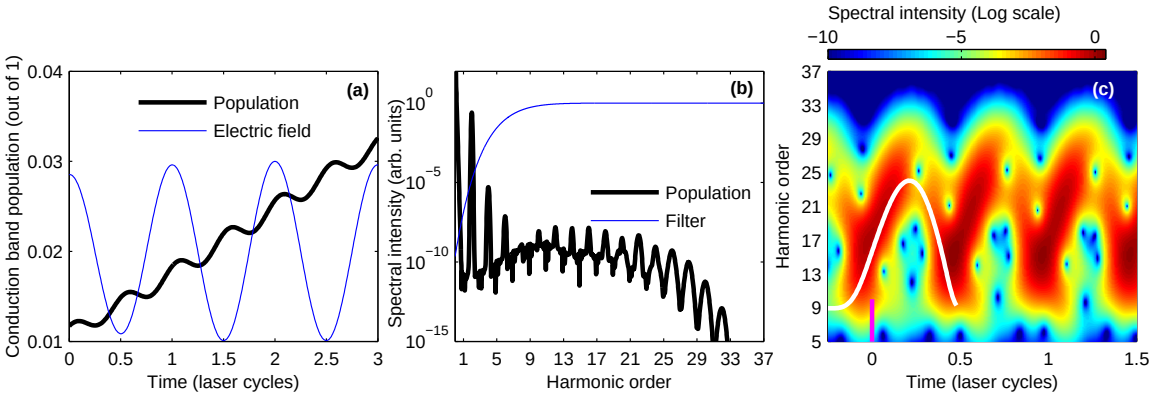

Figure 2.5: The conduction band population (black line in panel **a**) increases almost step-like at each field crest (laser field is the blue line). The dynamics generate a broad harmonic plateau (panel **b**, black line), and low order harmonics of rapidly decreasing intensity. Harmonics in the plateau are emitted at the time of recollision (solid white line in panel **c**), whereas low order harmonics are all emitted in phase (dashed magenta line). The laser frequency is $\omega_0 = 0.014$ a.u. and the field strength is $F_0 = 0.003$ a.u.

lence) band population. The momentum-integrated population in the conduction band is plotted in Fig. 2.5(a). The generation of harmonics by means of tunnel ionization was predicted by Brunel for the atomic case [30]. Typically, the spectrum consists of low-order harmonics of rapidly decreasing intensity (see panel **b**, black line). Panel (c) shows that Brunel harmonics are emitted in phase (marked by the dashed magenta line, up to the 9^{th} harmonic order).

Third, the intraband current also contains a recollision-like contribution that depends on the polarization buildup between electrons and holes. This contribution arises from the exponential term containing the semiclassical action S in Eq. (2.12a). Like Brunel emission, it is also embedded in $n_{\mathrm{m}}(\mathbf{K}, t)$. However, it gives rise to a broad spectral plateau in Fig. 2.5(b), all in all similar to the interband one. In fact, these harmonics are emitted at the time of recollision, as shown by the solid white line in panel (c). The position of the crossover between Brunel harmonics and the recollision-like mechanism, at $\omega \sim E_g$ in Fig. 2.5, depends on the dephasing time. For short dephasing times, recollision is less significant because of the loss of coherence between electrons and holes. Therefore, the plateau is weaker and the crossover shifts to higher harmonics.

In conclusion, only recolliding electron-hole pairs give rise to a variation of the emitted high harmonic order in time. For all other mechanisms, harmonic emission is in phase. This feature will be exploited to find the signature of recolliding hole-pairs in the experiment presented in section 3.1.

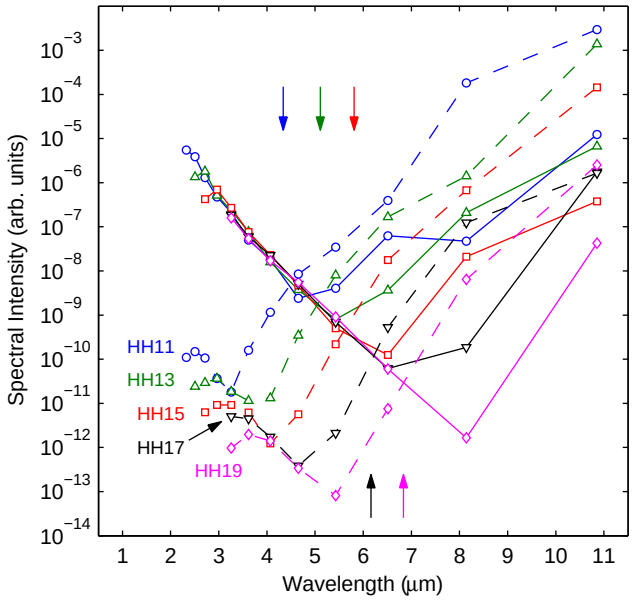

Figure 2.6: Theoretical prediction of harmonic intensity versus laser wavelength for various high harmonic orders; circles, triangles pointed upward, squares, triangles pointed downward, and diamonds refer to order 11, 13, 15, 17, and 19, respectively. The solid and dashed lines show the interband and intraband contributions for $T_2 = 2.7$ fs ($T_0/4$ for $\lambda = 3.25$ μm), respectively. The field strength is kept constant at $F_0 = 0.003$ a.u. and the laser frequency is $\omega_0 = 0.014$ a.u. The laser polarization is along the $\Gamma - M$ direction of a wurtzite ZnO crystal. Details about the crystal and the band structure are given in appendix A. The arrows mark the wavelength above which a given harmonic falls below the minimum bandgap.

2.4 Relative importance of interband and intraband currents

Figure 2.1 predicts that interband harmonics above the minimum bandgap of the material are orders of magnitude stronger than intraband harmonics. Figure 2.6 investigates how interband (solid lines) and intraband (dashed lines) contributions scale with laser wavelength, for a fixed field strength $F_0 = 0.003$ a.u. The arrows mark the wavelengths above which a given harmonic order falls below the minimum band gap. For the chosen dephasing time ($T_2 = T_0/4$), as long as high harmonics are above the band gap, interband emission dominates. For shorter dephasing times, intraband harmonics gain more weight and the points where interband and intraband emission intersect move slowly to shorter wavelengths; however, down to $T_2 \approx 1$ fs, interband emission remains dominant over most of the displayed wavelength range. The crossing point also depends on field strength. It varies by about 1 μm with field strengths in the range $F_0 = 0.003 - 0.1$ a.u.

The interband contribution drops exponentially with increasing wavelength. This can be attributed mostly to the dephasing term in Eq. (2.12b): as the excursion time $t - t'$ increases with λ, the amplitude decreases $\propto \exp[(t - t')/T_2]$. The longer the electron is separated from the hole, the higher the chance to endure collisions, which lessen the coherence they have with respect to one another.

The wavelength dependence of the intraband yield is more complex. It most likely results from a mixing of the different mechanisms identified above and can even increase for longer wavelengths. For wavelengths below $\sim 5\ \mu m$, intraband emission drops as fast as interband emission. Here, harmonics come from the recollision-like mechanism, and are therefore as prone to dephasing. At longer wavelengths, velocity or Brunel harmonics dominate, as indicated by the rapid decrease of spectral intensity with harmonic order. Here, the intraband contribution increases with wavelength. This increase is possibly caused by electrons and holes traversing the Brillouin Zone more than once in half-laser cycle, and therefore undergoing more oscillations in the same cycle fraction. Therefore, the spectral intensity increases.

In summary, the analysis indicates a clear distinction between two regimes: for wavelengths below $\sim 5\mu m$, interband harmonics dominate, whereas intraband emission from Bloch or Brunel mechanisms dominates for longer excitation wavelengths. The prediction seems in line with recent experiments performed at 10 μm wavelength, where the signature of Bloch oscillations has been found in the simultaneous emission of harmonics at the peaks of the driving laser field [17, 31].

Chapter 3

Experimental evidence of recollisions

Two experiments I performed during my PhD on ZnO and Si crystals are presented in this chapter. High harmonic spectra from both crystals show evidence of the recollision between electrons and holes. This is the major observation.

The signature of recollision is obtained by perturbing the high harmonic generation process with a second harmonic field, thereby producing even harmonics. Second harmonic fields as weak as few $V/\mu m$, below the DC breakdown threshold, are sufficient to produce even harmonics. This extreme sensitivity to perturbing fields opens the possibility to integrate electronics with high harmonics, for example to image such fields in actual semiconductor circuits. This is the second major observation.

The experiment in silicon also suggests that during the tunnelling step electrons undergo a vertical transition across the direct band gap, confirming a previous investigation [13] where energies of the photo-excited electrons in excess of the minimum (indirect) band gap have been measured. Furthermore, the modulation of the spectral intensity with crystallographic orientation with respect to the laser polarization suggests that high harmonics are sensitive to the relative alignment between polarization and bond directions.

The material presented in this chapter in based on two publications of mine [32, 33]. The technique employed to perturb the generation process has been adapted from atomic experiments, so its understanding in terms of simple optical interferometers presented at the beginning of section 3.1 is well known [34]. The analysis of the effect of the band structure on the dipole phase presented in section 3.3, and on the temporal chirp of the harmonic pulses presented in section 3.4, are new (although the chirp in atomic high harmonic generation is well studied by the scientific community).

3.1 High harmonic generation from ZnO

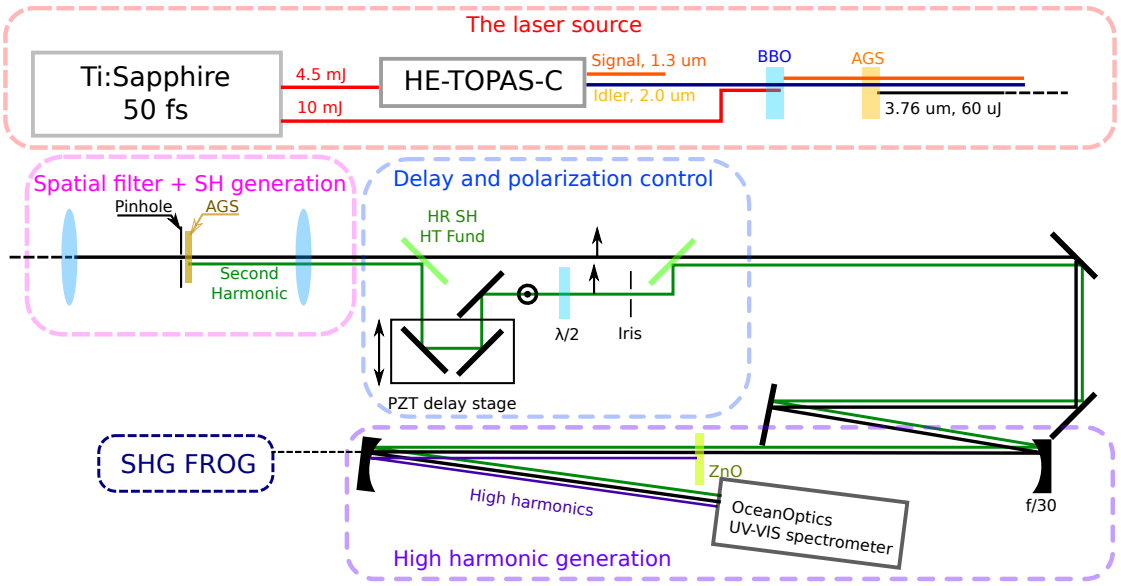

Figure 3.1: Sketch of the experimental setup.

The experimental setup. The experimental setup is sketched in Fig. 3.1. The laser source delivers mid-infrared laser pulses with center wavelength of 3.76 μm, energy of 60 μJ and pulse duration of 95 fs. These mid-infrared pulses are obtained by difference frequency generation in a 400 μm thick $AgGaS_2$ (AGS) crystal between the signal and idler of a commercial Optical Parametric Amplifier (LightConversion HE-Topas-C) pumped by 4.5 mJ of Ti:Sapphire 800 nm laser pulses. The output of the OPA is further amplified in a Beta Barium Borate (BBO) crystal pumped by 10 mJ of 800 nm pulses. The mid-infrared beam is spatially filtered with a pin-hole.

High harmonics are generated by focusing the mid-infrared pulses with f/30 spherical Ag mirror into a 500 nm thick ZnO single crystal, wurtzite phase, epitaxially grown over a 0.5 mm thick sapphire substrate. Both crystals are oriented with their c-axis, or the [0001] direction, aligned along the laser k-vector. The sample is oriented with the sapphire side facing the incoming beam. The pulse energy incident on the sample is 19 μJ. The peak intensity inside the sample is 0.85 TW/cm^2 (0.25 V/Å), which is calculated from the vacuum intensity accounting for reflection loss: $F_0 = 2F_{\text{vac}}/(n+1)$. Here, $n = 1.8971$ is the refractive index of ZnO at the mid-infrared wavelength. The vacuum intensity is calculated by independently measuring the pulse energy, duration, and the focus size. The pulse duration is measured with a dispersion-free SHG FROG (Frequency-Resolved Optical Gating) after the ZnO crystal. The focus size is measured with the knife-edge technique. The fundamental spectrum before and after the crystal is not visibly different, demonstrating that self-phase modulation is negligible. Likewise, because the incident peak power $P = 1.76 \times 10^8$ W is below the critical power for self-focusing $P_{cr} = 2.2 \times 10^8$ W (assuming a nonlinear refractive index for Sapphire of $n_2 = 5.4 \times 10^{-21}$ W [35]), self-focusing should also be negligible.

The high harmonics are focused with a spherical Al mirror on the entrance slit

of a visible-ultraviolet spectrometer from OceanOptics. The detected wavelength range is from 200 nm to 900 nm. Figure 3.2 shows the harmonic signal with respect to the fundamental intensity. An initial sharp rise in harmonic signal is followed by a much slower increase, in agreement with a previous experiment [16]. The scaling is roughly irrespective of the harmonic order, in contrast with predictions of conventional non-linear optics. Thus, the harmonics are non-perturbative.

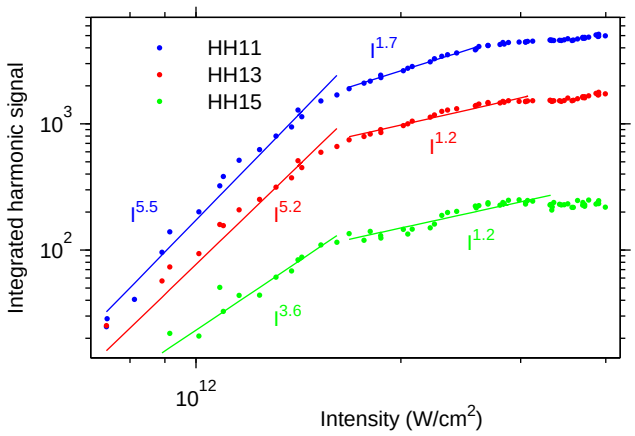

Figure 3.2: High harmonic signal integrated over the spectral width as a function of the fundamental intensity. For this particular experiment, the sample is a 500 μm thick single ZnO crystal. The scaling is non-perturbative and resembles the one reported in the literature [16].

To determine if high harmonics originate from a recollision mechanism, a weak second harmonic field is added to the strong mid-infrared fundamental field. The second harmonic is generated in a 300 μm thick AGS crystal optimized for Type-I generation[1], positioned right after the pinhole to exploit the high intensity of the focussed fundamental beam and its high quality resulting from the spatial filter. The two colours are separated and recombined with dichroic beam splitters that reflect the second harmonic. The polarization of the latter is rotated parallel to the fundamental before the recombining mirror. The energy of the second harmonic is controlled with an iris. The delay between the two colours is varied with a PZT stage on the second harmonic arm.

The addition of the second harmonic breaks the symmetry between successive half-cycles of the laser field. The broken symmetry results in the appearance of even harmonics. The recorded spectrum, as a function of delay between the two colours, is shown in Fig. 3.3, for a second harmonic intensity of 9×10^{-6} times that of the fundamental. The extremely weak second harmonic field does not significantly modify the spectrum of the odd harmonics that would be obtained in the fundamental field alone. Therefore, it is not reported here.

[1]In Type I SHG, the fundamental and the second harmonic are orthogonally polarized, along the ordinary and extraordinary axis respectively.

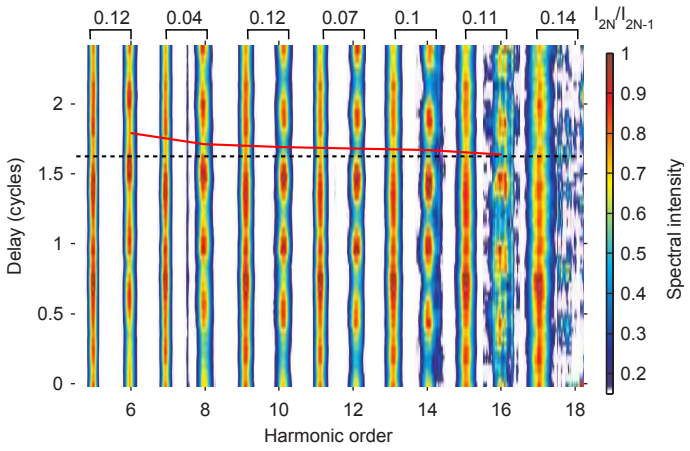

Figure 3.3: Measured high harmonic spectra versus the delay between the two colours (in cycles of the second harmonic); the spectral intensity is colour-coded (key at right). The even harmonic intensity modulates every half-cycle. The odd harmonics also modulate, but the modulation is extremely weak. In fact, their intensity is almost unaffected by the second harmonic field. The phase of the even harmonic modulation depends on the harmonic order, as evidenced by the red solid line relative to the black reference line (the red line links the minima in the modulation of the even harmonics). Each harmonic order is separately normalized. The relative intensity between even-order and adjacent odd-order harmonics is given at the top (I_{2N}/I_{2N-1}).

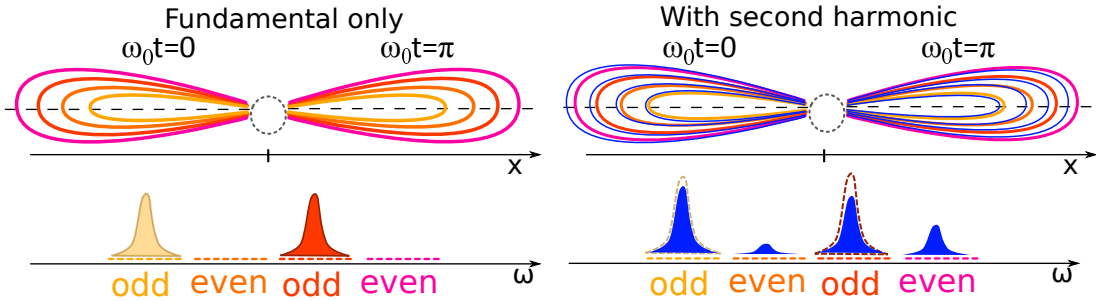

Figure 3.4: The (discrete) harmonic structure arises from temporal interference of emission from each atom at each laser half-cycle. Each interferometer is associated to a specific harmonic order. Each arm of the interferometer corresponds to propagation in two successive laser half-cycles. (top left) In the fundamental field alone, electrons propagate equal distance to the left and to the right of the origin (marked by the hollow grey dashed circle) in two subsequent half-cycles. Four trajectories are depicted, color coded to the harmonic photon energy emitted upon recollision. Propagation in each half-cycle corresponds to an arm of an interferometer. (bottom left) Only interferometers associated to odd harmonics result in constructive interference at the output. (top right) A properly phased second harmonic field stretches trajectories in the first half cycle, while it shrinks them in the next half cycle (blue lines). (bottom right) In this case the interferometer is unbalanced. This results in partially constructive interference of the even harmonics. The higher the even harmonic signal, the more the phase difference between the two arms.

The method. To understand the origin of the even harmonics, it is useful to think of high harmonic generation as a collection of interferometers, each interferometer associated to emission of a specific harmonic photon energy, and in which each arm of the interferometer corresponds to trajectories of electron-hole pairs launched at subsequent laser half-cycles (see Fig. 3.4). The length of each arm is determined by the phase of the dipole, $\exp[iS]$, where S is the semiclassical action accumulated between the time of birth and of recollision:

$$S(\mathbf{k}, t', t) = \int_{t'}^{t} \varepsilon_{\mathrm{g}}\left(\boldsymbol{\kappa}_{\tau}\right) d\tau \tag{3.1}$$

with $\boldsymbol{\kappa}_{t'} = \mathbf{k} + \mathbf{A}(t') - \mathbf{A}(t)$.

In the fundamental field alone, each interferometer is balanced: the length of the two arms is equal but oppositely phased, corresponding to electrons (holes) travelling equal distance to the left (right) in the first half-cycle and to the right (left) in the next half-cycle (see top-left part of Fig. 3.4). Mathematically, the dipole moment $d(t) = -d(t + \pi/\omega_0)$. The total dipole oscillating at the frequency $n\omega_0$ is the coherent addition of the two arms:

$$\begin{aligned} p(t) &= d(t)e^{in\omega_0 t} + d(t + \pi/\omega_0)e^{in\omega_0(t+\pi/\omega_0)} \\ &= d(t)e^{in\omega_0 t}\left[1 - e^{in\pi}\right] \end{aligned}$$

Clearly, the two arms constructively interfere only for interferometers associated to emission at the odd harmonics (n = odd), as illustrated in the bottom-left part of Fig. 3.4.

A second harmonic field properly phased to the fundamental breaks the symmetry between successive half cycles. When the second harmonic adds to the fundamental field in the first half-cycle it brings electrons a little further from their holes, while they are brought a little closer in the next half-cycle, when fundamental and second harmonic subtract (see top-right part of Fig. 3.4). In *optical* language, the interferometers are unbalanced: phase is added to one arm while it is removed from the other. The total phase in each arm is:

$$S_2 \simeq S_1 + \sigma(t, \phi) = S_1 + \int_{t'}^{t} \Delta\mathbf{v}(\boldsymbol{\kappa}_{\tau})\mathbf{A}_2(\tau, \phi)\, d\tau \tag{3.3}$$

where S_1 is the phase accumulated in the fundamental field alone (Eq. 3.1 with $\mathbf{A}(t)$ equal to the vector potential of the fundamental field), $\mathbf{A}_2(\tau, \phi) = \mathbf{A}_2 \cos(2\omega_0\tau + \phi)$ is the vector potential of the second harmonic and $\Delta\mathbf{v}(\mathbf{k}) = \nabla_{\mathbf{k}}\varepsilon_g(\mathbf{k})$ the difference of the velocities of electrons and holes. The above formula can be derived by expanding Eq. (3.1) for small $\mathbf{A}_2$. Because $\sigma(t, \phi) = -\sigma(t + \pi/\omega_0, \phi)$, the total phase difference between the two arms amounts to 2σ. The uneven length of the arms of the interferometers modifies the interference as follows:

$$p(t) = d_1(t)e^{in\omega_0 t}\left[e^{i\sigma(t,\phi)} - e^{-i\sigma(t,\phi)}e^{in\pi}\right] = \begin{cases} 2d_1(t)e^{in\omega_0 t}\cos(\sigma) & \text{if } n \text{ is odd,} \\ 2id_1(t)e^{in\omega_0 t}\sin(\sigma) & \text{if } n \text{ is even.} \end{cases}$$

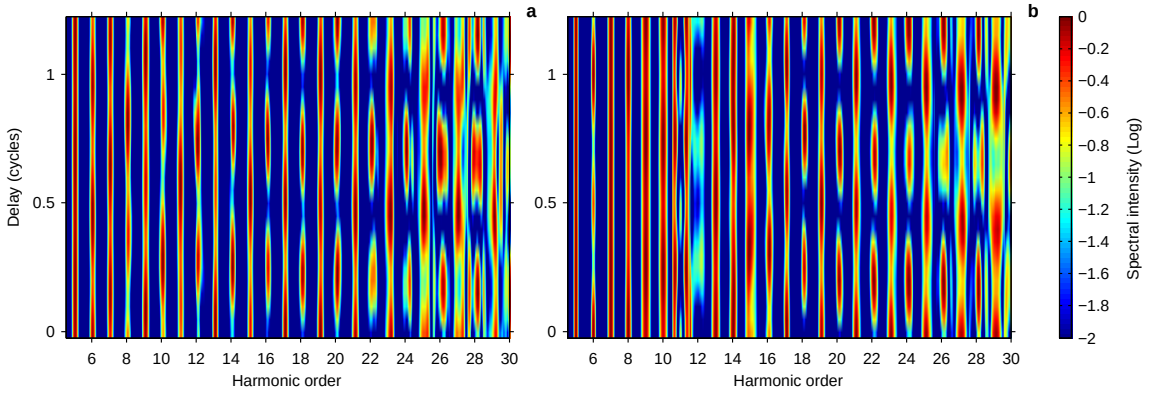

Figure 3.5: Simulated spectrograms for interband (**a**) and intraband (**b**) emission. Intensity is colour-coded on a logarithmic scale. Each harmonic order has been normalized to simplify comparison. The modulation depth is close to 100% for both intra- and interband generated above bandgap harmonics. It drops to $\sim 50\%$ for below bandgap interband harmonics and for harmonics below the 18^{th} for intraband emission. The laser parameters are: $\omega_0 = 0.0121$ a.u., $F_0 = 0.0049$ a.u., $F_{2\omega} = 10^{-2}F_0$.

where d_1 is the dipole due to the fundamental field alone. Even harmonics are now generated. Their intensity is proportional to the amount of added phase, $I_{2N} \propto |\sin(\sigma)|^2$, as illustrated in the bottom-right part of Fig. 3.4.

In optics, the interference can be continuously modified by moving one arm of the interferometer with respect to the other. By varying the delay between fundamental and second harmonic, the asymmetry between successive half cycles felt by the electrons can be continuously adjusted. As a result, the even harmonic intensity modulates with a period of half of the second harmonic cycle (see Fig. 3.3). Maximum even harmonic intensity is reached at an optimum phase Φ_{osc}, where the asymmetry is strongest. The red line in Fig. 3.3 links Φ_{osc} between all even harmonic orders. Because different trajectories are born and recollide at different times, each feels the second harmonic field differently. Therefore Φ_{osc} differs between harmonic orders (as evidenced by comparison with the flat dashed black line in Fig. 3.3). This behaviour is observed in gases as well.

The findings. To compare Φ_{osc} with theoretical predictions, the experiment is simulated using the two-band model introduced in Chap. 2, for a second harmonic field strength of 6×10^{-4} relative to the fundamental. This ensures that the even harmonics are $\sim 5\%$ of the odd ones, similar to the experiment (Φ_{osc} is rather insensitive to the strength of the perturbing field, as long as the even harmonics remain "small"). The simulations cannot account for spatial averaging over the gaussian beam profile, which can cause loss of contrast in the modulation and variations in Φ_{osc}. Spatial averaging can be easily avoided in the experiment by filtering the beam after the crystal. Temporal averaging, on the other hand, is accounted for by using the same pulse duration in the simulations than in the experiment. The

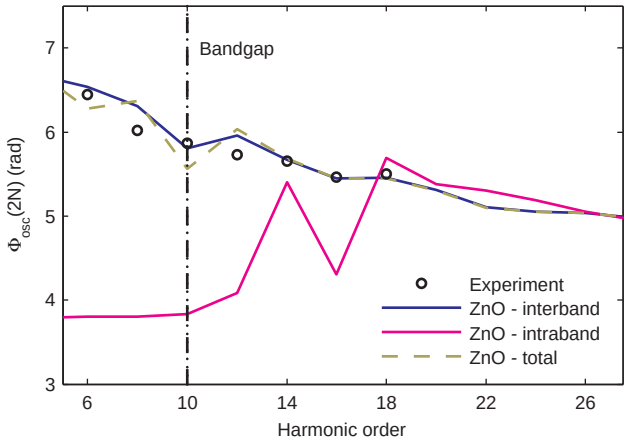

Figure 3.6: $\Phi_{osc}(2N)$ is extracted from the experimental data of Fig. 3.3 (black circles) and compared to the simulated intraband (purple line) and interband (blue line) phase. The simulated phase for their combined emission (interband plus intraband, dashed yellow line) agrees with interband emission, in agreement with interband harmonics being significantly stronger than intraband ones (Fig. 2.1). The vertical dash-dotted black line marks the minimum band gap of ZnO, at 3.3 eV.

spectrograms for the interband and intraband sources are plotted in Fig. 3.5. The theoretical values of Φ_{osc} are extracted from the simulated spectrograms and are plotted in Fig. 3.6 for the intraband (purple line) and interband (blue line) sources, and for their combined emission (gold dashed line). To position the experimental Φ_{osc} (black circles), an unmeasured constant phase is added (this constant phase can be measured by frequency doubling the fundamental in a phase-matched crystal, and beating the newly generated second harmonic field with the one used to perturb the harmonics). We find that *the experiment is consistent with the theoretical prediction that interband harmonics dominate in ZnO for the field strength used (see Fig. 2.1).*

The optimum phase of intraband harmonics above the 18^{th} order follows that of interband harmonics, suggesting that intraband recollisions – a mechanism presented in Chap. 2.3 – dominates intraband emission in this harmonic range. This is further proved in Figure 3.7, that shows the windowed Fourier transform of inter- and intraband currents (color coded) superposed to the time of emission expected from the semiclassical model of recollisions (red lines). The time of emission of intraband harmonics (panel **a**) agrees with recollisions for harmonic orders above the 18^{th}. Below the 18^{th} order, the emission becomes independent on the order, suggesting that other intraband emission mechanisms take over. As a result, Φ_{osc} also becomes independent on the harmonic order in this energy range. To summarize, *varation of Φ_{osc} with harmonic order tags recolliding electron-hole pairs, thereby establishing a link between atomic and solid harmonics.*

Tightening the link. This link can be strengthened further. In Fig. 3.3, the odd harmonics also modulate, but their modulation is much weaker than that of the even harmonics. This is because the added phase σ is small enough that $I_{2N+1} \propto$

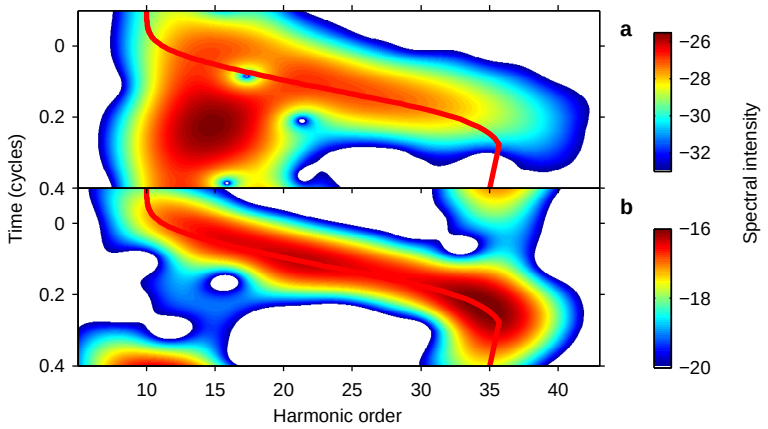

Figure 3.7: Time frequency analysis of the simulated experiment. Intraband emission (**a**) is timed to the recolliding electron-hole pairs (red line) only for harmonic orders above the 18^{th}. Interband harmonics (**b**), instead, arise all from the recollision mechanism. The spectral intensity, colour-coded, is in logarithmic scale.

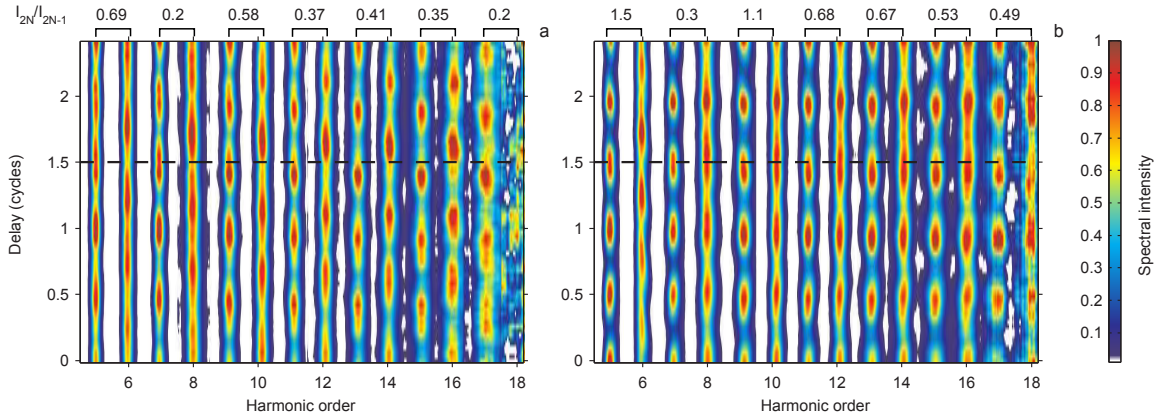

Figure 3.8: Experimental spectrograms for stronger second harmonic fields. (**a**) When the intensity of the second harmonic is increased to 1×10^{-4} times that of the fundamental, the even and odd harmonics modulate out of phase. (**b**) Further increasing the intensity to 3×10^{-3} times that of the fundamental, we find that all harmonics modulate in phase. Each harmonic order is separately normalized. The relative intensity between even-order and adjacent odd-order harmonics is given at the top.

$|\cos(\sigma)|^2 \simeq 1$. When the second harmonic intensity is increased to $\sim 10^{-4}$ of the fundamental (see Fig. 3.8**a**), the odd harmonics strongly modulate out of phase with the even harmonics. The added phase in each arm of the interferometer is now $\sigma \simeq \pi/2$, because for the appropriate delay only even harmonics are generated. This regime is also observed in atomic high harmonic generation.

For even higher second harmonic field strength (Fig. 3.8**b**), the emission is substantially modified. In the highly asymmetric sum field, tunnelling only occurs once per laser cycle. This leads to simultaneous emission (or suppression) of even and odd order harmonics – a behaviour well-studied for atomic gases [34, 36]. In the interferometer picture, the intensity – not only the path length – in each arm of the interferometer is modified. The harmonic structure arises from interference of emission at each laser cycle:

$$\begin{aligned} p(t) &= d(t)e^{in\omega_0 t} + d(t + 2\pi/\omega_0)e^{in\omega_0(t+2\pi/\omega_0)} \\ &= d(t)e^{in\omega_0 t}\left[1 + e^{i2n\pi}\right], \end{aligned}$$

which is always non-zero for $n = \{\text{even}, \text{odd}\}$.

3.2 High harmonics from silicon

High harmonic generation is not limited to ZnO, a wide direct band gap semiconductor. In this section, the generation of high harmonics from Si is demonstrated and characterized.

The experimental setup. In a first experiment, mid-infrared linearly polarized laser pulses of 100 fs duration with a central wavelength of 3.5 μm (0.35 eV photon energy) are focused in a 500 nm thick film of single crystal silicon, at an intensity of 0.10 V/Å in the crystal. Apart from the different laser source, the experimental setup is the same as in Fig. 3.1. The film is epitaxially grown on a 500 μm thick R-plane Sapphire substrate. The beam is incident on the silicon side. The [100] orientation of the Si lattice is parallel to the projection of the c-axis of Sapphire on the surface [39]. Measurement of the birefringence of the substrate determines the orientation of this projection with respect to the laser polarization, which ultimately determines the orientation of the Si lattice with respect to the latter. The field strength in the material is calculated from the vacuum field strength accounting for reflection losses at the air-silicon interface: $F_{si} = 2F_{vac}/(n_{Si} + 1)$. Here, $n_{si} = 3.4286$. The surface normal is aligned to the [001] direction, and is parallel to the laser k-vector.

Rotational dependence. The measured spectrum as a function of the crystallographic orientation with respect to the linear laser polarization is shown in Fig. 3.9. When the sample is rotated about the [001] axis, high harmonic spectra modulate with 4-fold symmetry. All harmonics maximize when the polarization of the fundamental beam is oriented along the [110] direction. For this orientation, electron-hole pairs created by the strong laser field are accelerated along the projection of the

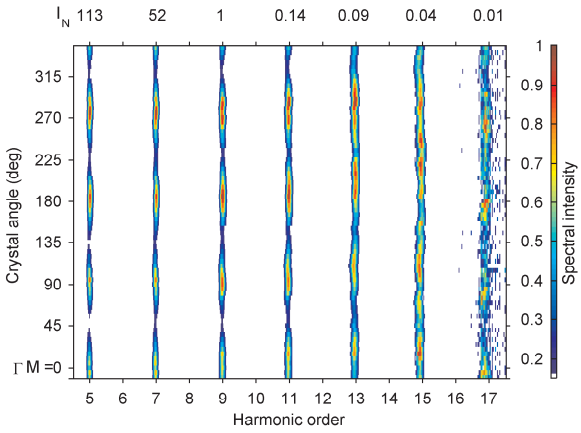

Figure 3.9: High harmonic spectra modulate as the linear polarization is rotated, with maximum emission for polarization parallel to the [110] direction. Each harmonic order is normalized to 1 for clarity. Their original intensity as compared to the 11^{th} order is indicated at the top.

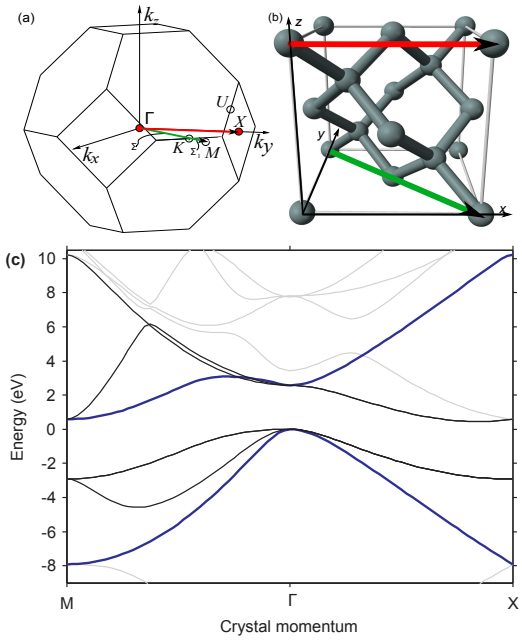

Figure 3.10: **(a)** First Brillouin Zone of the FCC silicon lattice; The M point lies outside the first Brillouin Zone, along the $\Gamma - K$ direction [37, 38]. **(b)** The lattice of silicon. The laser propagates along the z-axis. When the laser is polarized along the [100] direction (red arrow in (b)), electrons are accelerated along the $\Gamma - X$ direction of the Brillouin Zone (red arrow in (a)), and when it is polarized along the [110] (green arrow in (b)) direction they move along the $\Gamma - M$ direction (green arrow in (a)). **(c)** Band structure of silicon obtained from *ab initio* calculations. Bands coloured in blue have been considered for the classical calculation of Fig. 3.12. Bands degenerate with the blue one at Γ are coloured in black.

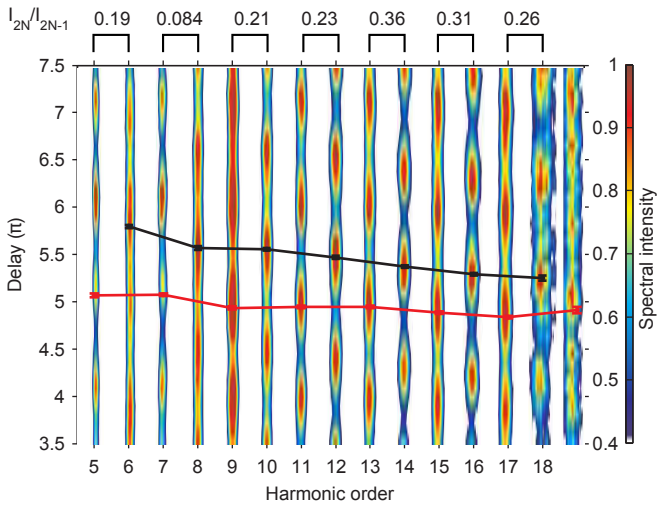

Figure 3.11: The harmonic intensity modulates when the delay between the fundamental and the second harmonic is varied. While the phase of the oscillation for the odd harmonics (red line) is almost constant, the phase of the even harmonics (black line) varies with harmonic order, for polarization along the [110] direction. The relative intensity of even and odd harmonics is shown at the top. Each harmonic order is separately normalized.

Si-Si bonds onto the (001) plane, as indicated by the green arrow in Fig. 3.10(b), or along the $\Gamma - K - M$ direction in the reciprocal space (green arrow in Fig. 3.10**a**). The M point is equivalent to the X point, but it is reached along the Σ_1 line. High harmonics are suppressed for polarization along the [100] direction, when electron-hole pairs move in and out of the molecular chain, as indicated by the red arrow in Fig. 3.10(b). In reciprocal space, the polarization is along the $\Gamma - X$ direction (red arrow in Fig. 3.10**a**).

Because the linear optical properties of silicon are isotropic, neither absorption nor phase-matching explains the strong rotational dependence of the harmonics. The observed behaviour can only originate from the microscopic generation process.

Tagging recollisions. As with ZnO, the possible generating mechanisms are distinguished by adding a weak second harmonic field to the fundamental. When the fundamental and its second harmonic are properly phased, even harmonics are produced, as shown in Fig. 3.11 for a second harmonic intensity of 9×10^{-4} of the fundamental (corresponding to a field strength of only 30 V/μm). In this case, laser pulses of 55 fs duration with a central wavelength of 3.7 μm (0.33 eV photon energy) are focused in a 40 nm thin film of single crystal silicon at the same intensity as in Fig. 3.9. The film is plasma etched from its initial thickness of 500 nm. In this experiment, the beam is incident on the Sapphire side, but to avoid birefringence the polarization is set parallel to the [110] direction.

When the phase between the two colours is varied, the even harmonic intensity modulates. The resulting spectrogram is shown in Fig. 3.11 for polarization along the $\Gamma - M$ direction. The intensity of the even harmonics relative to the odd ones

is reported at the top of the graph. The visibility of the modulation, defined as $V = 2\times(I_{max}-I_{min})/(I_{max}+I_{min})$, steadily increases with harmonic order from 0.04 to 0.8. The phase of the modulation of the even harmonics differs between harmonic orders (the black line connects the maxima of the even harmonics). Like for ZnO, this signature confirms that *recolliding electron-hole pairs and their recombination are the dominant source of harmonics in silicon for excitation with mid-infrared lasers.*

Insights into the tunnelling step. The experiment suggests that either electrons tunnel vertically at the direct band gap, rather than at the minimum (indirect) band gap, or that high harmonics are only generated by direct tunnelled electrons.

Figure 3.12 compares the experimental Φ_{osc} (black dots with error bars) along the [110] direction, with that obtained from a semiclassical calculation (blue line) where electrons tunnel at Γ. The latter curve is obtained, first, by simulating the trajectories of electron-hole pairs over the bands highlighted in blue in Fig. 3.10 and, second, by calculating the additional dipole phase σ (Eq. 3.3). These bands have been chosen because they have the smallest effective mass at Γ, which should result in strongest tunnelling. In reality, one should account for all six bands and their transition dipole moments. For a small perturbation, $I_{2N} \approx \sigma^2$. Following the procedure outlined in Ref. [34], σ can be decomposed as $\sigma(t,\phi) = \sigma_s(t)\cos(\phi) + \sigma_c(t)\sin(\phi)$, and the phase of the modulation of each harmonic calculated as $\Phi_{osc} = \arctan(\sigma_c/\sigma_s)$. The classical calculation does not allow recombination to occur with energy smaller than the minimum (direct) bandgap. Therefore, the calculated Φ_{osc} does not extend below the 10^{th} harmonic order. The analogous limit is present in the semiclassical analysis of gases. Within these limits, the agreement between experiment and analysis is excellent.

In an alternative scenario, electrons pick-up crystal momentum from phonons during tunnelling and start their motion from the minimum energy state away from Γ in the conduction band. Then, electrons and holes accelerate in reciprocal space by the same amount, but remain separated by the initial momentum offset. In real space, electrons and holes are initially at rest because electrons tunnel from the valence band maximum to a local minimum of the conduction band, where $\mathrm{v_{c,v}} = \nabla_{\mathrm{k}} E_{\mathrm{c,v}}(\mathrm{k}) = 0$. Then they begin to accelerate away from each other. Following their re-encounter later in the laser cycle, emission of a high harmonic photon requires recombination with exchange of the same phonons absorbed during tunnelling. This scenario and the one in which tunnelling happens at Γ can be easily discriminated because electrons travel different portions of the Brillouin zone at different times. Therefore, Φ_{osc} is different. The red line of Fig. 3.12 shows Φ_{osc} for electrons that tunnel at M in the conduction band. Because the minimum gap is now close to the indirect band gap of silicon (1.1 eV), the classical calculation extends below the 10^{th} harmonic. The cut-off extends only up to the 14^{th} order, contrary to the experiment. If the probability of emitting or absorbing a phonon is equivalent, our analysis excludes tunnelling across indirect band gaps [13]. The comparison is approximate: in reality electrons should be created at the minimum band gap, positioned along the $\Gamma - X$ direction (100), and accelerated along the

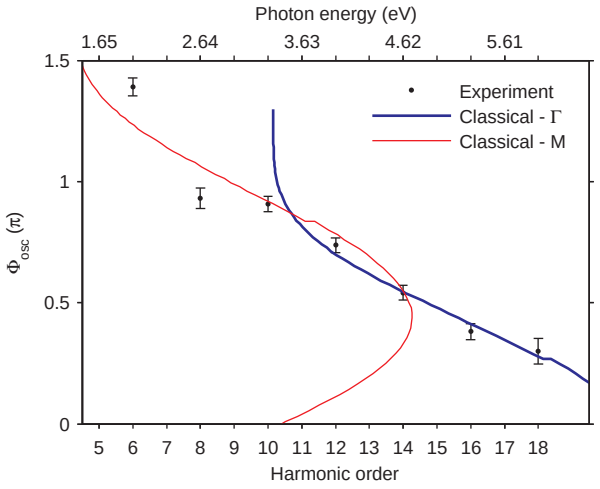

Figure 3.12: Optimum phase for electron-hole pairs tunnelling at Γ (blue line), for polarization along the $\Gamma - M$ direction (as in Fig. 3.11). The minimum harmonic energy corresponds to the direct bandgap of silicon (10^{th} harmonic order). The classical calculation doesn't allow recombination below the minimum bandgap. The red line shows the optimum phase for electrons that tunnell at M, instead. Here, the lowest band gap is close to the minimum (indirect) band gap of silicon (1.1 eV).

(110) direction. Therefore, a 2D model is required. However, the dispersion along this direction, starting at the indirect band gap, should be less than the one crossing Γ, so that Φ_{osc} may be even more different.

The band structure of the material has a strong influence on the high harmonics. This is analysed in the following section.

3.3 Role of the band structure

In the ZnO experiment, even harmonics are detected for second harmonic intensities only 10^{-6} of the fundamental one. This relative intensity is three orders-of-magnitude smaller than in gas phase experiments performed with 800 nm laser pulses. As shown in Fig. 3.13(a), electron–hole pairs in ZnO (black line), at the laser frequency and intensity of the experiment, accumulate four to ten times the phase they accumulate in vacuum (red line) in typical gas phase experiments with $I_0 = 10^{14}$ W/cm^2 and $\lambda = 0.8$ μm. In the *optics* analogy, the arms of the interferometers are longer in solid experiments. Therefore, much weaker fields are required to unbalance the interferometers by the same phase shift.

The longer wavelength used in experiments in solids is only part of the reason why the cumulated phase is higher. The biggest contribution comes from the smaller *effective* mass of electrons and holes in solids as opposed to in vacuum. The effective mass is defined by the curvature of the bands:

$$[m^*]^{-1} = \frac{1}{\hbar^2}\nabla_{\mathrm{k}}^2 E_m(\mathrm{k}), \tag{3.5}$$

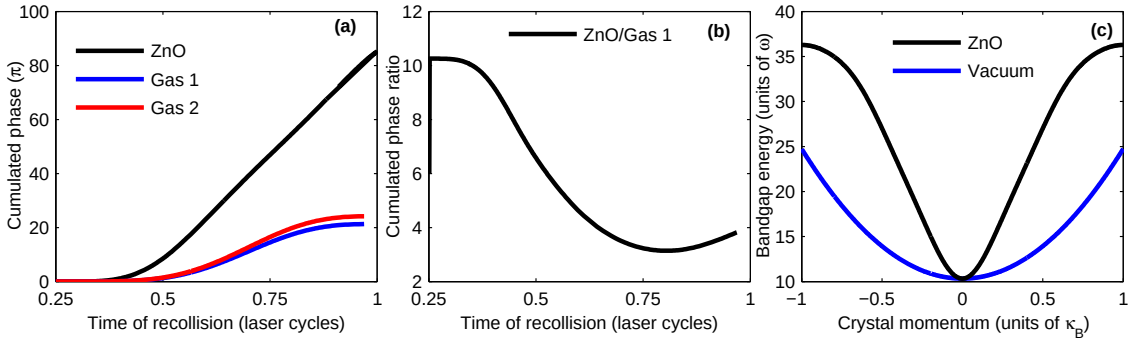

Figure 3.13: (**a**) Dipole phase (in units of π) accumulated by electron-hole pairs between their time of creation and recollision, as a function of the latter, calculated with Eq. (3.1). The laser parameters are $\lambda = 3.76\ \mu m$ and $F_0 = 0.25\ V/\text{Å}$ for ZnO (black line) and for a solid with unitary reduced effective mass (blue line). The dipole phase accumulated in typical experiments in atomic gases with $\lambda = 0.8\ \mu m$ and $I_0 = 10^{14}$ W/cm^2 is plotted with a red line. (**b**) Ratio between the phases accumulated in ZnO and by electron-hole pairs having unitary reduced effective mass (blue line of panel **a**). (**c**) Momentum-dependent band gap of ZnO (black line) and of the model solid with unitary reduced effective mass (blue line).

Because the phase is determined by the band gap ε_g, it is the *reduced effective mass* of the electron-hole pair that comes into play:

$$\frac{1}{m^*_{\text{red}}} = \frac{1}{m^*_c} - \frac{1}{m^*_v} = \frac{1}{\hbar^2}\nabla^2_{\text{k}}\varepsilon_g(\text{k}).$$

The blue line in Fig. 3.13(a) is the phase accumulated by electron-hole pairs having unitary mass ($m^*_{\text{red}} = 1$) in a solid under the conditions of the ZnO experiment. The band gap used is plotted in blue in panel (c), and is compared to the band gap of ZnO (black line). The ratio between the black and blue phases is plotted in panel (b). In ZnO, the reduced effective mass calculated with the band gap of Fig. 3.13(c) is $m^*_{\text{red}} = 0.1\ m_e$. Therefore, it explains why the cumulated phase for the short trajectories, which explore the band gap only around the minimum, is ~ 10 times that in vacuum (for which $m^*_{\text{red}} = m_e$). Longer trajectories explore regions of the reciprocal space for which the quadratic approximation, Eq. (3.5), does not hold. Therefore, the ratio in the cumulated phase between ZnO and vacuum differs from 10.

In conclusion, it is the different band structure of ZnO and vacuum, the integrated quantity in Eq. (3.1), that allows the greater sensitivity of ZnO to perturbing fields at fundamental intensities which are ~ 100 times weaker than in gas phase experiments.

The similar sensitivity to weak fields found in silicon lends itself to integrating high harmonics with solid state technology. It was shown that a clear spectral signature is imposed on a high harmonic beam using a control beam having a peak electric field of only ~ 30 V/μm. Fields of this magnitude are present in electronic circuits. Therefore, it seems possible to record movies of working electrical circuits or of plasmons propagating in plasmonic devices. When the circuit is off, harmonics generated from the spatially complex circuit will diffract according to the shape of

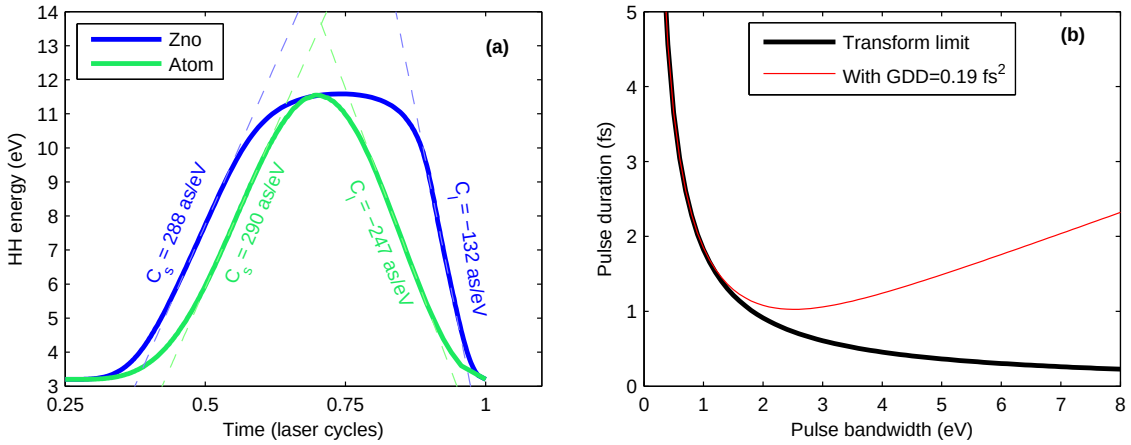

Figure 3.14: **(a)** High harmonic photon energy as a function of the emission time for ZnO at $F_0 = 0.0046$ a.u. (blue solid line) and for an atomic system with the same band gap as ZnO at $F_0 = 0.0087$ a.u. (green solid line). The latter field strength is chosen to equate the cut-off. The atomic ionization potential is set equal to the minimum bandgap E_g. Laser frequency is $\omega_0 = 0.0141$ a.u. The slope of the curves determines the chirp of the high harmonic pulses. The dashed lines are the derivatives taken at 7.5 eV for the long (C_l) and short (C_s) trajectories. The values of the chirps are reported along the lines. **(b)** Variation of the pulse duration as a function of the pulse bandwidth. The short trajectory chirp equivalent to GDD = 0.19 fs^2 broadens the pulse (red line) with respect to its transform limit (black line). For this GDD the shortest pulse (1.02 fs) is obtained for a 2.5 eV bandwidth.

the structures. When the circuit is on, the diffraction is modified by the instantaneous distribution of the internal fields. Comparison of the "off" with the "on" pattern will return a snapshot of the working circuit, or of an evolving plasmon.

3.4 Chirp of high harmonic pulses

One of the most important applications of atomic high harmonic generation is the possibility to synthesize XUV laser pulses with a duration of a fraction of a cycle of the fundamental; that is, several tens of attoseconds. In solids, sub-cycle bursts of harmonic radiation are also created.

How short can such bursts be? Short pulses require wide bandwidths and nearly flat spectral phases (small chirps). The band structure of ZnO allows generation of 20 harmonic orders at the conditions of the experiment, corresponding to 7.6 eV bandwidth. A transform-limited gaussian spectrum with half of this bandwidth corresponds to high harmonic pulses with a duration of 480 as (FWHM). However, analogously to the atomic case, the generation process gives an intrinsic temporal chirp to the harmonics that prevents the generation of transform limited pulses (unless the temporal chirp is compensated ex-situ). The chirp arises from the variation in the emission time of different harmonic orders [40, Chapter 4]:

$$C = \frac{dt}{d(N\omega)}, \tag{3.6}$$

with harmonic order $N(t)$ a function of the return (emission) time.

Fig. 3.14(a) shows the variation of harmonic order with time (solid blue line) obtained from a theoretical calculation performed for laser frequency $\omega_0 = 0.014$ a.u. and $F_0 = 0.0046$ a.u. The first derivative (the chirp) calculated at half of the maximum band gap (at 7.5 eV) for the long and short trajectories is also plotted (dashed blue lines). It amounts to -132 as/eV and +288 as/eV for the long and short trajectories respectively. The latter corresponds to a Group Delay Dispersion (GDD) equal to 0.19 fs^2. The conversion is:

$$GDD\{\text{as}^2\} = \hbar\{\text{eV} \cdot \text{as}\} \times C\{\text{as/eV}\}.$$

In the presence of a linear chirp a transform limited pulse of duration τ_{tl} (FWHM) is broadened to a duration [40, Chapter 1] of,

$$\tau_c = \tau_{tl}\sqrt{1 + \frac{(4ln2)^2 GDD^2}{\tau_{tl}^4}}$$

The shorter the pulse and the wider the spectrum, the more severe it is affected by the chirp. As a result, as long as the chirp cannot be compensated, there exists an optimum bandwidth that generates the shortest pulse. The duration of the high-harmonic pulse as a function of its bandwidth is shown in Fig. 3.14(b). The shortest possible pulse with the given chirp is achieved for 2.5 eV bandwidth and lasts 1.02 fs (transform limit is 0.73 fs).

So far, the estimate on the achievable pulse duration has not taken into account how the harmonic intensity changes with harmonic order, a factor that determines the actual bandwidth achievable in experiments. In fact, a fast drop of harmonic intensity with order has been measured from ZnO [16]. This suggests that multi-eV bandwidths are hard to achieve in ZnO, however a $\sim$ 2.5 eV FWHM seems possible. It corresponds to the optimum bandwidth in Fig. 3.14(b). Therefore, by optimizing material parameters and by going to wider band gap materials, sub-fs high-harmonic pulses from solids will be achieved. Wider bandwidths can also be obtained by excitation to higher lying conduction bands [41, 42] or lower lying valence bands.

The high harmonic pulses propagate inside the generating crystal, so that linear material dispersion changes the pulses that reach the exit surface. In practice, only above band gap harmonics that are generated within one absorption length of the material are measured [43]. Because absorption lengths are on the order of few tens of nanometers, it is unlikely that linear dispersion plays any role.

In the experiment, a harmonic chirp of 380 as/eV at the 16^{th} harmonic order is measured from Fig. 3.6. It corresponds to a train of pulses with duration of 1.7 fs (before dispersion compensation) for a $\sim$ 2 eV bandwidth.

Comparison with gases. Chirps obtained from solids at the conditions of the experiment are larger than those obtained in gases, which typically are $\sim$10 as/eV. Small chirp in gases is attributed to the two orders of magnitude higher intensity

typically used in experiments, which in turn results in wider bandwidth of the harmonic spectrum and smaller shifts of emission time per harmonic order.

Besides the laser parameters, the band structure also affects the chirp. Figure 3.14(a) compares the chirp from ZnO and from atomic gases for field strengths that yield the same cut-off harmonic (at the same fundamental frequency). The atomic emission times and chirps are the green solid and dashed curves respectively. Whereas the atomic chirp of the short trajectory is 290 as/eV (comparable to the one from ZnO), the chirp of the long trajectory is -247 as/eV, almost twice the one from ZnO.

Chapter 4

Applications and implications of the recollision mechanism

The dominance of recollision-based harmonics demonstrated in the previous chapter promises to extend to solids the attosecond and high-harmonic based methodology applied to study atomic and molecular gases. However, novel methods can also be developed specifically for solids. The first section of this chapter presents a method to reconstruct the momentum-dependent band gap of a solid using high harmonics. Then, an analytical scaling law for the cut-off is derived in the second section. From the scaling of the cut-off with field strength, other information about the solid can be gathered. In the last section, instead, a method to extend the cut-off to higher energies is presented. It is based on a novel emission mechanisn, interband in nature, but not related to recollisions.

The contents of this chapter are based entirely on my research [44, 20, 45].

4.1 A method to reconstruct band structures

The variation of Φ_{osc} with harmonic order differs considerably between ZnO and Si, and even between different orientations in Si. For given laser parameters, Φ_{osc} is determined by the structure of the bands in which the electrons and holes move. Is it possible to extract this information?

The band structure of matter determines its properties. It is typically mapped with Angle-Resolved PhotoEmission Spectroscopy (ARPES) [46], where the energy and the momentum of electrons liberated from the material upon absorption of energetic photons are indipendently measured. The process is depicted in the left side of Fig. 4.1. ARPES has been incredibly useful to understand novel systems, such as high-temperature superconductors [47] and other strongly correlated materials like graphene [48] and topological insulators [49]. Conversely, in "inverse photoemission", electrons can be externally injected into higher-lying unoccupied bands and the photons emitted upon their decay to lower-lying states are measured.

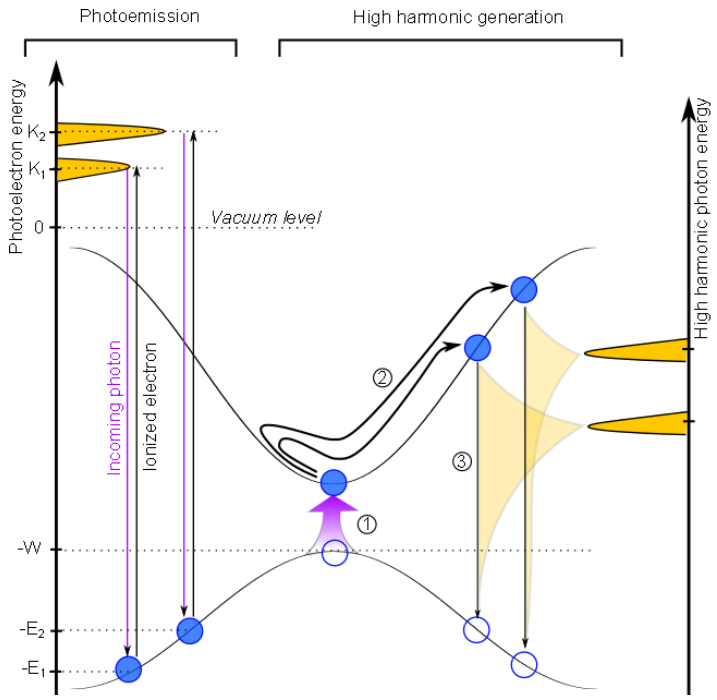

Figure 4.1: Comparison between photoemission and high harmonic generation. In photoemission experiments, an incoming photon (purple arrow) causes emission of an electron (black vertical arrow) with kinetic energy (K1 and K2) proportional to the initial binding energy (E1 and E2). In high harmonic generation, an electron first tunnels (marked by circled "1") to the conduction band. The electron-hole pair is then accelerated (circled "2") and recombines (circled "3") emitting a harmonic photon in the process. Electrons and holes are denoted by filled and empty blue circles respectively. Two trajectories are identified by the wiggled solid black arrows, corresponding to different times of creation and recollision of the electron-hole pair.

However, photoelectrons are not always accessible. For example, they cannot be emitted from the bulk (ARPES is a surface-sensitive technique), they cannot escape enclosures, they are affected by magnetic fields, and they don't propagate at atmospheric pressures. Therefore, matter under extreme conditions of pressure or magnetic fields, and chemical reactions on surfaces at ambient conditions are all precluded to photoemission experiments. Measurement of the band structure in these situations can be done all-optically with the high harmonics.

High harmonic generation can be considered, in fact, a coherent analogue of inverse photoemission: rather than externally injecting electrons, conventional of the latter method, electron-hole pairs are internally created and accelerated by the laser field, which positions them at the crystal momentum of recollision, where electrons recombine with the holes emitting high harmonic photons. The process is sketched to the right of Fig. 4.1. Knowledge of the trajectories of the pairs, for examples indirectly obtained through Φ_{osc}, links photon energy to the momentum of recollision, in a similar fashion that photoelectron energy is linked to its momentum in ARPES.

Proof of principle demonstration. To prove the concept, a simulation of a possible experiment was performed for a model hexagonal crystal interacting with a fundamental mid-infrared laser pulse and its second harmonic (at an intensity of 10^{-5} of the fundamental). The fundamental field has a peak strength of 0.28 $V/$Å and a central wavelength of 3.66 μm; both fields are linearly polarized along the $\Gamma - M$ direction of the Brillouin zone. The simulated spectrogram is shown in Fig. 4.2(a). The phase of the modulation of the even harmonics is plotted as red dots with error bars. A realistic experimental uncertainty on Φ_{osc} is ~ 25 mrad, and is artificially added to simulate noise in an experiment. The band gap between the valence and conduction bands is plotted in Fig. 4.2(c), red line, up to the edge of the Brillouin zone. Its analytical form is reported in the caption. This is the "target" band structure for a reconstruction procedure.

To reconstruct the target band gap, Φ_{osc} of the simulated experiment is compared with those calculated for a set of trial band gaps and the ones that best reproduce the target are selected[1]. A successful reconstruction requires a precise calibration of the experimental laser field strength. The trial bands are chosen to have the same functional form as the target: $\varepsilon_g(\mathrm{k}) = E_g + A[1 - \cos(\mathrm{k}a)] + B[1 - \cos(2\mathrm{k}a)]$. The spectrograms are calculated by spanning the (A,B) parameter space; the target band is not included in the set. A set of 257 trial bands is considered. The comparison is performed according to χ^2:

$$\chi_i^2 = \sum_{2N} \left[\frac{\Phi_{osc}(2N) - \Phi_{osc}^t(2N, i)}{\sigma} \right]^2 , \tag{4.1}$$

[1]In principle, given a trial band gap, Φ_{osc} can also be calculated analytically knowing the link between birth and recollision times, and the associated photon energy. In practice, both real and imaginary components of the solutions to the saddle point equations are important to determine Φ_{osc}, and their determination for arbitrarily shaped bands is non-trivial. To the best of my knowledge, no general solution exists to date.

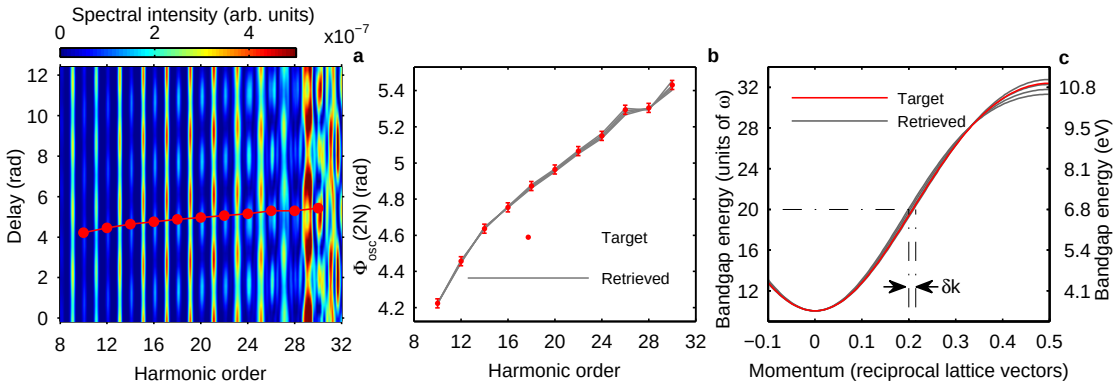

Figure 4.2: Reconstruction of the bands. **(a)** High harmonic spectra obtained from the target band structure as a function of delay between fundamental and second harmonic fields. The red line with dots is the optimum phase Φ_{osc}. **(b)** Target Φ_{osc} (red dots with error bars) compared to those associated with the retrieved band structures (grey lines). **(c)** Target (red line) and retrieved (grey lines) momentum-dependent band gaps. The Brillouin zone extends up to half of the reciprocal lattice vector. The target band gap is $\varepsilon_g(\mathrm{k}) = E_g + 0.139[1 - \cos(\mathrm{k}a)] + 0.011[1 - \cos(2\mathrm{k}a)]$, and approximates that of a ZnO crystal as obtained from *ab initio* calculations. The crystal and laser parameters are defined in Table B.2 of Appendix B.

where the sum runs over the even harmonics, "i" labels one trial band and σ is the uncertainty on Φ_{osc}. The χ^2 probability distribution function is used to reject candidate band structures that badly fit the experimental phase: a trial is rejected if the probability of measuring $\chi^2 > \chi_i^2$ is lower than the threshold p = 0.1. With a confidence level (1-p) of 90%, only four trial bands are plausible – their shape and the associated Φ_{osc} are plotted as grey lines in Figs. 4.2(b-c).

The retrieved band gaps are extremely accurate: at most they differ by 0.2 eV at M, a resolution comparable to time-resolved ARPES (static experiments have higher resolution) [50]. The momentum resolution (δk in Fig. 4.2**c**) can be interpreted as the difference between the maximum and minimum momentum corresponding to a given energy for the set of reconstructed bands. It amounts to $\sim$ 1-5% of the Brillouin Zone, or to $\sim$ 0.02-0.12 Å^{-1}. The accuracy is limited by the precision on Φ_{osc} and the number of measured harmonic orders (their effect on the reconstruction is analysed in Appendix B), not by the spectral bandwidth of the laser pulse, a typical shortcoming of photoemission. In fact, shorter pulses (wider bandwidths) might even be beneficial to solid high harmonics because they can extend the harmonic cutoff (wider harmonic range), similarly to the atomic case.

One may argue that the identical functional form of the target and the trials is biased towards good agreement. In Appendix B it is demonstrated that the reconstruction is successful also for target and trial bandgaps with different functional forms.

Preliminary experiment in ZnO. To experimentally verify the simulation, a more accurate two-colour experiment has been performed in ZnO. In the simulated reconstruction presented so far, one needs radiation stretching up to the maximum

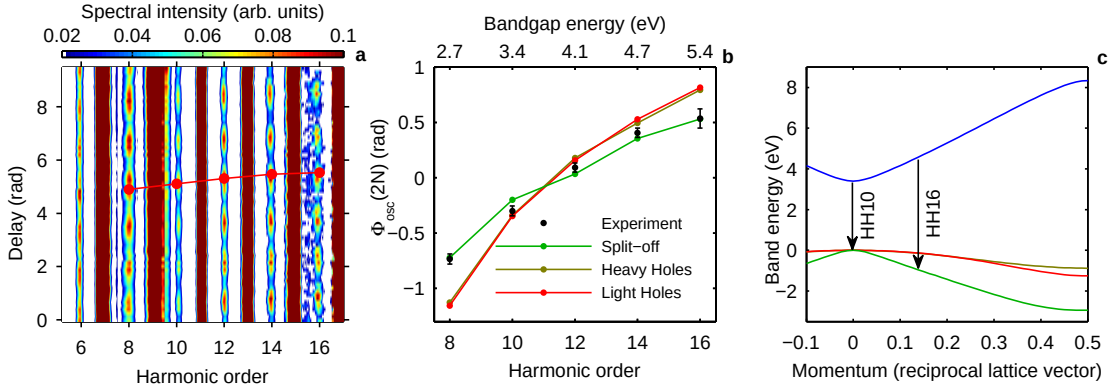

Figure 4.3: Experimental contribution of the split-off band. **(a)** Experimental spectrogram obtained from a ZnO crystal. Experimental parameters are the same as in Fig. 4.2. Each harmonic order is independently normalized to facilitate comparison between orders. The odd harmonics saturate the spectrometer. The red line is the experimental Φ_{osc}. **(b)** The optimum phase extracted from the experiment (black dots with error bars), simulated for tunnelling from the split-off valence band (green line), the heavy-holes band (gold line) and the light holes band (red line). Contrary to Fig. 4.2, an unmeasured offset phase is used here to position the experimental data. This phase is in principle measurable in a more refined experiment. **(c)** Band structure for the same bands of part (b) with the same color coding. The blue band is the first conduction band. They are obtained from *ab initio* calculations. The arrows mark the recombination between electrons and holes in the split-off band for the 10^{th} and 16^{th} harmonic orders. The measured harmonic spectrum extends up to $\sim 25\%$ of the Brillouin Zone.

band energy to obtain the full relative band structure. In ZnO this requires a spectrum that terminates at ~ 10 eV. However, the spectrograph used in the experiment does not allow measurement beyond ~ 6 eV, or the 18^{th} harmonic. Therefore, electrons and holes that explore only $\sim 20\%$ of the Brillouin Zone are measured.

With the limited experimental data presented in Fig. 4.3(a), it is impossible to reconstruct the full bands. However, by comparing the experiment with Φ_{osc} obtained from *ab initio* calculated bands, one can identify which of the possible valence bands contribute to tunnelling.

The experimental Φ_{osc} (black dots in Fig. 4.3**b**) agrees with the simulation for tunnelling from the split-off valence band to the first conduction band (green line); the other two curves associated to tunnelling from the heavy holes (gold) and light holes (red) bands are significantly steeper. In atoms, when multiple occupied states contribute to high harmonic generation, a hole wavepacket is launched and evolves on attosecond timescales. Because only one valence band seems active in ZnO, similar dynamics do not seem to be initiated.

The different slope of Φ_{osc} for the different valence bands is, to first order, related to the effective mass: in narrow bands, adjacent harmonic orders map onto very different momenta, and in turn to very different trajectories. Since the optimum phase is linked to the trajectory, Φ_{osc} varies more strongly with harmonic order than in wider bands. The accuracy on Φ_{osc} is 50 mrad and is mainly limited by intensity fluctuations on the high harmonic signal and delay jitter. The bands are plotted in Fig. 4.3(c), with the same color coding (blue for the conduction band).

The dominant contribution of the split-off valence band to tunnelling is expected: holes in this band have a lower effective mass than the heavy and light holes valence bands. Is it possible to reconstruct the heavier bands instead? It may be possible if the selected band is non degenerate with the split-off band (the separation is $\sim$ 0.1 eV at Γ). For example, the infrared field could resonantly populate an intragap impurity level that lays one or two photon energies above the top of the desired valence band. From there, electrons will tunnel to the conduction band. The presence of the resonance greatly enhances tunnelling over the off-resonant transitions from the split-off band. If the desired band is well separated ($>$ 1 eV), one could also excite with a resonant ultraviolet pulse within a fraction of the infrared cycle [51].

Three important issues are raised.

1. Electrons and holes move in bands dressed with the laser field. Does any laser field that is sufficiently intense to create the harmonics severely distort the bands that are measured?

   The analytical solution of the Semiconductor Bloch equations in the limit of negligible depletion of the valence band (Eqs. 2.12) shows electron-hole pairs moving in the field-free band structure. As found for atomic high harmonic generation [52], depletion automatically includes Stark shift of the energy states. When depletion is included in solids (see appendix C), the semiclassical action becomes:

   $$S(\mathbf{k}, t', t) = \int_{t'}^{t} \sqrt{\varepsilon_g^2[\mathbf{k} - \mathbf{A}(t) - \mathbf{A}(t'')] + (Fd)^2} dt'', \tag{4.2}$$

   where d is the transition dipole moment between the bands. Here, the electron propagates in the Stark shifted band structure. The effect is maximum at the minimum band gap, $\varepsilon_g(\mathbf{k}) = E_g$, and when the field is strongest. For the parameters of the experiment, $E_g = 3.2$ eV and $F = 0.28\,V/\text{Å}$ and $d = 1.8$ Å, the dressed band gap differs from the field-free one by only 2%. Furthermore, the simulations naturally include the effect of the field so that any distortion to Φ_{osc} is already accounted for in the reconstruction.

2. Real materials have multiple bands. Does the presence of multiple bands alter the optimum phase originating from a two-band recombination? In this regard, recent calculations are encouraging [42, 45]. Model results show that when several bands are considered, two-band emission still dominates over a reasonably extended intensity range. This is possibly a result of the wide separation between bands. Coupling between multiple bands is expected to be negligible also for closely spaced bands of similar symmetry. When transition dipole moments become large, however, coupling of multiple bands can be significant [31].

3. Dynamical screening of the Coulomb interaction following strong-field excitation can lead to renormalization of the bandgap [13], and consequently to an

offset of the absolute phase. In Appendix B it is shown that for variations < 0.2 eV, the offset is almost identical for all harmonic orders, and the reconstruction converges to the field-free band structure if the absolute phase is neglected. Conversely, the absolute phase can be used to map the dynamical screening.

In summary, an all-optical method complementary to ARPES for measuring band structures based on high harmonic generation has been demonstrated. Specifically, it exploits the sensitivity of the phase of the oscillation of even harmonics to the momentum-dependent band gap. This technique will be useful where it is not possible to detect photoelectrons, such as in the bulk of materials or in matter under extreme pressures [53] or high magnetic fields. In addition, it may be possible to extend the approach to studying the energetics of chemical reactions under ambient conditions (it does not require vacuum up to energies of ~ 16 eV, where Ar purging is sufficient), such as catalysis, oxidation of metals, and solution chemistry.

Due to the brief life of recolliding electron-hole pairs, all-optical band structure measurement inherently has ultrafast temporal resolution, at no expense of energy resolution. It will be possible to probe the fastest modifications to band structures, for example band renormalization as population is transferred between the bands [13], the onset of screening [54] or of the effective mass [55]. The initial states of photoinduced transitions in strongly correlated materials can potentially be mapped, too [56].

In addition, as in photoelectron spectroscopy, it seems possible to obtain information about individual bands by forcing the electron or the hole to propagate in a known band. For example a localized intragap impurity state for the hole or a free-electron band for an electron propagating in vacuum. The latter can be achieved by grazing incidence illumination with laser polarization orthogonal to the surface.

Finally, another method that retrieves some features of the band structure has been proposed in the literature [18]. The necessary information is encoded in the relative intensities of the odd harmonics generated by the "velocity" mechanism described in section 2.3. The method presented here exploits the recolliding trajectories, and is therefore completely different.

4.2 An analytical cut-off scaling law

When high harmonics from bulk crystals were first observed, a linear scaling of the cut-off harmonic order with the laser field strength was measured [16]. This behaviour is in stark contrast with the quadratic dependence on field strength typical of gas-phase experiments, as explained in chapter 1, immediately suggesting that high harmonics from solids arise from a very different mechanism than in gases. In fact, theoretical investigation of intraband emission via nonlinear oscillations of electrons' velocity confirmed the linear scaling, although no quantitative comparison between theory and experiment has been performed [57, 42]. Furthermore, no analytical solution has been derived. Interband emission, however, also reveals a linear scaling, as shown in Fig. 4.4 (red line). By using the analytical solution of

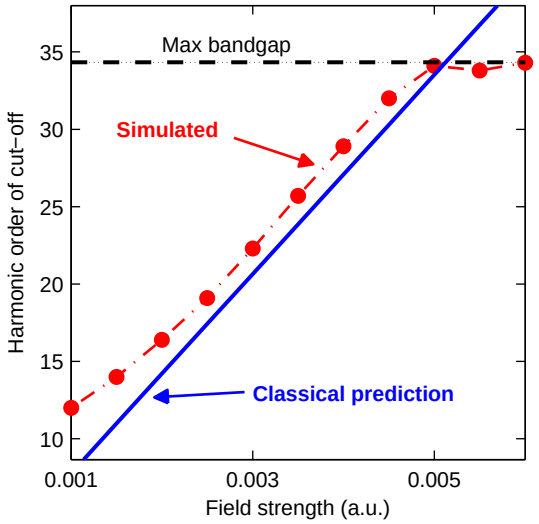

Figure 4.4: The simulated high harmonic cut-off (red circles, red dash-dotted line) lies slightly above the cut-off predicted with classical trajectory analysis (Eq. 4.5). The band parameters are given in the caption of Table 4.1. The laser polarization is aligned along the Γ-M direction of the hexagonal Brillouin zone of ZnO, the central frequency is $\omega_0 = 0.014$ a.u.

interband emission, Eq. (2.12b), and the saddle point conditions, an approximate analytical law is derived below.

Conservation of energy, Eq. (2.14c), requires that the cut-off harmonic ω_c is determined by electron-hole pairs recolliding with the highest momentum $\mathbf{k}_c$, that is,

$$\omega_c = \varepsilon_{\mathrm{g}}(\mathbf{k}_c).$$

In a solid, the band energy can be a complicated function of momentum. Fortunately, in most cases, $\varepsilon_g(\mathbf{k})$ is almost linear near the half-point of the Brillouin zone – between Γ and $\kappa/2 = \pi/a$ – as the curvature changes sign between the bottom and the top of the bands. Furthermore, only the direction along the laser polarization matters to calculate the cut-off, so the vectorial nature of $\mathbf{k}$ can be disregarded. By expanding $\varepsilon_g(\mathrm{k})$ up to first order around $\mathrm{k} = \kappa/4$ we obtain

$$\omega_c \simeq \varepsilon_g\left(\frac{\kappa}{4}\right) + \left.\frac{d\varepsilon_g(\mathrm{k}_c)}{d\mathrm{k}_c}\right|_{\mathrm{k}_c=\kappa/4} \left(\mathrm{k}_c - \frac{\kappa}{4}\right). \tag{4.3}$$

The momentum at recollision is determined by a trajectory born at time t_c' and recolliding at time t_c,

$$\mathrm{k}_c = \frac{F_0}{\omega_0}\left[\sin(\omega_0 t_c') - \sin(\omega_0 t_c)\right] = \frac{F_0\delta}{\omega}. \tag{4.4}$$

This trajectory can be found with the numerical procedure described in chapter 1. In the following, the case of nearest neighbours bands is discussed, where

$$\varepsilon_g(\mathrm{k}) = E_g + (\Delta_{\mathrm{v}} + \Delta_{\mathrm{c}})[1 - \cos(\mathrm{k}a)],$$

where $2\Delta_c$ and $2\Delta_v$ are the widths of the conduction and valence bands, respectively. Inserting $\varepsilon_g(k)$ in Eq. (4.3) yields the cut-off law

$$\omega_c = E_g + (\Delta_c + \Delta_v)\left(1 - \frac{\pi}{2} + \frac{F_0 a \delta}{\omega_0}\right). \tag{4.5}$$

The blue line in Fig. 4.4 represents the cut-off calculated with the above formula for a nearest neighbours band structure that best approximates the real ZnO bands used for Fig. 2.1. The band parameters are reported in the caption of Table 4.1. Table 4.1 reports the birth and recollision times for the cut-off trajectory along with δ, defined in Eq. (4.4), for increasing field strengths. As Eq. (4.5) is based on an expansion around the crystal momentum at half Brillouin zone, δ can be taken from the trajectory that recollides at $\omega_c = \varepsilon_g[\kappa/4]$. This yields $\delta \simeq 1.32$.

F_0	t'/T_0	t/T_0	δ	two-band cut-off
0.001	0.050	0.701	1.26	10.1
0.002	0.052	0.702	1.27	14.3
0.003	0.057	0.700	1.30	20.4
0.004	0.063	0.708	1.35	27.5
0.005	0.077	0.728	1.45	33.4
0.006	0.107	0.630	1.35	34.3

Table 4.1: Parameters describing the cut-off trajectory as a function of field strength for a nearest neighbour band structure with coefficients: $\Delta_c = 0.0872$ a.u., $\Delta_v = 0.0925$ a.u., a = 10.64 a.u., $E_g = 0.1213$ a.u. Birth (t') and recollision (t) times are given in units of optical cycles (T_0). The trajectory responsible for the cut-off emission changes slightly as a function of the laser field strength.

The validity of Eq. (4.5) is tested against a simulation of the high-harmonic spectrum for the same band structure. The cut-off is extracted from a windowed Fourier transform of the interband current. Because the windowed Fourier transform returns a continuous spectrum, the cut-off is determined more accurately than by inferring it from the discrete harmonic structure. The cut-off corresponds to the maximum photon energy in the plateau region of the spectrum, before the exponential roll-off of the high harmonic intensity (see Fig. 2.1). This photon energy is plotted in Fig. 4.4 (red line). The numerical result lies about 1 to 2 harmonic orders above the theoretical prediction (blue line), but their slope is identical.

The small difference between numerical and analytical cut-off is probably due to the neglect of the imaginary parts of the saddle points. Taking into account the complex nature of the saddle points, electrons and holes are not born at the same position $\Delta x(t') = x_c(t') - x_v(t') \neq 0$. For recollision to occur, the electron and the hole have to travel the extra distance $\Delta x(t')$. The work done by the field gives the pair extra energy $\delta\omega = F(t)\Delta x(t')$. A classical description fails to account for this fact and returns a lower cut-off.

Three comments can be made:

1. The derived cut-off law is accurate as long as the band gap is approximately a linear function of momentum. Deviations from the cut-off law are expected around the minimum and maximum energies, where quadratic terms dominate the dispersion. Indeed, deviations from the linear scaling are evident in Fig. 4.4 near the lowest and the highest photon energies. Most notably, Eq. (4.5) fails in the limit $F_0 \to 0$ since it predicts a cut-off lower than the minimum band gap. In the quasi-classical analysis the energy available to the electron-hole pair for recombination must always be higher or equal to E_g.

2. The coefficient δ in table 4.1 is approximately independent of electric field strength, up to the field strength for which the cut-off approaches the maximum band gap (see table 4.1). However, the birth and recollision times shift for increasing fields, a behaviour that has not been observed for atomic high harmonic generation. The variation of the trajectory with field strength arises from the cut-off electrons (and holes) exploring the non-parabolic part of the band structure, an effect described in chapter 1.

3. Finally, the quadratic scaling of cut-off with field strength in atomic high harmonic generation can be viewed as a special case in which the band gap energy, determined by the energy of electrons in vacuum, is a quadratic function of momentum. In solids, the interpretation of the cut-off and the analytical scaling law presented in this section opens the possibility of mapping the momentum-dependent band gap by accurately measuring the cut-off harmonic as a function of the laser intensity.

4.3 A mechanism to reach higher cut-off

Experiments with mid-infrared lasers have been confined to moderate intensities by the onset of material damage. However, the material damage threshold can be shifted to higher intensities by using shorter pulse durations and/or by going to different materials. This makes the study of the higher intensity regime meaningful and interesting from an application perspective. Higher laser intensities can potentially translate into shorter harmonic wavelengths and shorter high harmonic pulse durations, both being of interest for attosecond spectroscopy in solids.

At higher intensities, when electrons are driven beyond the first Brillouin zone boundary, intraband harmonics arising from the band velocities can extend beyond the maximum band gap, as opposed to interband harmonics arising from recollisions. Obviously, electrons can also tunnel to higher-lying conduction bands [42, 41], in which case the interband cut-off can be extended. In this scenario, the harmonic intensity above the 2-band cut-off strongly depends on the energy gap between the two conduction bands at the edge of the Brillouin zone. There is, however, an additional interband mechanism to extend the cut-off, that does not require excitation to higher-lying conduction bands. This mechanism is demonstrated below.

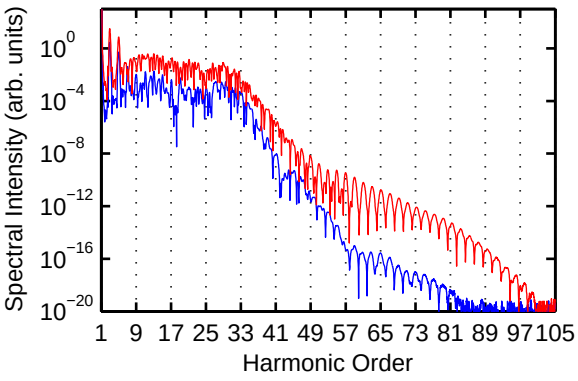

Figure 4.5: Harmonic spectra for $F_0 = 0.007$ a.u. (blue) and $F_0 = 0.01$ a.u. (red) for $\lambda = 3.25$ μm, and for a dephasing time of $T_2 = 5.4$ fs (equal to half cycle).

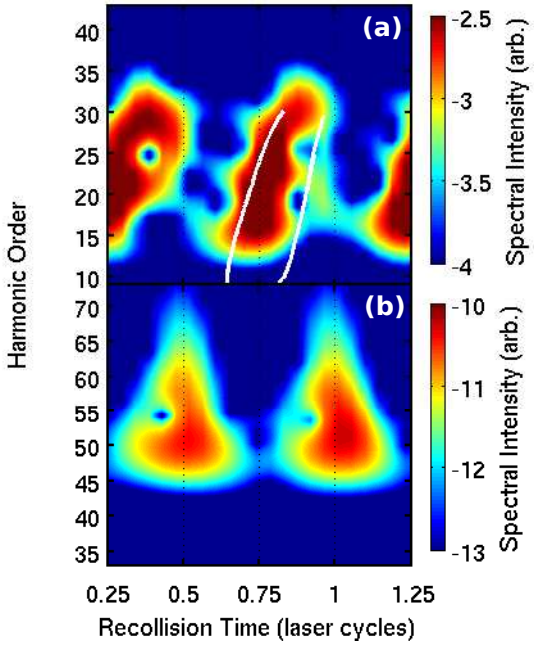

Figure 4.6: Time-frequency analysis for the **(a)** fundamental and **(b)** second cut-off for field intensity $F_0 = 0.01$ a.u. of Fig. 4.5. The field peaks at quarter-cycle times and the nodes occur at integer and half-integer cycle times. The white lines are the results for the first returns from the semiclassical trajectory analysis. The color scale is logarithmic.

Evidence for a higher cut-off. Figure 4.5 shows the harmonic spectra for field strengths $F_0 = 0.007$ a.u. (blue) and $F_0 = 0.01$ a.u. (red) in a ZnO crystal (the bands and crystal parameters are the same as in Fig. 2.1). These field strengths correspond to vacuum field intensities of $I_{\text{vac}} = 3.6$ TW/cm^2 ($F_{\text{vac}} = 0.51$ V/Å) and $I_{\text{vac}} = 7.4$ TW/cm^2 ($F_{\text{vac}} = 0.73$ V/Å), respectively. In contrast, the highest vacuum intensity used for experimental measurement in Ref. [16] was 5 TW/cm^2 (0.6 V/Å). The two-band cut-off from recolliding electron-hole pairs sets about the 33^{rd} harmonic order. At both field strengths electrons will travel beyond the first Brillouin zone and, as a result, a second plateau emerges about the 45^{th} order, followed by another exponential drop; for higher field strengths the second plateau is more pronounced. This "staircase" structure is not observed when the field is too weak for electrons to travel beyond the first Brillouin zone. Finally, the staircase structure appears also in the intraband current, however, is considerably weaker, and therefore not shown here.

Figure 4.6 shows the spectrograms of the interband current for $F_0 = 0.01$ a.u. when a spectral filter positioned near the first (figure 4.6**a**) or the second (4.6**b**) cut-off is applied. The highest photon energy of the first plateau is emitted slightly before each field zero (at 0.5 and 1 laser cycles), in agreement with the semiclassical recollision model (white lines). The two white lines indicate trajectories that are born after and before the peak of the field. As illustrated in Fig. 2.2(h), it is the latter that dominates the emission at such high intensities. Notably, these trajectories propagate outside the first Brillouin zone.

All harmonics of the second plateau, instead, are emitted in phase near a field zero (panel b). The observed difference is indicative of an interband process for emitting harmonic radiation that occurs when electrons traverse beyond the first Brillouin zone that is fundamentally different from the classical trajectory picture.

Explanation of the emission mechanism. The physical picture of this emission mechanism can be grasped with a saddle point analysis of the interband current, Eq. (2.12b). Saddle point integration in k and t' yields (in one dimension):

$$\mathrm{j}_{\text{er}}(\omega) = \sum_{t_b} Q(t_b) \int_{-\infty}^{\infty} dt\; e^{i\omega t} e^{-iS(t_b,t)} + c.c. \tag{4.6}$$

where t_b is the birth time (the solution of the saddle point in t'), Q is a pre-exponential factor, $S(t_b,t) = \int_{t_b}^{t} \varepsilon_g[A(t'') - A(t_b)]dt''$. The saddle point condition $\mathrm{k} = A(t) - A(t_b)$ has been used. For the purpose of the analysis, $T_2 = \infty$. To simplify the expressions, the nearest neighbour band structure is used: $\varepsilon_g = E_g + \Delta\{1 - \cos[a(A(t'') - A(t_b)]\}$ where a is the lattice constant. Looking at a single birth time and ignoring the pre-expontential factor, the current can be written as:

$$\tilde{\mathrm{j}}_{t_b}(\omega) \propto \int_{-\infty}^{\infty} e^{i\omega t} e^{-i(E_g+\Delta)(t-t_b)} e^{i\Delta I_g(t_b,t)} dt, \tag{4.7}$$

where $I_g(t_b,t) = \int_{t_b}^{t} \cos[a(A(t'') - A(t_b))]dt''$.

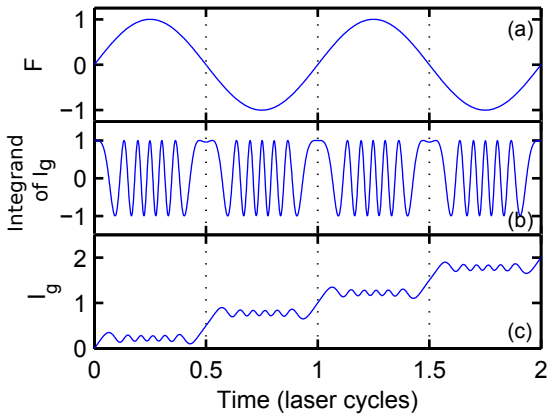

Figure 4.7: **(a)** Laser field normalized by peak amplitude. **(b)** Integrand of I_g; that is $\Delta^{-1}(\varepsilon_g - E_g)$. The saddle points occur at the field nodes. **(c)** Full integral I_g. The steps result from the contributions from the individual saddle points. Here $F_0 = 0.04$ a.u. The field strength is made artificially strong for illustrative purposes.

In Fig. 4.7 the laser field F, ε_g, and I_g are plotted as a function of time. Note that ε_g is a rapidly oscillating function so that the integral I_g in the exponent has to be calculated with the saddle point method. This is fundamentally different from the usual use of saddle point integration for high harmonic generation, which is applied to the integral over the exponent, $\int dt' \exp[iS(t', t)]$. Defining the phase term in $I_g(t_b, t)$ as $\phi(t_b, t) = a[A(t'') - A(t_b)]$, at the saddle point t_s one gets the condition:

$$\frac{d\phi}{dt''} = -aF(t_s) = 0. \tag{4.8}$$

This implies that the saddle points occur at the nodes of the field (when the vector potential is maximum): $t_s = n\pi/\omega_0$, where $n \in \mathbb{Z}$, as can be seen in Fig. 4.7(b). Thus, at the saddle point t_s, $\phi(t_b, t_s) = a[A(t_s) - A(t_b)]$ and $\phi''(t_b, t_s) = -a\dot{F}(t_s)$. The integral can be approximated around each saddle point as:

$$I_g^{(s)} \approx \int_{t_b - t_s}^{t - t_s} \cos\left[\phi(t_b, t_s) + \frac{1}{2}\phi''(t_b, t_s)\tau^2\right] d\tau.$$

It can be demonstrated [45] that the integral has a dominant contribution that is linear in time, also apparent in Fig. 4.7(c):

$$I_g^{(s)} \approx \cos[\phi(t_b, t_s)](t - t_b). \tag{4.9}$$

By adding the contribution of each saddle point t_s, the Fourier integral of the inter-band current becomes:

$$\tilde{\mathrm{j}}_{t_b}(\omega) \approx \int_{-\infty}^{\infty} e^{-i(E_g + \Delta - \omega)(t - t_b)} e^{i\Delta \sum_n I_g^{(s)}} dt.$$

Inserting Eq. (4.9) into the above expression and integrating over t results in a delta function yielding the relation,

$$\omega = E_g + \Delta\{1 - \sum_n \cos[\phi(t_b, t_s)]\}.$$

Maximum ionization occurs at field peaks for which $A(t_b) = 0$. Then, adding N saddle points, the above equation becomes:

$$\omega = E_g + \Delta\{1 - N\cos[aA(t_s)]\}. \tag{4.10}$$

Then, ω maximizes when the last term in Eq. (4.10), $\cos[aA(t_s)] = -1$. This condition is fulfilled when the laser is strong enough to accelerate electrons to the edge of the Brillouin zone, i.e., for $F_0/\omega_0 \geq \pi/a$, or for $F_0 \geq F_b$ with $F_b = \pi\omega_0/a$ the Bloch field strength. For the system considered here, with $a = 5.32$ a.u. and $\omega_0 = 0.014$ a.u., it is $F_b \approx 0.008$ a.u. As a result, for $F = F_b$ a single saddle point ($N = 1$) can produce cut-off harmonics equal to the fundamental plateau. Addition of the second saddle point ($N = 2$) creates a second plateau, and so on so forth.

In summary, emission of harmonics above the fundamental band gap seems to proceed as a cascaded nonlinearity at each field node, represented by adding the contribution of each saddle point.

The intensity of the second plateau is extremely weak, which makes it experimentally irrelevant. However, the plateau can be intensified by adding a higher-lying conduction band.

To demonstrate it, the semiconductor Bloch equations are extended to include three bands. Figure 4.8 shows the valence band (V) and the first (C_1) and second (C_2) conduction bands of ZnO which are used in the three-band simulations. Due to the wide band gap between V and C_2 at Γ, it is unlikely that population tunnels directly between these two bands. Therefore, only the coupling between $V - C_1$ and $C_1 - C_2$ is considered. At the edge of the Brillouin zone, the gap between C_1 and C_2 is ~ 1 eV.

Figure 4.9(a) shows a comparison of the two-band (red) and three-band (green) models for ZnO for $F_0 = 0.01$ a.u. The addition of the second conduction band has little effect on the overall harmonic spectrum. However, reducing the band gap at the edge of the Brillouin zone from 1 eV (ZnO) to 0.75 eV results in a significant enhancement of the second plateau; see the purple line in Fig. 4.9(a). The time-frequency analysis of Fig. 4.9(b) for the green three-band spectrum reveals that the addition of the third band does not affect the dominance of the recollision mechanism in the first plateau. However, emission at the field nodes becomes visible in the spectrogram of the purple three-band spectrum. This demonstrates that the interband emission mechanism introduced in this section remains intact in three-band systems, and is responsible for the enhancement of the second plateau. The nature of this enhancement, however, is still unclear.

The enhancement of the high harmonic emission at very high harmonic orders suggests the possibility to extend the harmonic cut-off to higher energies by using materials with a small band gap at the edge of the Brillouin zone. Furthermore, materials are typically more transparent to soft X-rays than to vacuum-ultraviolet light, effectively enhancing second and higher plateaus. For example, in silicon the absorption length increases from a minimum of 7 nm at ~ 5.6 eV to 66 nm at ~ 31 eV – an increase of four orders of magnitude in transmission at such distance from the surface.

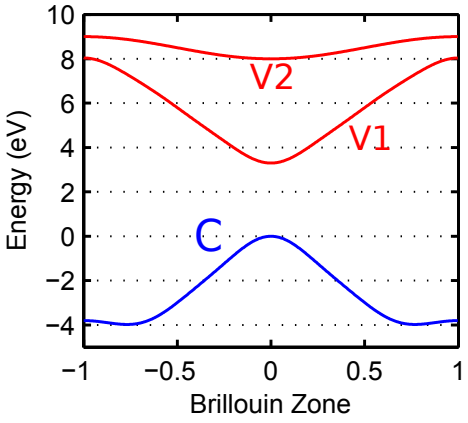

Figure 4.8: Band structure along $\Gamma - M$ for three-band model with a single valence band (blue) and two conduction bands (red).

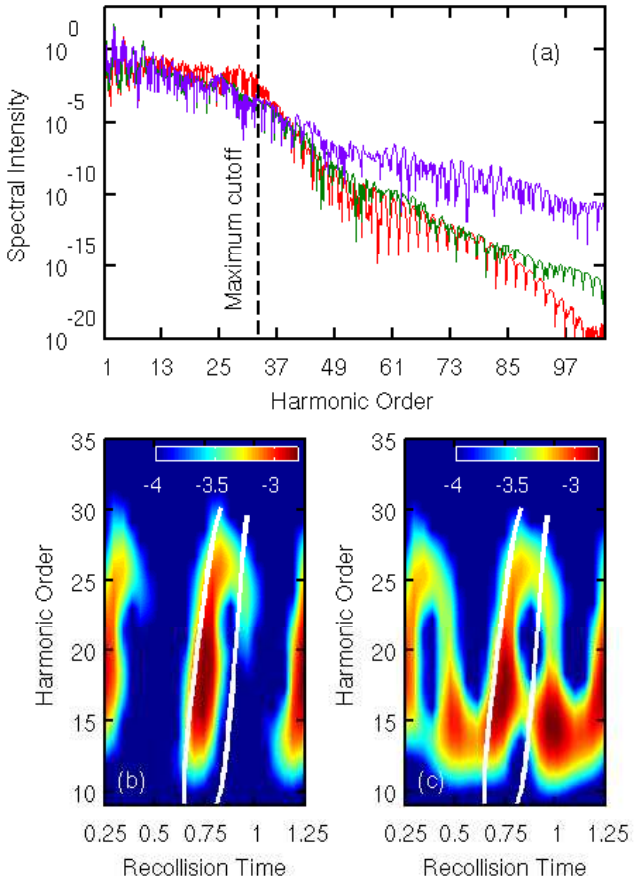

Figure 4.9: **(a)** Comparison of the harmonic spectra at $F_0 = 0.01$ a.u. for the two-band (red) and three-band (green) ZnO models. In addition a harmonic spectrum with a reduced bandgap between the conduction bands at the Brillouin zone edge is shown (purple). **(b)** Time-frequency analysis of the first cut-off for the three-band model. **(c)** Time-frequency analysis of the first cut-off for the three-band model with reduced band gap between conduction bands at the Brillouin zone edge. The white lines are the results for the first two electron-hole recollisions from the semiclassical trajectory analysis for the two-band model. The color scale is logarithmic.

Conclusions

In conclusion, the suggestion that recollision between electrons and holes causes emission of high harmonics has been confirmed both with extensive numerical and analytical work and with two experiments performed with very different materials (ZnO and Si) and with a mid-infrared laser. Thus, 50 years after Keldysh explained strong-field tunnelling of atoms and solids in a unified way, my work unifies the response of gases and solids to strong fields once again.

The link I established will allow extending atomic attosecond spectroscopic methods based on high harmonics to the condensed phase. But novel methods can also be developed specifically for solids. For example, I explained how high harmonic spectroscopy can yield accurate and complete information about the momentum-dependent band structure of solids, a key information in modern material design.

Rapid dephasing – an effect absent in gases – could play an important and potentially helpful role. If high harmonics survive despite strong dephasing, it will be possible to search for similar nonlinear phenomena in many other materials – even soft and biological matter or solution-phase chemistry. The flood-gate of research on high harmonic generation and its associated spectroscopy is opening, as research in a broad range of materials is ongoing. In the future, a better knowledge of dephasing mechanisms and rates is also advisable. Research is already steering in this direction [58].

In the two experiments conducted in ZnO and Si, very weak second harmonic fields – as weak as DC and AC fields found in conventional semiconductors – impose a clear spectral signature on the high harmonics. It seems likely that this sensitivity can be exploited to record movies of working electrical circuits or of nano-plasmonic devices. When the circuit is *off*, harmonics will diffract according to the spatial features within the circuit. When the circuit is *on*, the electric fields modify the diffracted pattern. Comparison of the *off* with the *on* pattern will return the distribution of the fields within. Therefore, high harmonics from solids can be relevant for the technological endeavour of fusing attosecond science with electronics.

Despite the role played by recollisions, other mechanisms, both intraband and interband in nature, also emit harmonics. Some of them are known to the scientific community, and have been found to dominate emission of harmonics from longer

wavelength sources ($\sim 10\mu$m) up to the visible spectral region (below the direct band gap) [17], and from shorter wavelength (800 nm) sources at very high energies (20-40 eV) [18]. Most interesting was the explanation of the generation of even harmonics [31]. However, I've shown that each generation mechanism in the intraband current has an analogue in the interband current, and vice-versa. It will be interesting to hunt for these new mechanisms.

Appendix A

Band structure of ZnO and Si and details on the simulations

The Semiconductor Bloch equations, Eqs. (2.8), are integrated numerically with Runge-Kutta method. The inter- and intraband currents and their respective high-harmonic spectra are separately calculated with Eqs. 2.6. The numerical value of the transition dipole moment $\mathrm{d_{cv}}$ has been extracted from tabulated data [19] and its k-dependence is neglected.

The laser is characterized by field amplitude $\mathbf{F}(t) = F_0 f(t)\cos(\omega_0 t)\hat{\mathbf{x}}$, consisting of a temporal Gaussian envelope $f(t)$ and cosine carrier with frequency ω_0. The input electric field is the one inside the material. The vacuum field strength is obtained by taking into account the reflection loss at the air-solid interface: $F_{\mathrm{vac}} = (n+1)F_0/2$, where n is the refractive index of the solid.

The bands calculated with Density Functional Theory are fitted to a Fourier series expansion which is used in the integration of Eqs. (2.8). 3D and 1D simulations are performed. The 3D band structure is approximated as:

$$E_{\mathrm{m}}(\mathbf{k}) = E_{\mathrm{m,x}}(\mathrm{k_x}) + E_{\mathrm{m,y}}(\mathrm{k_y}) + E_{\mathrm{m,z}}(\mathrm{k_z}). \tag{A.1}$$

For each direction in reciprocal space ($i = x, y, z$):

$$E_{\mathrm{v},i}(k_i) = \sum_{j=0}^{\infty} \alpha_{\mathrm{v},i}^{j} \cos(j k_i a_i) \tag{A.2a}$$

$$E_{\mathrm{c},i}(k_i) = E_g + \sum_{j=0}^{\infty} \alpha_{\mathrm{c},i}^{j} \cos(j k_i a_i) \tag{A.2b}$$

with $a_i = 2\pi/\kappa_i$ where κ_i the reciprocal space wavevector along coordinate i. Only one valence and one conduction bands are considered, unless when mentioned otherwise (see Sec. 4.3). Initially, the valence band is completely full, and the conduction band completely empty.

Parameters for ZnO. ZnO has a wurtzite structure at ambient conditions. The Brillouin zone of ZnO is depicted in Fig. A.1(b). The energy bands along some

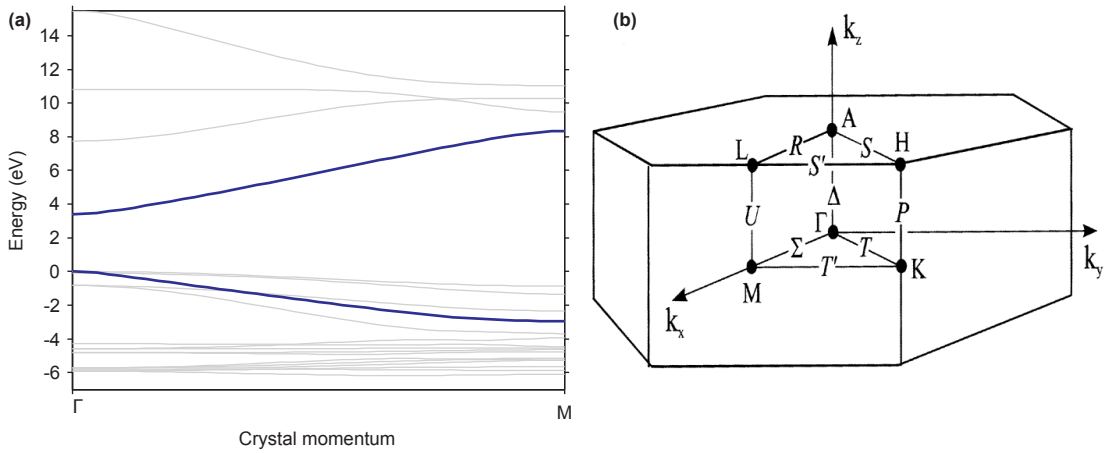

Figure A.1: **(a)** Band structure of ZnO along the $\Gamma - M$ direction of the Brillouin zone, calculated with LDA-ABINIT. The split-off valence and first conduction bands of ZnO are coloured blue. **(b)** Brillouin zone of wurtzite ZnO. The high symmetry points are indicated.

high-symmetry directions obtained by *ab initio* calculations in the Local Density Approximations (ABINIT), are plotted in panel (a). The split-off valence and first conduction bands are highlighted in blue.

In all simulations, the crystallographic axis have been oriented such that $\hat{\mathbf{x}} \parallel \Gamma{-}M$, $\hat{\mathbf{y}} \parallel \Gamma{-}K$, and $\hat{\mathbf{z}} \parallel \Gamma{-}A$ (optical axis); along these directions $(a_x, a_y, a_z) = (5.32, 6.14, 9.83)$ a.u. The expansion coefficients $\alpha^j_{\mathrm{m},i}$ $(i = x, y, z,\ j = 0, 1\ldots)$ for valence (m = v) and conduction (m = c) band are obtained from expanding the bands calculated with a Non-Local Empirical Pseudopotential Method (NL-EPM, described in Ref. [59]) up to $j = 5$ for Γ–M; the nearest neighbour expansion is used for $\Gamma{-}K$ and $\Gamma{-}A$. The resulting coefficients are listed in table A.1. The bandgap energy at the Γ-point is given by $E_{\mathrm{g}} = 0.1213$ a.u. (3.3 eV). It should be noted here that both the local density approximation (LDA-ABINIT) and NL-EPM were used to determine the ZnO band structure. While some quantitative differences exist, the conclusions remain unchanged.

	Valence band	Conduction band
$\alpha_{0,x}$	-0.0928	0.0898
$\alpha_{1,x}$	0.0705	-0.0814
$\alpha_{2,x}$	0.0200	-0.0024
$\alpha_{3,x}$	-0.0012	-0.0048
$\alpha_{4,x}$	0.0029	-0.0003
$\alpha_{5,x}$	0.0006	-0.0009
$\alpha_{0,y}$	-0.0307	0.1147
$\alpha_{1,y}$	0.0307	-0.1147
$\alpha_{0,z}$	-0.0059	0.0435
$\alpha_{1,z}$	0.0059	-0.0435

Table A.1: Coefficients of the expansion of the NL-EPM bands from Ref.[59] for the crystal field split valence band and the first conduction band.

The transition dipole moment is $\mathbf{d} = (3.46, 3.46, 3.94)$ a.u.

Parameters for Si. Silicon has the diamond crystal structure. The first Brillouin zone and the band structure along two directions of high-symmetry have been plotted in Fig. 3.10. The band structure has been obtained with LDA-ABINIT. The lattice constant of Si is $a = 10.8$ a.u. The band parameters along the $\Gamma - M$ direction for the bands used in the calculation of the semiclassical trajectories of Fig. 3.12 are reported in table A.2. The transition dipole moment has been taken equal to that of ZnO.

	Valence band	Conduction band
$\alpha_{0,x}$	0.1315	0.04495
$\alpha_{1,x}$	0.02758	-0.01445
$\alpha_{2,x}$	0.01031	-0.00684
$\alpha_{3,x}$	0.004835	-0.00159
$\alpha_{4,x}$	0.002588	-0.00034
$\alpha_{5,x}$	0.001498	-0.00045

Table A.2: Coefficients of the expansion of the LDA-ABINIT bands for the valence band and the first conduction band of Si along the $\Gamma - M$ direction.

Appendix B

Detailed analysis of the reconstruction method

In this Appendix, the effects of several parameters on the results of band gap reconstruction are analysed.

Effect of the functional form of the trials

As in any variational method, the functional form of the trial dictates how accurately the reconstructed band gap approximates the real band structure. In the main text it was shown that, when the target band has the same functional form as the trials, the reconstructed bands lie very close to the target. In this section, instead, the method is generalized to the real ZnO target band structure, obtained from Density Functional Theory calculations in the Local Density Approximation (labelled "LDA" in the following), expanded up to the 5^{th} spatial frequency and to two sets of trial bands: one set has functional form

$$\varepsilon_g(\mathrm{k}) = E_g + A[1\cos(\mathrm{k}a)] + B[1\cos(2\mathrm{k}a)] \tag{B.1}$$

(as in the main text, labelled "NNN" in Fig. B.1); the other set has functional form

$$\varepsilon_g(\mathrm{k}) = E_g - (E_g/2)^{2B} + [(E_g/2)^2 + (A\mathrm{k}a)^2]^B \tag{B.2}$$

(labelled "SQ" in Fig. B.1). In both cases only two parameters (A,B) need to be scanned. The parameters of the target band are reported in Table B.1.

Figure B.1 shows the result of the reconstruction. The target phase and target band gap are reported as red lines (labelled "LDA") in panels (a,c) and (b,d) respectively. The ZnO split-off valence and first conduction bands have small effective masses and strong linearity across the Brillouin zone, a shape not accurately reproduced by the short expansion used in the main text. The results with the "SQ" bands are shown in panels (a) and (b). All trial bands but one are rejected with a confidence level of 90%, because the probability of measuring $\chi^2 > \chi_i^2$ is less than the threshold p-value of 0.1. The only plausible band has p = 0.2 and it well

Spatial frequency	Parameter values (eV)
$\varepsilon_g(\mathrm{k}) = E_g +$	E_g = 3.4
$+A+$	A = 4.1714
$+B[1-\cos(\mathrm{k}a)]+$	B = -3.6175
$+C[1-\cos(2\mathrm{k}a)]+$	C = -0.1488
$+D[1-\cos(3\mathrm{k}a)]+$	D = -0.2568
$+E[1-\cos(4\mathrm{k}a)]+$	E = -0.07396
$+F[1-\cos(5\mathrm{k}a)]+$	F = -0.07431

Table B.1: Band parameters for "LDA" ZnO target band gap. Each term of the functional form of the target ZnO band is reported in the left column; the value of the parameter is in the second column. The bands are obtained from a LDA-DFT calculation and fit to the above functional form.

Parameter	Value	Units
a_l	3.250	$\mathring{A}$
$a = \sqrt{(3)}/2a_l$	2.814	$\mathring{A}$
ε_g	3.4	eV
F_0	0.285	V/$\mathring{A}$
F_1	0.04	F_0
λ	3.66	μm
τ	60	fs
T_2	1.3	fs
d	1.8	$\mathring{A}$

Table B.2: Parameters of the simulation. a_l is the lattice constant of wurtzite ZnO, $a = 2\pi/\kappa$, where κ is the reciprocal lattice vector along the $\Gamma - M$ direction, ε_g is the minimum bandgap (at Γ), F_0 and F_1 are the peak field strength of the fundamental and second harmonic, λ is the fundamental wavelength, τ is the pulse duration, T_2 is the dephasing time of the interband polarization and d is the transition dipole moment between the bands.

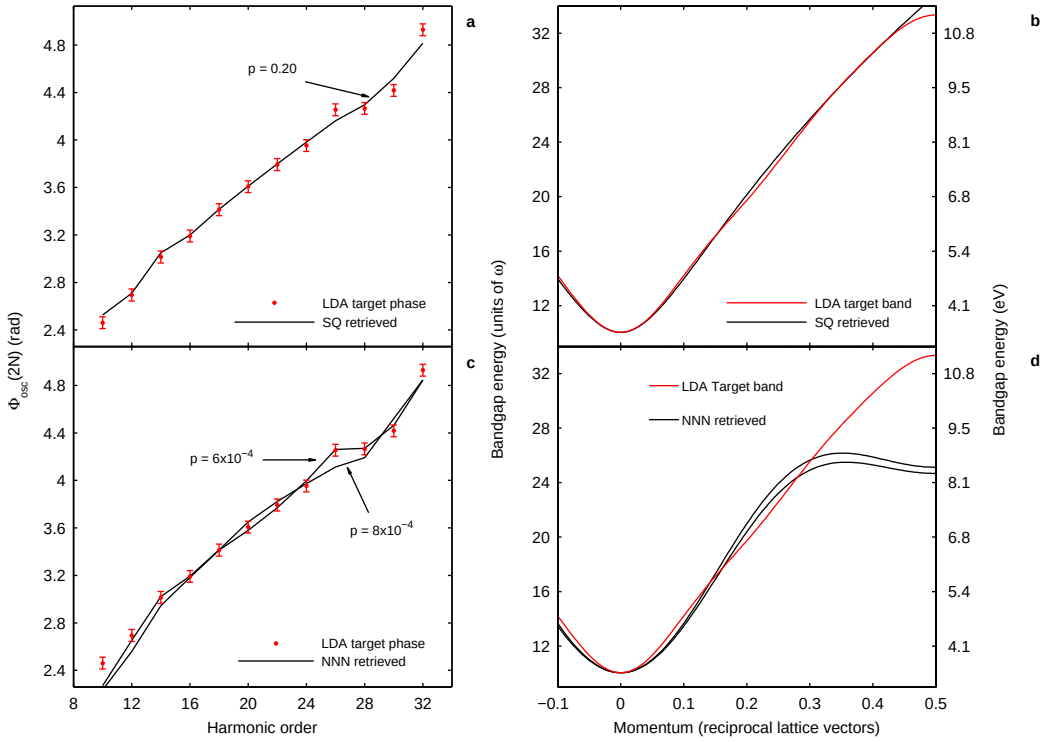

Figure B.1: Reconstruction with different functional forms. Panels **(a)** and **(b)** show the result of the reconstruction with the functional form of the trial bandgaps labelled "SQ" in the text. Φ_{osc} is plotted in panel (a) for the target "LDA" band (red dots) and for the retrieved band. The band gaps are plotted in panel (b), for the target (red lines) and for the "SQ" retrieved band (gray line). Panels **(c)** and **(d)** show the result with "NNN" bands. Here, no bands have sufficient confidence. The two most confident ones are plotted as light grey lines. The corresponding p-values are reported and labelled "p".

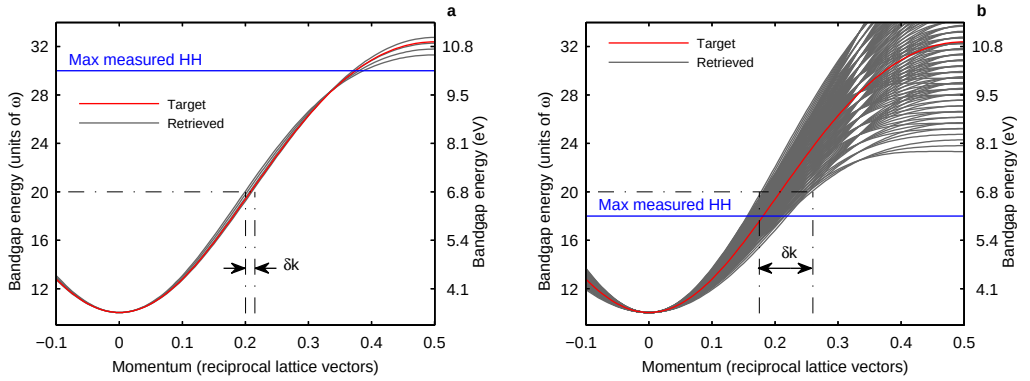

Figure B.2: Effect of the measured harmonic range on the reconstruction. When only harmonics up to the 18^{th} are measured (panel **b**), many more bands become plausible (grey lines). Panel **(a)** shows the reconstruction of Fig. 4.2, when harmonics up to the 30^{th} order are measured.

approximates the target band gap, except at the edge of the Brillouin zone, where the derivative of the target vanishes as expected from the Fourier expansion. The functional form of the trials cannot reproduce this feature. On the contrary, if only two spatial frequencies are used in the Fourier expansion (the "NNN" trials, shown in panels **c** and **d**), all bands must be rejected with a 90% confidence level. The two best guesses are reported in the figures, with p-values of 6×10^{-4} and 8×10^{-4}. They fail to reproduce both the high curvature around Γ and the total width of the band gap. Clearly, the strong linearity of the target bands cannot be captured with a Fourier expansion up to only two spatially defined frequencies.

In conclusion, the good sensitivity of Φ_{osc} to the functional form of the band gap implies a strong selectivity of the method to the band structure.

Effect of the measured high harmonic range on the accuracy of the reconstruction

Accurate reconstruction of the band gaps requires measurement of many high harmonics. In the situation presented in Fig. 4.2 of the main text, the "measured" harmonic range extends up to the 30^{th} harmonic order, which is very close to the maximum band gap of the target band structure. The reconstructed band structures lie very close to the target, as shown in Fig. 4.2(c) and reported in Fig. B.2(a). However, many more bands are plausible when the "measured" harmonic range extends only up to the 18^{th} order, as shown in Fig. B.2(b).

The loss in the accuracy of the reconstruction can be interpreted as a loss of momentum resolution. This can be taken as the difference between the maximum and minimum momenta that correspond to a given harmonic photon energy in the set of plausible bands. The black dash-dotted lines in Fig. B.2 mark the momentum resolution δk at the 20^{th} harmonic order. Although it may seem strange at first, a heuristic explanation of the dependence of the resolution on the accuracy of the reconstruction is the following. Consider the trajectories depicted by the two wiggled

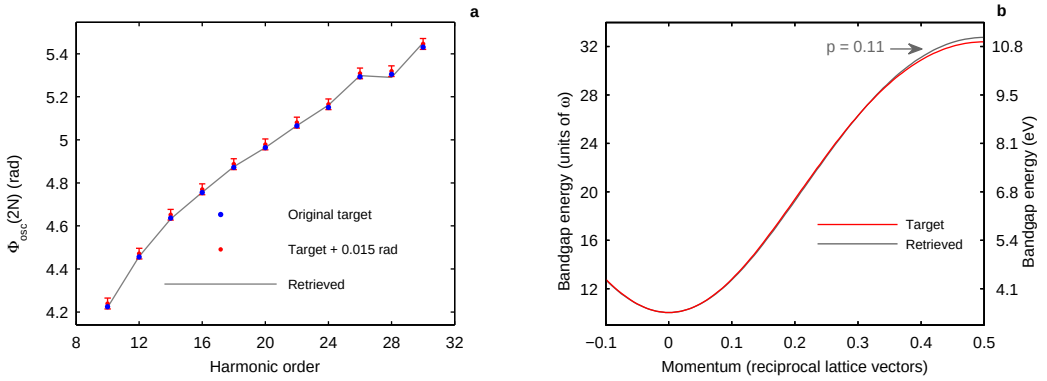

Figure B.3: Effect of the absolute phase on the reconstruction. When the target phase of Fig. 4.2 (blue dots in panel a) is offset by 0.015 rad (red dots with error bar in panel a), only one band is plausible, with p-value of 0.11 (therefore lower than in Fig. 4.2). The retrieved phase is the grey line in panel **(a)**, while the associated band structure is the grey line in panel **(b)**. The target band structure is the red line in panel (b). Target and trial are almost indistinguishable.

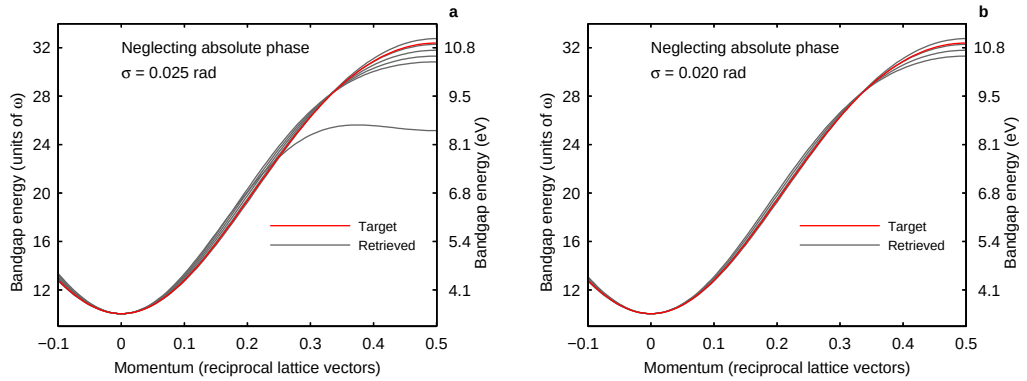

Figure B.4: Effect of neglecting the absolute phase on the reconstruction. When the average optimum phase is removed from the trials and the target (both panels), the reconstruction returns similar results to those obtained in Fig. 4.2, but some extra bands become plausible (panel **a**). The same accuracy as when the absolute phase is included can be achieved by reducing the experimental error on the optimum phase from $\sigma = 0.025$ rad (as in Fig. 4.2) to 0.02 rad (panel **b**).

arrows of Fig. 4.1. Although they are mapped to two different harmonic photon energies, both propagate along the lower part of the band. Therefore, there is redundant information about the bottom part. The higher part is however only sensed by the top trajectory. Here, the redundancy is lost. When many harmonics are measured, there is plenty of redundant information about the lower part of the bands, and the resolution is therefore high. On the contrary, when few harmonic orders are measured there is less redundancy and the momentum resolution is lower.

Effect of the absolute phase on the reconstruction

Shifting the absolute phase. The absolute optimum phase is a measurable parameter that, when used, improves the accuracy of the reconstruction. Figure B.3

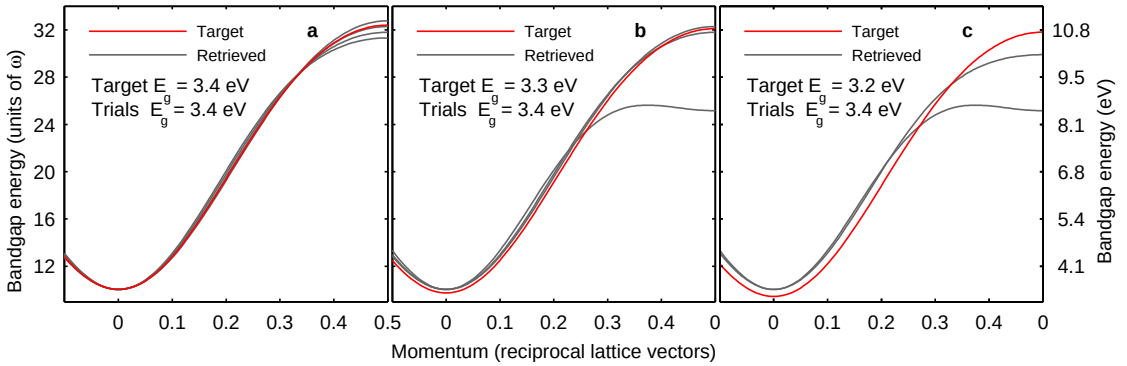

Figure B.5: Effect of the minimum band gap on the reconstruction. The minimum band gap E_g of the target band structure is progressively decreased from 3.4 eV (as in Fig. 4.2) to 3.2 eV, through panels (a) to (c). The reconstruction performed with the same set of trials with $E_g = 3.4$ eV (as in Fig. 4.2) fails for $E_g < 3.3$ eV (panel c).

shows the effect that varying the absolute phase of the target by 0.015 rad (equivalent to about half the uncertainty on the optimum phase) has on the reconstruction. Only one band is plausible and has p = 0.11, just above the acceptance threshold. The associated band gap, grey line of panel (b), closely matches the target (red line). When the absolute phase is offset by more than ~ 0.03 rad (equivalent to the uncertainty on the optimum phase), no bands are plausible.

The sensitivity to the optimum phase can be mitigated by neglecting it. Figure B.4 shows the results when the average phase is removed from both the target and the trials. This corresponds to a situation where the absolute phase in not measured in the experiment. The lack of the extra constraint represented by matching the absolute phase results in slightly lower accuracy (panel a). High precision can be restored by measuring the optimum phase more accurately (from 0.025 rad to 0.020 rad), as shown in panel (b).

Varying the minimum gap. In the simulations, a variation of the minimum bang gap E_g results in an almost rigid shift of the absolute optimum phase. In our model target solid of Fig. 4.2, for example, a variation of E_g by 0.2 eV results in a variation of 0.1 rad of the absolute phase. This dependence can be understood in the following way. Each harmonic order is linked to a specific trajectory of the electron-hole pair when it is referenced to the minimum band gap. A harmonic photon with energy exactly equal to E_g corresponds to electron-hole pairs that do not travel in the solid: they recombine as soon as they are created. If the reference is lowered, the same harmonic order corresponds to emission above the minimum band gap. Therefore, the associated trajectory and its optimum phase are different. Owing to the shape of the bands, the variation in the optimum phase differs between harmonic orders. However, we find that when the variation in E_g is less than the fundamental photon energy, the variation of the optimum phase is similar for all harmonic orders.

As shown in Fig. B.4, a rigid shift in the optimum phase is rather unimportant,

since the reconstruction can also be performed by neglecting it. However, it is important to investigate the effect of deviations from a rigid shift as E_g is varied. In an experiment, it is the E_g of the trials that has to adapt to a given experimental measurement of Φ_{osc}. For simplicity, in Fig. B.5 the same set of trials with $E_g = 3.4$ eV (as for Fig. 4.2) is compared to three different target bands with the same shape as in Fig. 4.2, but with E_g decreasing from 3.4 eV to 3.2 eV. As the gap is decreased, the convergence to the target band gap worsens. For the reconstruction, the average phase is removed because target and trials differ by more than 0.03 rad. Good convergence is achieved for variations < 0.2 eV of E_g between the target and the trials, corresponding to $\sim 60\%$ of the fundamental photon energy.

The fundamental energy gap of solids is typically well known. Uncertainty can arise from a lack of knowledge of which valence band mostly contributes to high harmonic generation (the top-most valence bands can differ in the maximum energy by < 1 eV), and to band gap renormalization following strong excitation. The latter has been measured to be ~ 0.2 eV in silicon, excited by intense visible pulses [13]. The analysis presented above proves that for deviations in the minimum gap between target and trials is < 0.2 eV the method is sensitive to band gap renormalization if the offset phase is measured, otherwise it returns the field-free band structure. For stronger variations, either the minimum band gap has to be measured and replaced in the simulations, or the trials need to be tuned to correctly reconstruct the experimental band structure.

Appendix C

Including depletion in the analytical solution to the semiconductor Bloch equations

In chapter 2, the Semiconductor Bloch equations have been solved in the limit of low excitation. This approximation not only limits the population in the valence band to the initial one, but removes the effect of Stark shift on the motion of electron-hole pairs. A more complete analytical solution to the Semiconductor Bloch equations can be obtained starting from Eqs. (2.3):

$$\dot{a}_{\mathrm{m}} = (-iE_{\mathrm{m}}(\mathbf{k}) + \mathbf{F}(t)\nabla_{\mathbf{k}})a_{\mathrm{m}} + i\mathbf{F}(t)\sum_{m'\neq m}\mathbf{d}_{\mathrm{mm'}}(\mathbf{k})a_{\mathrm{m'}} \tag{C.1}$$

where $m = \{c, v\}$, and simplifying them with the coordinate transformation:

$$\mathbf{K}(\mathrm{k}, t) = \mathbf{k} - \mathbf{A}(t); \quad \tau(\mathrm{k}, t) = t$$

and with the ansatz:

$$a_m(\mathbf{K}, \tau) = b_m(\mathbf{K}, \tau)e^{-i\int_{\infty}^{\tau} E_m[\mathbf{K}+\mathbf{A}(t')]dt'}$$

to obtain:

$$\dot{b}_v(\mathbf{K}, \tau) = i\mathbf{F}(\tau)\mathbf{d}_{\mathrm{cv}}(\mathbf{K} + \mathbf{A})b_c(\mathbf{K}, \tau)e^{-i\int_{-\infty}^{\tau}\varepsilon_g(\mathbf{K}+\mathbf{A})dt'} \tag{C.2a}$$

$$\dot{b}_c(\mathbf{K}, \tau) = i\mathbf{F}(\tau)\mathbf{d}^*_{\mathrm{cv}}(\mathbf{K} + \mathbf{A})b_v(\mathbf{K}, \tau)e^{i\int_{-\infty}^{\tau}\varepsilon_g(\mathbf{K}+\mathbf{A})dt'} \tag{C.2b}$$

where $\varepsilon_g(\mathbf{k}) = E_c(\mathbf{k}) - E_v(\mathbf{k})$. The two equations can be uncoupled by deriving each one and replacing the first derivatives with the above equations. For the conduction band, the result reads:

$$\ddot{b}_c = ig\dot{b}_c - \Omega^2 b_c \tag{C.3}$$

where

$$ig = \frac{d}{d\tau}\ln(Fd^*) + i\varepsilon_g \tag{C.4a}$$

$$\Omega = Fd^* \tag{C.4b}$$

The latter is the Rabi frequency. The dependencies on $\mathbf{K}$ and τ have been omitted for convenience. Eq. (C.3) can be cast into a form suitable for integration with the WKB method by applying the transformation:

$$b_c = c_c \, e^{i/2 \int_{-\infty}^{\tau} g(t')dt'} \tag{C.5}$$

to obtain:

$$\begin{aligned} \ddot{c_c} &= -\left(\frac{i}{2}\dot{g} + \frac{g^2}{4} + \Omega^2\right) c_c \\ &= Q \; c_c \end{aligned}$$

Solution of the above equation with the WKB method results in:

$$c_c = \frac{1}{Q^{1/4}} e^{\pm \int_{-\infty}^{\tau} \sqrt{Q(t')}dt'} \tag{C.7}$$

If one approximates $ig \simeq i\varepsilon_g$ and $\dot{g} \simeq 0$, then

$$c_c \propto e^{\pm i \int_{\infty}^{\tau} \sqrt{\frac{\varepsilon_g^2}{4} + \Omega^2} \, dt'} \tag{C.8}$$

Applying Eq. C.5 yields:

$$b_c \propto \exp\left[i \int_{-\infty}^{\tau} \frac{\varepsilon_g}{2} + \sqrt{\frac{\varepsilon_g}{4} + \Omega^2} \, dt'\right] \simeq \tag{C.9a}$$

$$\simeq \exp\left[i \int_{-\infty}^{\tau} \varepsilon_g \left(1 + \frac{\Omega^2}{\varepsilon_g^2}\right) \, dt'\right] \tag{C.9b}$$

where the square root has been expanded for small Ω^2/ε_g^2. In the limit of vanishing fields ($\Omega \to 0$), the above result implies that electron-hole pairs move in the field-free band structure. This approximation is valid as long as $\Omega^2/\varepsilon_g^2 \ll 1$.

Bibliography

[1] L. Keldysh, "Ionization in the field of a strong electromagnetic wave," *Sov. Phys. JETP*, vol. 20, no. 5, pp. 1307–1314, 1965.

[2] P. Corkum and F. Krausz, "Attosecond science," *Nature Physics*, vol. 3, no. 6, pp. 381–387, 2007.

[3] T. Popmintchev, M.-C. Chen, D. Popmintchev, P. Arpin, S. Brown, S. Ališauskas, G. Andriukaitis, T. Balčiunas, O. D. Mücke, A. Pugzlys, *et al.*, "Bright coherent ultrahigh harmonics in the kev x-ray regime from mid-infrared femtosecond lasers," *science*, vol. 336, no. 6086, pp. 1287–1291, 2012.

[4] J. Itatani, J. Levesque, D. Zeidler, H. Niikura, H. Pépin, J.-C. Kieffer, P. B. Corkum, and D. M. Villeneuve, "Tomographic imaging of molecular orbitals," *Nature*, vol. 432, no. 7019, pp. 867–871, 2004.

[5] C. Vozzi, M. Negro, F. Calegari, G. Sansone, M. Nisoli, S. De Silvestri, and S. Stagira, "Generalized molecular orbital tomography," *Nature Physics*, vol. 7, no. 10, pp. 822–826, 2011.

[6] H. Worner, J. Bertrand, D. Kartashov, P. Corkum, and D. Villeneuve, "Following a chemical reaction using high-harmonic spectroscop," *Nature*, vol. 466, no. 7306, pp. 604–607, 2010.

[7] O. Smirnova, Y. Mairesse, S. Patchkovskii, N. Dudovich, D. Villeneuve, P. Corkum, and M. Y. Ivanov, "High harmonic interferometry of multi-electron dynamics in molecules," *Nature*, vol. 460, no. 7258, pp. 972–977, 2009.

[8] A. Shiner, B. Schmidt, C. Trallero-Herrero, H. Wörner, S. Patchkovskii, P. Corkum, J. Kieffer, F. Légaré, and D. Villeneuve, "Probing collective multi-electron dynamics in xenon with high-harmonic spectroscopy," *Nature Physics*, vol. 7, no. 6, pp. 464–467, 2011.

[9] K. Zhao, Q. Zhang, M. Chini, Y. Wu, X. Wang, and Z. Chang, "Tailoring a 67 attosecond pulse through advantageous phase-mismatch," *Optics letters*, vol. 37, no. 18, pp. 3891–3893, 2012.

[10] E. Goulielmakis, Z.-H. Loh, A. Wirth, R. Santra, N. Rohringer, V. S. Yakovlev, S. Zherebtsov, T. Pfeifer, A. M. Azzeer, M. F. Kling, *et al.*, "Real-time obser-

vation of valence electron motion," *Nature*, vol. 466, no. 7307, pp. 739–743, 2010.

[11] H. Wang, M. Chini, S. Chen, C.-H. Zhang, F. He, Y. Cheng, Y. Wu, U. Thumm, and Z. Chang, "Attosecond time-resolved autoionization of argon," *Physical review letters*, vol. 105, no. 14, p. 143002, 2010.

[12] M. Schultze, E. M. Bothschafter, A. Sommer, S. Holzner, W. Schweinberger, M. Fiess, M. Hofstetter, R. Kienberger, V. Apalkov, V. S. Yakovlev, *et al.*, "Controlling dielectrics with the electric field of light," *Nature*, vol. 493, no. 7430, pp. 75–78, 2013.

[13] M. Schultze, K. Ramasesha, C. Pemmaraju, S. Sato, D. Whitmore, A. Gandman, J. S. Prell, L. J. Borja, D. Prendergast, K. Yabana, D. M. Neumark, and S. R. Leone, "Attosecond band-gap dynamics in silicon," *Science*, vol. 346, no. 6215, pp. 1348–1352, 2014.

[14] S. Neppl, R. Ernstorfer, A. Cavalieri, C. Lemell, G. Wachter, E. Magerl, E. Bothschafter, M. Jobst, M. Hofstetter, U. Kleineberg, *et al.*, "Direct observation of electron propagation and dielectric screening on the atomic length scale," *Nature*, vol. 517, no. 7534, pp. 342–346, 2015.

[15] F. Calegari, D. Ayuso, A. Trabattoni, L. Belshaw, S. De Camillis, S. Anumula, F. Frassetto, L. Poletto, A. Palacios, P. Decleva, *et al.*, "Ultrafast electron dynamics in phenylalanine initiated by attosecond pulses," *Science*, vol. 346, no. 6207, pp. 336–339, 2014.

[16] S. Ghimire, A. D. DiChiara, E. Sistrunk, P. Agostini, L. F. DiMauro, and D. A. Reis, "Observation of high-order harmonic generation in a bulk crystal," *Nature physics*, vol. 7, no. 2, pp. 138–141, 2011.

[17] O. Schubert, M. Hohenleutner, F. Langer, B. Urbanek, C. Lange, U. Huttner, D. Golde, T. Meier, M. Kira, S. Koch, *et al.*, "Sub-cycle control of terahertz high-harmonic generation by dynamical bloch oscillations," *Nature Photonics*, vol. 8, no. 2, pp. 119–123, 2014.

[18] T. Luu, M. Garg, S. Y. Kruchinin, A. Moulet, M. T. Hassan, and E. Goulielmakis, "Extreme ultraviolet high-harmonic spectroscopy of solids," *Nature*, vol. 521, no. 7553, pp. 498–502, 2015.

[19] G. Vampa, C. McDonald, G. Orlando, D. Klug, P. Corkum, and T. Brabec, "Theoretical analysis of high-harmonic generation in solids," *Physical review letters*, vol. 113, no. 7, p. 073901, 2014.

[20] G. Vampa, C. McDonald, G. Orlando, P. Corkum, and T. Brabec, "Semiclassical analysis of high harmonic generation in bulk crystals," *Physical Review B*, vol. 91, no. 6, p. 064302, 2015.

[21] G. Vampa, C. McDonald, A. Fraser, and T. Brabec, "High-harmonic generation in solids: Bridging the gap between attosecond science and condensed matter physics," *Selected Topics in Quantum Electronics, IEEE Journal of*, vol. 21, no. 5, pp. 1–10, 2015.

[22] P. B. Corkum, "Plasma perspective on strong field multiphoton ionization," *Physical Review Letters*, vol. 71, no. 13, p. 1994, 1993.

[23] T. Pfeifer, C. Spielmann, and G. Gerber, "Femtosecond x-ray science," *Reports on Progress in Physics*, vol. 69, no. 2, p. 443, 2006.

[24] X. Gonze, B. Amadon, P.-M. Anglade, J.-M. Beuken, F. Bottin, P. Boulanger, F. Bruneval, D. Caliste, R. Caracas, M. Cote, *et al.*, "Abinit: First-principles approach to material and nanosystem properties," *Computer Physics Communications*, vol. 180, no. 12, pp. 2582–2615, 2009.

[25] J. Krieger and G. Iafrate, "Time evolution of bloch electrons in a homogeneous electric field," *Physical Review B*, vol. 33, no. 8, p. 5494, 1986.

[26] E. Blount, "Formalisms of band theory," *Solid state physics*, vol. 13, pp. 305–373, 1962.

[27] H. Haug and S. W. Koch, *Quantum theory of the optical and electronic properties of semiconductors*, vol. 5. World Scientific, 1990.

[28] D. Golde, T. Meier, and S. Koch, "High harmonics generated in semiconductor nanostructures by the coupled dynamics of optical inter-and intraband excitations," *Physical Review B*, vol. 77, no. 7, p. 075330, 2008.

[29] O. Smirnova, M. Ivanov, and M. Vrakking, "Multielectron high harmonic generation: Simple man on a complex plane," *Attosecond and XUV Physics*, pp. 201–256, 2014.

[30] F. Brunel, "Harmonic generation due to plasma effects in a gas undergoing multiphoton ionization in the high-intensity limit," *JOSA B*, vol. 7, no. 4, pp. 521–526, 1990.

[31] M. Hohenleutner, F. Langer, O. Schubert, M. Knorr, U. Huttner, S. Koch, M. Kira, and R. Huber, "Real-time observation of interfering crystal electrons in high-harmonic generation," *Nature*, vol. 523, pp. 572–575, 2015.

[32] G. Vampa, T. Hammond, N. Thiré, B. Schmidt, F. Légaré, C. McDonald, T. Brabec, and P. Corkum, "Linking high harmonics from gases and solids," *Nature*, vol. 522, no. 7557, pp. 462–464, 2015.

[33] G. Vampa, T. J. Hammond, N. Thiré, B. E. Schmidt, F. Légaré, D. D. Klug, and P. B. Corkum, "Generation of high harmonics from silicon," *arXiv preprint arXiv:1605.06345*, 2016.

[34] N. Dudovich, O. Smirnova, J. Levesque, Y. Mairesse, M. Y. Ivanov, D. Villeneuve, and P. B. Corkum, "Measuring and controlling the birth of attosecond xuv pulses," *Nature physics*, vol. 2, no. 11, pp. 781–786, 2006.

[35] R. W. Boyd, *Nonlinear optics*. Academic press, 2003.

[36] X. He, J. Dahlström, R. Rakowski, C. Heyl, A. Persson, J. Mauritsson, and A. LHuillier, "Interference effects in two-color high-order harmonic generation," *Physical Review A*, vol. 82, no. 3, p. 033410, 2010.

[37] M. I. Aroyo, D. Orobengoa, G. de la Flor, E. S. Tasci, J. M. Perez-Mato, and H. Wondratschek, "Brillouin-zone database on the bilbao crystallographic server," *Acta Crystallographica Section A: Foundations and Advances*, vol. 70, no. 2, pp. 126–137, 2014.

[38] E. Tasci, G. De la Flor, D. Orobengoa, C. Capillas, J. Perez-Mato, and M. Aroyo, "An introduction to the tools hosted in the bilbao crystallographic server," in *EPJ Web of Conferences*, vol. 22, p. 00009, EDP Sciences, 2012.

[39] C. C. Chang, "Silicon-on-sapphire epitaxy by vacuum sublimation: Leed–auger studies and electronic properties of the films," *Journal of Vacuum Science & Technology*, vol. 8, no. 3, pp. 500–511, 1971.

[40] Z. Chang, *Fundamentals of attosecond optics*. CRC Press, 2011.

[41] P. G. Hawkins, M. Y. Ivanov, and V. S. Yakovlev, "Effect of multiple conduction bands on high-harmonic emission from dielectrics," *Physical Review A*, vol. 91, no. 1, p. 013405, 2015.

[42] M. Wu, S. Ghimire, D. A. Reis, K. J. Schafer, and M. B. Gaarde, "High-harmonic generation from bloch electrons in solids," *Physical Review A*, vol. 91, no. 4, p. 043839, 2015.

[43] S. Ghimire, A. D. DiChiara, E. Sistrunk, G. Ndabashimiye, U. B. Szafruga, A. Mohammad, P. Agostini, L. F. DiMauro, and D. A. Reis, "Generation and propagation of high-order harmonics in crystals," *Physical Review A*, vol. 85, no. 4, p. 043836, 2012.

[44] G. Vampa, T. J. Hammond, N. Thiré, B. E. Schmidt, F. Légaré, C. R. McDonald, T. Brabec, D. D. Klug, and P. B. Corkum, "All-optical reconstruction of crystal band structure," *Phys. Rev. Lett.*, vol. 115, p. 193603, Nov 2015.

[45] C. McDonald, G. Vampa, P. Corkum, and T. Brabec, "Interband bloch oscillation mechanism for high-harmonic generation in semiconductor crystals," *Physical Review A*, vol. 92, no. 3, p. 033845, 2015.

[46] A. Damascelli, "Probing the electronic structure of complex systems by arpes," *Physica Scripta*, vol. 2004, no. T109, p. 61, 2004.

[47] A. Lanzara, P. Bogdanov, X. Zhou, S. Kellar, D. Feng, E. Lu, T. Yoshida, H. Eisaki, A. Fujimori, K. Kishio, *et al.*, "Evidence for ubiquitous strong electron–phonon coupling in high-temperature superconductors," *Nature*, vol. 412, no. 6846, pp. 510–514, 2001.

[48] A. Bostwick, T. Ohta, T. Seyller, K. Horn, and E. Rotenberg, "Quasiparticle dynamics in graphene," *Nature Physics*, vol. 3, no. 1, pp. 36–40, 2007.

[49] Y. Chen, J. Analytis, J.-H. Chu, Z. Liu, S.-K. Mo, X.-L. Qi, H. Zhang, D. Lu, X. Dai, Z. Fang, *et al.*, "Experimental realization of a three-dimensional topological insulator, bi2te3," *Science*, vol. 325, no. 5937, pp. 178–181, 2009.

[50] L. Perfetti, P. Loukakos, M. Lisowski, U. Bovensiepen, H. Eisaki, and M. Wolf, "Ultrafast electron relaxation in superconducting bi 2 sr 2 cacu 2 o 8+ δ by time-resolved photoelectron spectroscopy," *Physical review letters*, vol. 99, no. 19, p. 197001, 2007.

[51] J. Leeuwenburgh, B. Cooper, V. Averbukh, J. P. Marangos, and M. Ivanov, "High-order harmonic generation spectroscopy of correlation-driven electron hole dynamics," *Physical review letters*, vol. 111, no. 12, p. 123002, 2013.

[52] M. Lewenstein, P. Balcou, M. Y. Ivanov, A. Lhuillier, and P. B. Corkum, "Theory of high-harmonic generation by low-frequency laser fields," *Physical Review A*, vol. 49, no. 3, p. 2117, 1994.

[53] M. Eremets and I. Troyan, "Conductive dense hydrogen," *Nature materials*, vol. 10, no. 12, pp. 927–931, 2011.

[54] R. Huber, F. Tauser, A. Brodschelm, M. Bichler, G. Abstreiter, and A. Leitenstorfer, "How many-particle interactions develop after ultrafast excitation of an electron–hole plasma," *Nature*, vol. 414, no. 6861, pp. 286–289, 2001.

[55] R. Chang, S. Potnis, R. Ramos, C. Zhuang, M. Hallaji, A. Hayat, F. Duque-Gomez, J. Sipe, and A. M. Steinberg, "Observing the onset of effective mass," *Physical review letters*, vol. 112, no. 17, p. 170404, 2014.

[56] L. Perfetti, P. Loukakos, M. Lisowski, U. Bovensiepen, H. Berger, S. Biermann, P. Cornaglia, A. Georges, and M. Wolf, "Time evolution of the electronic structure of 1 t- tas 2 through the insulator-metal transition," *Physical review letters*, vol. 97, no. 6, p. 067402, 2006.

[57] T. Higuchi, M. I. Stockman, and P. Hommelhoff, "Strong-field perspective on high-harmonic radiation from bulk solids," *Physical review letters*, vol. 113, no. 21, p. 213901, 2014.

[58] A. P. Pati, I. S. Wahyutama, and A. N. Pfeiffer, "Subcycle-resolved probe retardation in strong-field pumped dielectrics," *Nature communications*, vol. 6, 2015.

[59] M. Goano, F. Bertazzi, M. Penna, and E. Bellotti, "Electronic structure of wurtzite zno: Nonlocal pseudopotential and ab initio calculations," *Journal of Applied Physics*, vol. 102, no. 8, p. 083709, 2007.